



12-2019

Vibrational properties of molecule-based multiferroics and quantum magnets across quantum phase transitions

Kendall Hughey

University of Tennessee, khughey1@vols.utk.edu

Follow this and additional works at: https://trace.tennessee.edu/utk_graddiss

Recommended Citation

Hughey, Kendall, "Vibrational properties of molecule-based multiferroics and quantum magnets across quantum phase transitions. " PhD diss., University of Tennessee, 2019.
https://trace.tennessee.edu/utk_graddiss/5599

This Dissertation is brought to you for free and open access by the Graduate School at TRACE: Tennessee Research and Creative Exchange. It has been accepted for inclusion in Doctoral Dissertations by an authorized administrator of TRACE: Tennessee Research and Creative Exchange. For more information, please contact trace@utk.edu.

To the Graduate Council:

I am submitting herewith a dissertation written by Kendall Hughey entitled "Vibrational properties of molecule-based multiferroics and quantum magnets across quantum phase transitions." I have examined the final electronic copy of this dissertation for form and content and recommend that it be accepted in partial fulfillment of the requirements for the degree of Doctor of Philosophy, with a major in Chemistry.

Janice Musfeldt, Major Professor

We have read this dissertation and recommend its acceptance:

Alexei Sokolov, David Mandrus, Ziling Xue

Accepted for the Council:

Dixie L. Thompson

Vice Provost and Dean of the Graduate School

(Original signatures are on file with official student records.)

**Vibrational properties of
molecule-based multiferroics and
quantum magnets across quantum
phase transitions**

A Dissertation Presented for the

Doctor of Philosophy

Degree

The University of Tennessee, Knoxville

Kendall Day Hughey

December 2019

Acknowledgments

First and foremost, I would like to thank my advisor, Professor Janice L. Musfeldt, for her valuable guidance and support throughout my graduate program – her knowledge in the various aspects of chemistry, physics, and materials science has been a superb resource.

I am grateful to Professors Alexei Sokolov, Ziling Xue, and David Mandrus for serving on my committee, as well as for all of their interest, help, and advice.

I wish to acknowledge all the (past and present) members of my research group: Judy Cherian, Amal al-Wahish, Ken O’Neal, Brian Hollinsworth, Michael Yokosuk, Amanda Clune, Shiyu Fan, Nathan Harms, Kevin Smith, Sabine Neal, Avery Blockmon, Kiman Park, and Brandon Chapman for their advice, encouragement, and collaboration. I am grateful to all the faculty and staff of the Chemistry Department who shared their knowledge with me and helped in a variety of ways during my graduate program.

Many thanks to John Singleton, Nandita Abhyankar, Naresh Dalal, Xiixin Ding, Mykhalo Ozerov, Zhiqiang Li, Dmitry Smirnov, Vivien Zapf, Jing Li, Hongjun Xiang, Wei Tian, Minseong Lee, Jisoo Nam, JunHee Lee, Jeffrey Monroe, and Christopher Landee for their excellent collaboration during these years.

I also thank the American Physical Society, the American Chemical Society, Wiley-VCH, Macmillan Publishers Ltd., Oxford University Press, Springer Science and Business Media, IOP Publishing Ltd., Elsevier, and the corresponding authors

for the kind permission to reproduce selected figures from their articles.

Finally, I am extremely grateful to my mom, dad, and sister for their support, encouragement, and patience, and to Michael, who has been a source of unwavering inspiration and optimism.

Abstract

Molecule-based materials offer unique opportunities to explore the interplay between charge, spin, and lattice across quantum phase transitions. With their flexible architectures and overall low energy scales, quantum phases can be induced at experimentally realizable conditions. In this dissertation, I present a spectroscopic study of three important families of multiferroics and quantum magnets with a variety of tuning parameters to unravel the mechanisms required to reach distinct non-equilibrium phases. The exploration of spin-lattice coupling and local lattice distortions across magnetic quantum phase transitions is the unifying theme of this work.

As our first platform for investigation, we explore the coupling between ferroic orders in the metal-organic framework $[(\text{CH}_3)_2\text{NH}_2]M(\text{HCOO})_3$ ($M=\text{Mn,Co,Ni}$) family. The formate bend links the ferroelectric and magnetic quantum phase transition in the Mn analog. Strikingly, B-site substitution drastically alters this mechanism. The Ni material behaves similarly to the Mn analog but at much higher energy scales, whereas the Co system utilizes formate stretches. B-site substitution is thus a powerful tool for developing structure-property relations within chemically analogous materials, providing control of electronic and magnetic properties as well as energy scales.

Copper coordination polymers provide a second platform with which to extend our work. Magneto-infrared spectra of $[\text{Cu}(\text{pyz})_2(2\text{-HOpy})_2](\text{PF}_6)_2$ and $[\text{Cu}(\text{pyz})_{1.5}(4\text{-HOpy})_2](\text{ClO}_4)_2$, combined with prior work of other copper complexes,

allow for the investigation of spin-lattice coupling across magnetic quantum phase transitions as a function of structural and magnetic dimensionality. Spin-phonon coupling strength versus magnetic dimensionality reveals that coupling is maximized in the ladder complex. These findings are applicable to other materials with field-induced transitions from the antiferromagnetic to fully saturated state.

Multiferroic $(\text{NH}_4)_2[\text{FeCl}_5 \cdot (\text{H}_2\text{O})]$ is our final test case, sporting a complex network of hydrogen and halogen bonds. The high-field polarization change is quenched at the quasicollinear- to collinear-sinusoidal magnetic reorientation, collapsing before magnetic saturation. Remarkably, nearly all low-frequency modes distort to facilitate the development of the magnetic quantum phase, entirely different than most other molecule-based magnets. Signatures of electron-phonon coupling emerge through magneto-infrared measurements.

Together, these findings elucidate quantum phase transitions, spin-lattice coupling, and structure-property relations in molecular multiferroics and quantum magnets, motivating further exploration of non-equilibrium phases in these materials.

Table of Contents

| | | |
|----------|--|-----------|
| 1 | Introduction: Vibrational properties of molecule-based magnetic materials | 1 |
| 2 | Literature survey | 11 |
| 2.1 | Multifunctional and multiferroic materials | 11 |
| 2.1.1 | Multiferroic materials | 11 |
| 2.1.2 | Molecular multiferroics vs oxide multiferroics | 15 |
| 2.1.3 | Magnetoelastic coupling | 17 |
| 2.2 | Magnetism and magnetically-driven phase transitions | 19 |
| 2.2.1 | Exchange pathways | 21 |
| 2.2.2 | Goodenough-Kanamori-Anderson rules | 23 |
| 2.3 | Hydrogen and halogen bonding | 25 |
| 2.4 | Classical versus quantum phase transitions | 28 |
| 2.4.1 | Magnetic field drives magnetic quantum phase transitions . . | 33 |
| 2.5 | Materials of interest in this work | 37 |
| 2.5.1 | $[(\text{CH}_3)_2\text{NH}_2]M(\text{HCOO})_3$ ($M=\text{Mn}^{2+}$, Co^{2+} , Ni^{2+}) molecule-based magnets | 37 |
| 2.5.2 | $[\text{Cu}(\text{pyz})_2(2\text{-HOpy})_2](\text{PF}_6)_2$ and $[\text{Cu}(\text{pyz})_{1.5}(4\text{-HOpy})_2](\text{ClO}_4)_2$ copper halide complexes | 41 |
| 2.5.3 | Hydrogen-bonded multiferroic $(\text{NH}_4)_2[\text{FeCl}_5\cdot(\text{H}_2\text{O})]$ | 45 |

| | | |
|----------|---|-----------|
| 3 | Methods | 50 |
| 3.1 | Optical spectroscopy | 50 |
| 3.1.1 | Maxwell's equations | 51 |
| 3.1.2 | The harmonic oscillator and infrared spectroscopy | 55 |
| 3.1.2.1 | Lattice dynamics calculations of solids | 61 |
| 3.2 | Spectroscopic instrumentation | 62 |
| 3.2.1 | Fourier transform spectroscopy | 62 |
| 3.2.2 | Bruker IFS 113v Fourier transform infrared spectrometer . . . | 64 |
| 3.2.3 | Bruker Equinox 55 FTIR spectrometer with Bruker IR Scope II | 65 |
| 3.3 | Measurements under extreme conditions | 66 |
| 3.3.1 | Magnetometry | 66 |
| 3.3.2 | Pulsed-field polarization | 68 |
| 3.3.3 | Spectroscopy under extremes | 69 |
| 3.3.3.1 | Variable temperature spectroscopy | 69 |
| 3.3.3.2 | Magneto-infrared techniques | 71 |
| 3.3.3.3 | High pressure infrared spectroscopy | 73 |
| 3.4 | Materials of interest: sample preparation and complementary calcu- lations | 75 |
| 3.4.1 | Synthetic procedures | 75 |
| 3.4.2 | Magnetometry | 76 |
| 3.4.3 | Pulsed-field polarization | 76 |
| 3.4.4 | Infrared transmittance measurements | 77 |
| 3.4.5 | Magneto-infrared experiments | 77 |
| 3.4.6 | Lattice dynamics calculations | 78 |
| 4 | Phonon mode links ferroicities in multiferroic $[(\text{CH}_3)_2\text{NH}_2]\text{Mn}(\text{HCOO})_3$ | 79 |

| | | |
|----------|--|------------|
| 4.1 | Understanding the lattice dynamics of $[(\text{CH}_3)_2\text{NH}_2]\text{Mn}(\text{HCOO})_3$ as a function of temperature | 80 |
| 4.2 | Spin-lattice coupling across the magnetically-driven transition in $[(\text{CH}_3)_2\text{NH}_2]\text{Mn}(\text{HCOO})_3$ | 82 |
| 5 | Structure-property relations in multiferroic $[(\text{CH}_3)_2\text{NH}_2]M(\text{HCOO})_3$ ($M=\text{Mn, Co, Ni}$) | 87 |
| 5.1 | Developing magnetic field-temperature phase diagrams | 88 |
| 5.2 | Vibrational properties of this family of hybrid organic-inorganic perovskites across the ferroelectric transition | 91 |
| 5.3 | Magnetoelastic coupling and the metal center | 97 |
| 6 | Spin-lattice coupling across the magnetic quantum phase transition in Cu-containing coordination polymers | 101 |
| 6.1 | Development of low temperature hydrogen bonding | 102 |
| 6.2 | Spin-lattice coupling across the magnetic quantum phase transition . | 105 |
| 6.3 | Pressure-induced structural phase transitions in Cu-containing coordination polymers | 109 |
| 6.4 | Supporting information | 112 |
| 7 | Observation of magnetoelectric, spin-lattice, and electron-phonon coupling in multiferroic $(\text{NH}_4)_2[\text{FeCl}_5 \cdot (\text{H}_2\text{O})]$ | 116 |
| 7.1 | Electric polarization across the magnetic quantum phase transition . | 117 |
| 7.2 | Lattice distortions through the order-disorder phase and the magnetic quantum phase transition | 119 |
| 7.3 | Microscopic signatures of charge-spin-lattice coupling | 124 |
| 8 | Summary and outlook | 127 |

Bibliography 132

Vita 153

List of Tables

| | | |
|-----|--|----|
| 1.1 | Scientific problems and important findings in this dissertation. | 7 |
| 2.1 | Summary of important direct and corresponding inverse magnetoelastic effects. | 17 |
| 2.2 | Critical exponents (β , γ , δ) for various models. | 30 |
| 2.3 | Comparison of important properties in $[(\text{CH}_3)_2\text{NH}_2]M(\text{HCOO})_3$ ($M=\text{Mn}^{2+}$, Co^{2+} , Ni^{2+}). Here, P is the polarization, J is the dominant exchange energy (calculated according to molecular field theory [126] as well as DFT) and other symbols are defined in the caption of Figure 1. Parameters measured in other works are cited, whereas ‡ indicates values derived in this dissertation. [120] | 40 |
| 2.4 | Summary of properties comparing $[\text{Cu}(\text{pyz})_2(2\text{-HOpy})_2](\text{PF}_6)_2$ and $[\text{Cu}(\text{pyz})_{1.5}(4\text{-HOpy})_2](\text{ClO}_4)_2$. Values derived in this work are labeled with a ‡. | 45 |
| 3.1 | Operating parameters for the Bruker IFS 113v. | 66 |
| 3.2 | Important parameters of operation for the Bruker IRscope II. | 68 |
| 4.1 | Frequencies and assignments for important modes in $[(\text{CH}_3)_2\text{NH}_2]\text{Mn}(\text{HCOO})_3$ at 300 and 4 K. | 80 |

5.1 Comparison of theoretical [64] critical exponents ν for the power law fit $A(T_C - T)^\nu$ along with exponents extracted from the Mn and Ni data above. The values suggest that the Mn system is more two-dimensional (being closer to the predicted Heisenberg and Ising exponents), while the Ni material is closer to the mean-field, three-dimensional predictions. [120] 95

6.1 Summary of magneto-active vibrations in $[\text{Cu}(\text{pyz})_2(2\text{-HOpy})_2](\text{PF}_6)_2$ and $[\text{Cu}(\text{pyz})_{1.5}(4\text{-HOpy})_2](\text{ClO}_4)_2$. We show the percent changes of absorption across the quantum critical transition of these modes, along with field-induced frequency shifts and corresponding spin-phonon coupling constants. These are related as $\omega \approx \omega_0 + \lambda \langle S_i \cdot S_j \rangle$. Here, λ is the spin-phonon coupling constant. 107

List of Figures

| | | |
|-----|--|---|
| 1.1 | (a) Magnetization curve of the spin-ladder complex $(5\text{IAP})_2\text{CuBr}_4 \cdot 2\text{H}_2\text{O}$, revealing the spin gap transition and the fully saturated magnetic state. [17] | |
| | (b) Quantum tunneling of magnetization in the single-molecule magnet Mn_{12} -acetate. [18] | |
| | (c) Phase diagram of the bimetallic quantum magnet $[\text{Ru}_2(\text{O}_2\text{CMe})_4]_3[\text{Cr}(\text{CN})_6]$, revealing the pressure-driven spin-crossover transition. [19] | 3 |

| | | |
|-----|--|----|
| 1.2 | <p>Summary of the spectroscopic and crystallographic response of several molecule-based materials under tuning parameters such as magnetic field, temperature, and pressure. (a) Magnetization curves as a function of temperature for $[(\text{CH}_3)_2\text{Mn}(\text{HCOO})_3]$. [30] (b) Low temperature magnetic structures at different magnetic fields in the molecular multiferroic $(\text{NH}_4)_2[\text{FeCl}_5 \cdot (\text{H}_2\text{O})]$. [28] (c) Infrared spectra as a function of temperature of DMACoF, revealing the disappearance of modes near 170 K and the development of the ferroelectric phase. [34] (d) Polar vs paraelectric states in $\text{HHTP} \cdot 4\text{H}_2\text{O}$; below T_C, the majority of sites share the same order parameter whereas above T_C, there is an equal population of both states. [35] (e) Summary of how the saturation fields and the exchange parameters change in $\text{CuF}_2(\text{H}_2\text{O})_2(\text{pyz})$ as a function of pressure. [31] (f) Pressure-driven Jahn-Teller reorientations in $[\text{CuF}_2(\text{H}_2\text{O}_2(\text{pyz}))]$ [33] (g) Spectroscopic response of $\text{CuF}_2(\text{H}_2\text{O})_2(3\text{-chloropyridine})$ as a function of pressure, where the different colors denote new phase transitions. [36]</p> | 5 |
| 2.1 | <p>Schematic of multiferroic control. Ferrotoroidicity, ferromagnetism, ferroelectricity, and ferroelasticity are depicted with respect to time-reversal and space-inversion symmetries. [52]</p> | 13 |
| 2.2 | <p>Schematic of a perovskite oxide above and below the ferroelectric transition. Applied electric field shifts the central atom to an off-center position, inducing ferroelectricity.</p> | 14 |

| | | |
|-----|---|----|
| 2.3 | Ordering of spins in magnetic materials. PM represents paramagnetism, FM represents a material in the ferromagnetic state, AFM stands for antiferromagnetism, FiM symbolizes ferrimagnetism, and NC-AFM stands for non-collinear antiferromagnetism like cycloidal, spiral, or canted antiferromagnets. | 19 |
| 2.4 | Symmetry relations for overlapping orbitals in octahedral environments that share either (a) a common edge or (b) a common face. These conformations display direct exchange interactions, as there is no need for an intermediary. [85] | 21 |
| 2.5 | Summary of the semi-empirical Goodenough-Kanamori rules. Both antiferromagnetic and ferromagnetic superexchange pathways are depicted. [85] | 24 |
| 2.6 | (a) Two neighboring d sites with an oxygen ion in between. The wavy lines represent virtual hoppings of a d hole from one site to the other via p levels. The numbers give one possible sequence of consecutive hoppings. This energy corresponds to J . (b) Another sequence of hoppings that transfers a d hole from each metal to the p , so that there are two holes at the same oxygen. This energy corresponds to J' . [89] | 26 |
| 2.7 | Summary of hydrogen bonded molecular magnetic materials. [90, 92–94] | 27 |
| 2.8 | General phase diagram near the vicinity of a quantum critical point (labelled QCP) as a function of both a control parameter g and temperature T . When $r < 0$ and temperature is low, the material is in an ordered state. At $T=0$ K and $r=0$, the quantum critical point exists. Above this, the system becomes quantum disordered. [99] | 31 |

| | | |
|------|--|----|
| 2.9 | (a) General phase diagram for a spin ladder complex. H_{c1} and H_{c2} are the quantum critical points corresponding to the spin gap and the fully saturated magnetic state, respectively. [106] (b) Saturation field and J exchanges as a function of pressure, revealing a magnetic transition. (c) Resistivity versus temperature at various doping concentrations of $\text{Pr}_{2-x}\text{Ce}_x\text{CuO}_{4-\delta}$. [108] (d) Temperature-hole density phase diagram of $\text{YBa}_2\text{Cu}_3\text{O}_7$. [109] | 32 |
| 2.10 | Summary of different magnetic quantum phase transitions in molecule-based materials including (a) magnetization saturation in $[\text{Cu}(\text{pyz})(\text{H}_2\text{O})(\text{gly})_2](\text{ClO}_4)_2$, (b) the B - T phase diagram of a quantum magnet $[\text{Cu}(\text{pyz})(\text{gly})](\text{ClO}_4)$ showing two quantum critical points, and (c) the microscopic mechanism that $[\text{Ni}(\text{HF}_2)(\text{pyz})_2]\text{SbF}_6$ undergoes to reach the quantum phase transition. [22, 32] | 33 |
| 2.11 | When magnetic field is applied parallel to the sublattice magnetization, (a) the spins are unaffected at low fields and (b) at a critical field, the system undergoes a spin-flop transition. [64] | 34 |
| 2.12 | Energies of the antiferromagnetic and spin-flop phases as a function of increasing magnetic field. | 36 |

| | | |
|------|--|----|
| 2.13 | (a) Crystal structure of $[(\text{CH}_3)_2\text{NH}_2]M(\text{HCOO})_3$ ($M=\text{Mn}^{2+}$, Co^{2+} , Ni^{2+}) at room temperature showing the metal centers, formate ligands, and disordered dimethylammonium. [56] (b) Electronic and spin states for the various metal centers. (c) Close-up view of the dimethylammonium counterion in the low-temperature, ordered state. (d) Temperature and magnetic field energy scales showing the characteristic transitions. cAFM = canted antiferromagnet, PM = paramagnet, FE = ferroelectric, PE = paraelectric, B_{SF} = spin flop field, and B_{C} = saturation field. [120] | 38 |
| 2.14 | (a) Electric polarization in $[(\text{CH}_3)_2\text{NH}_2]\text{Mn}(\text{HCOO})_3$ was applied in conjunction with magnetic fields of 0, 7, and 13 T. It is clear that ferroelectricity improves with application of magnetic fields, showing a direct magnetoelectric effect. [37] (b) Heat capacity of $[(\text{CH}_3)_2\text{NH}_2]\text{Mn}(\text{HCOO})_3$ reveals the structural and magnetic transitions. [56] Similar results are seen in the Ni^{2+} and Co^{2+} complexes, albeit at different energy scales. | 39 |
| 2.15 | Magnetic field-temperature phase diagram of $[(\text{CH}_3)_2\text{NH}_2]\text{Mn}(\text{HCOO})_3$, highlighting the canted antiferromagnetic (cAFM), canting, fully polarized, and paramagnetic (PM) regions. [30] Long-range interactions fall off above the Néel transition at 8.5 K. | 41 |

| | | |
|------|--|----|
| 2.16 | (a) Magnetization versus temperature of $[(\text{CH}_3)_2\text{NH}_2]\text{Co}(\text{HCOO})_3$ at 4 and 1 T. The jump in magnetization coincides with the structural transition, indicating a possible change in the magnetic moment of the Co^{2+} ion. [40] (b) Temperature dependence of the ac susceptibility in $[(\text{CH}_3)_2\text{NH}_2]\text{Co}(\text{HCOO})_3$, showing two transitions at 15.1 K and 11 K. The shift in frequency of the 11 K peak is indicative of glassy nature or magnetic frustration between two competing magnetic phases. [125] | 42 |
| 2.17 | Summary of Cu halide complexes as a function of increasing dimensionality. | 43 |
| 2.18 | (a) Crystal structure of $[\text{Cu}(\text{pyz})_2(2\text{-HOpy})_2](\text{PF}_6)_2$ emphasizing the layered, infinitely extending Cu^{2+} planes. (b) View of the ladder structure $[\text{Cu}(\text{pyz})_{1.5}(4\text{-HOpy})_2](\text{ClO}_4)_2$. Exchange strengths of the rung vs rail are indicated. [148] | 44 |
| 2.19 | (a) Crystal structure of $(\text{NH}_4)_2[\text{FeCl}_5(\text{H}_2\text{O})]$. Hydrogen-bonding interactions ($\text{O-H}\cdots\text{Cl}$) govern the herringbone-like connectivity. [61] (b) Summary of the various exchange pathways mediated by hydrogen- and ionic-bonding, along with the strength of each pathway. (c) Summary of the important temperature- and field-driven transitions. $T_{\text{o/d}}$ is a reported order/disorder transition, T_{S} is an isostructural distortion, and T_{N} and T_{FE} give the Néel and ferroelectric transitions, respectively. Along the field axis, B_{SR1} and B_{SF} are the low-field spin reorientation and spin-flop transitions; B_{SR2} and B_{C} are the high-field spin reorientation and the saturation field. [61] | 46 |

| | | |
|------|---|----|
| 2.20 | (a) Low field B - T phase diagram of $(\text{NH}_4)_2[\text{FeCl}_5 \cdot (\text{H}_2\text{O})]$, highlighting the different ferroelectric phases. [61] (b) Full B - T phase diagram, including the small spin reorientations that lead up to magnetic saturation. [90] | 47 |
| 2.21 | (a-c) Temperature dependences of spontaneous electric polarization P_a for magnetic fields applied parallel to the a , b and c axes. (d) Magnetization versus magnetic field applied parallel to a , b and c . (e) Magnetic field dependence of the electric polarization P_a , P_b , and P_c as a function of magnetic field. [61] | 49 |
| 3.1 | Potential wells of the harmonic oscillator and the anharmonic (Morse) potential. | 56 |
| 3.2 | Dispersion curves for optical and acoustic branches. | 60 |
| 3.3 | Experiments were carried out on a variety of spectrometers including (a) far-infrared measurements on the Bruker IFS 113v (20 - 700 cm^{-1}) and (b) middle-infrared measurements on the Bruker Equinox 55 with Bruker IR Scope II attachment (500 - 5000 cm^{-1}). | 63 |
| 3.4 | (a) Schematic view of a Michelson interferometer. The beamsplitter divides the source beam and sends signals to the movable mirror M_1 and the fixed mirror M_2 . These beams are reflected and brought back together, resulting in an interference pattern at the detector. (b) The combination of two signals yields the interference pattern, which is plotted as power versus time. | 64 |
| 3.5 | Schematic view of the Bruker IFS 113v FTIR spectrometer. | 65 |
| 3.6 | Optical path of Bruker IRscope II. | 67 |
| 3.7 | Schematic of the LT-3-110 Heli-Tran open flow cryostat in a low-temperature setup. | 70 |

| | | |
|------|---|----|
| 3.8 | Cryostats used for optical measurements on (a) the Bruker 113v and (b) the Bruker Equinox 55 FTIR spectrometer with Bruker IR Scope II attachment. | 71 |
| 3.9 | Summary of the low-temperature setup for the Bruker Equinox 55. | 72 |
| 3.10 | Schematic view of the 35 T Resistive Magnet at the National High Magnetic Field Laboratory in Tallahassee, FL. | 74 |
| 3.11 | (a) Pictures and (b) schematic representation of a diamond anvil cell. [170] | 75 |
| 4.1 | (a) Infrared response of $[(\text{CH}_3)_2\text{NH}_2]\text{Mn}(\text{HCOO})_3$ at room temperature and displacement pattern of formate bending mode. Inset: low frequency region of the spectra which has mostly Mn-containing modes. (b) Close-up view of the infrared-active formate bending mode. (c) Frequency versus temperature plot that reveals doublet splitting of the formate bending mode across T_C . An anharmonic fit of the high temperature data points reveals the behavior of the unperturbed phonon. Error bars are on the order of the symbol size. (d) Splitting of the formate bending mode vs. temperature, a power law fit to this data, and polarization from Ref. Wang2013. (e) Width of the hysteresis around T_C vs. cooling rate. The loop closes when the cooling rate is $< \approx 0.2$ K/min. Inset: hysteresis of the C-N-C asymmetric bending mode at 0.5 K/min. | 81 |

| | | |
|-----|--|----|
| 4.2 | <p>(a) Close-up view of the absolute absorption spectrum focusing on the formate bending mode (displacement shown in schematic) at 0 and 35 T at 4.2 K along with the full field absorption difference spectrum. (b) Absorption difference spectra, $\Delta\alpha = \alpha(\omega, B) - \alpha(\omega, B = 0)$, showing field-induced changes in the formate bending mode for fields up to 35 T. The scale bar is 500 cm^{-1}. (c) Absorption spectrum of the 1030 cm^{-1} amine stretching mode at 0 T and 35 T along with the full field absorption difference spectrum, revealing the lack of field dependence in the couterion mode. (d) Normalized magnetization [30], square of the magnetization, and integrated absorption difference as functions of applied field. (e) Schematic of the field-induced local lattice distortion of the formate ligand.</p> | 83 |
| 5.1 | <p>(a-c) Pulsed field magnetization of $[(\text{CH}_3)_2\text{NH}_2]M(\text{HCOO})_3$ ($M = \text{Mn}^{2+}, \text{Co}^{2+}, \text{Ni}^{2+}$) up to 65 T at different temperatures. Derivatives of this data reveal B_{SF} as shown in the lower insets. Only the Mn compound has a clear saturation field under these conditions. [30] The Ni and Co systems are not saturated even at 65 T. (d-f) Magnetic field-temperature phase diagrams developed from the pulsed field magnetization data. Orange points follow the transition to the fully saturated magnetic state, and pink points track the spin flop. The high field phase boundaries for the Ni and Co compounds are estimated as described in the text. Error bars are on the order of the symbol size. cAFM = canted antiferromagnet and PM = high temperature paramagnetic state. [120]</p> | 89 |

| | | |
|-----|--|----|
| 5.2 | (a-c) Close-up views of the formate bending mode (left) and C-N-C stretch (right) for the Mn, Ni, and Co analogs as a function of temperature. Insets show low frequency modes. (d-f) Frequency vs. temperature plots for these features, highlighting the difference in behavior of the Mn and Ni complexes versus the Co system. T_C and T_N are indicated by purple vertical lines. The fit to the high temperature phase data described in the text represents the behavior of the hypothetical unperturbed phonons below T_C . [120] | 92 |
| 5.3 | (a) Splitting of the formate bending mode vs. temperature in the Mn complex, a power law fit to this data, and polarization from Ref. 37, along with a corresponding power law fit. (b) Overlay of the formate bending mode splittings in the Mn and Ni complexes, along with their power law fits and extracted critical exponents. (c) Calculated cooling rate of the C-N-C stretch along with an extended power law fit. [120] | 93 |
| 5.4 | (a-c) Absolute absorption spectra at 0 and 35 T for the $[(CH_3)_2NH_2]M(HCOO)_3$ materials along with waterfall plots of the absorption difference at 4.2 K highlighting spectral changes in applied magnetic field. The Mn system sports field-induced changes in the formate bending mode, whereas the symmetric O-C-O stretch is important for the Co compound. The Ni analog displays no field-dependent vibrational modes up to 35 T. (d-f) Absolute value of the absorption difference integrated over a small energy window vs. magnetic field along with the 4 K magnetization and the square of the magnetization. Error bars are indicated. [120] | 98 |

| | | |
|-----|---|-----|
| 6.1 | <p>(a) Infrared absorption of $[\text{Cu}(\text{pyz})_2(2\text{-HOpy})_2](\text{PF}_6)_2$ and $[\text{Cu}(\text{pyz})_{1.5}(4\text{-HOpy})_2](\text{ClO}_4)_2$ at 300 and 4 K. Insets show the low frequency regions. (b,c) Close-up view of the pyridone (py) and pyrazine-containing (pyz) quartet in $[\text{Cu}(\text{pyz})_2(2\text{-HOpy})_2](\text{PF}_6)_2$ along with the corresponding peak position vs temperature trends. Specifically, we highlight the differences between hydrogen-bonded modes and anharmonic modes. (d,e) Close-up view of the same region in $[\text{Cu}(\text{pyz})_{1.5}(4\text{-HOpy})_2](\text{ClO}_4)_2$. (f) Calculated displacement patterns of the out-of-plane pyrazine distortion and in-phase pyrazine ring bend.</p> | 103 |
| 6.2 | <p>(a,d) Absorption (at 4.2 K) of $[\text{Cu}(\text{pyz})_2(2\text{-HOpy})_2](\text{PF}_6)_2$ and $[\text{Cu}(\text{pyz})_{1.5}(4\text{-HOpy})_2](\text{ClO}_4)_2$ at 0 and 35 T along with the 35 T absorption difference spectra. Vertical gray boxes highlight field-induced changes. (b,e) Absorption differences of the magneto-active modes with increasing magnetic field. (c,f) Overlay of magnetic-field-induced frequency shifts of the out-of-plane pyrazine distortions plotted with the 1.5 K magnetization [148] and the square of magnetization. The data sets are normalized above the critical field, B_C. (g) Comparison of spin-phonon coupling constant of the out-of-plane pyrazine distortion as a function of magnetic dimensionality in several well known Cu-containing coordination complexes.</p> | 106 |

| | | |
|-----|--|-----|
| 6.3 | (a,c) Close-up views of the 300 K infrared spectra as a function of pressure for $[\text{Cu}(\text{pyz})_2(2\text{-HOpy})_2](\text{PF}_6)_2$ and $[\text{Cu}(\text{pyz})_{1.5}(4\text{-HOpy})_2](\text{ClO}_4)_2$, respectively. The spectra are offset for clarity. The vertical green regions highlight pressure-driven distortions. (b,d) Frequency vs. pressure trends for the modes displayed in (a,c). Critical pressures P_C are indicated by vertical red lines. The gray areas indicate the point at which each system becomes amorphous (Supporting Information). | 110 |
| 6.4 | Comparison of several copper-containing coordination polymers in the relevant frequency range. We highlight a number of similarities between these complexes including pyrazine-, pyridone-, HOpy, and BF_4^- - and ClO_4^- -related modes. Our goal is to assign vibrations in $[\text{Cu}(\text{pyz})_{1.5}(4\text{-HOpy})_2](\text{ClO}_4)_2$ and $[\text{Cu}(\text{pyz})_2(2\text{-HOpy})_2](\text{PF}_6)_2$ (dark blue and red spectra on the bottom.) | 114 |
| 6.5 | (a) Infrared absorption and (b, c) Raman scattering spectra of two-dimensional $[\text{Cu}(\text{pz})_2(2\text{-OHpy})_2](\text{PF}_6)_2$ below P_C , above P_C , and in the disordered phase. (d-f) Corresponding spectra for ladder-like $[\text{Cu}(\text{pz})_{1.5}(4\text{-OHpy})_2](\text{ClO}_4)_2$. All data are taken at room temperature, and the spectra are offset for clarity. | 115 |

| | | |
|-----|---|-----|
| 7.1 | <p>(a) Change in electric polarization (ΔP) of $(\text{NH}_4)_2[\text{FeCl}_5 \cdot (\text{H}_2\text{O})]$ as a function of magnetic field at various temperatures. This is the $P a, B c$ configuration. Others are given in Supplemental Information.</p> <p>(b) Magnetoelectric current I vs B, highlighting changes in $\Delta P(B)$.</p> <p>(c) B-T phase diagram of $(\text{NH}_4)_2[\text{FeCl}_5 \cdot (\text{H}_2\text{O})]$; points taken from the magnetoelectric current measurement are indicated in light blue. [90]</p> <p>A color bar is included to illustrate the strength of ΔP with field – red signifies a strong response and white represents zero polarization.</p> | 118 |
| 7.2 | <p>Frequency vs temperature plots of several important modes, emphasizing the differences in behavior as a function of temperature.</p> | 121 |
| 7.3 | <p>(a) Absorption of $(\text{NH}_4)_2[\text{FeCl}_5 \cdot (\text{H}_2\text{O})]$ at 0 at 35 T in the low-frequency regime along with the 35 T absorption difference spectrum, $\Delta\alpha = \alpha(35 \text{ T}) - \alpha(0 \text{ T})$. All vibrations in this region are magneto-active. (b) Analysis of percent changes of absorption across the magnetic quantum phase transition. (c) Overlay of the integrated area of several magneto-active vibrations along with the low-temperature magnetization [90] and the square of magnetization. The magnetic saturation region is shown by the vertical gray box.</p> | 122 |
| 7.4 | <p>Comparison of the absolute value of the absorption differences of two important magneto-infrared distortions, magnetization [90], the square of magnetization, and ΔP of $(\text{NH}_4)_2[\text{FeCl}_5 \cdot (\text{H}_2\text{O})]$. [90] All data were acquired at low temperature (below T_N and T_{FE}) and are normalized to the P or M saturation fields. $\Delta P(B)$ goes to zero at 26 T, and magnetization saturates at 30 T. The magneto-infrared data tracks $[M(B)]^2$, but small signatures of the ΔP transitions are also apparent in the infrared data as deviations from this trend.</p> | 125 |

Chapter 1

Introduction: Vibrational properties of molecule-based magnetic materials

Equipped with flexible architectures and overall low energy scales, molecule-based magnetic materials offer fundamental insight into the behavior of high energy oxides along with the unique opportunity to fully investigate the interplay between structure and magnetism. With control and improvement of molecular building blocks and structural and magnetic connectivities, molecule-based magnets demonstrate an extensive list of useful properties such as room temperature ferromagnetism, tunable ferroelectric transitions, quantum tunneling, and dimensionality switching – just to name a few. [1–5] Their available structural motifs range from zero-dimensional, isolated molecules to one- and two-dimensional chains and planes to three-dimensional extending networks. Moreover, by modifying stoichiometry and chemical composition, both hydrogen-bonding interactions and spin exchange pathways can be altered, providing routes toward tunable structural and magnetic dimensionalities. [6–8]

One important way to develop molecule-based materials is through the introduction of building blocks capable of hydrogen bonding. [9, 10] Surprisingly, although hydrogen bonds are generally very weak intermolecular bonds, they can mediate magnetic exchange, induce ferroelectricity, and drastically alter the overall extending structure of a system. [11–13] A prominent example of this effect is in the frustrated three-leg ladder complex $[(\text{CuCl}_2\text{tachH})_3\text{Cl}]\text{Cl}_2$, in which hydrogen-bonded super-exchange interactions between frustrated triangles turn out to be even stronger than the shorter Cu-Cu interactions within the triangle. [14] In the hybrid perovskite $(\text{C}_2\text{H}_5\text{NH}_3)_2\text{CuCl}_4$, ferroelectricity is induced by hydrogen-bond ordering of organic chains below the Curie temperature. [15] Strong $\text{H}\cdots\text{F}$ bonds can even act as ligands in the self assembly of novel quantum magnetic solids such as $[\text{Cu}_2(\text{HF}_2)(\text{pyz})_2]\text{SbF}_6$. [16] In this dissertation, I examine an extensive set of copper-containing coordination polymers with various degrees of dimensionality – due in large part to differences in hydrogen bonding – in order to investigate spin-phonon coupling constants as a function of magnetic field. Additionally, we explore the magnetic and ferroelectric aspects of two important families of molecule-based multiferroics, one of which has a structure and magnetic exchange interaction governed solely by hydrogen- and halogen-bonding interactions.

The low energy scales in molecular magnets provide easy opportunities for unveiling complex quantum phenomena that arise in these systems. Quantum properties and phases are different from traditional phase transitions in that they are driven by a physical tuning parameter like magnetic field, composition, or pressure rather than by thermal fluctuations. [20–24] Those involving applied field are among the most well-studied. For example, spin-ladder complexes like $(5\text{IAP})_2\text{CuBr}_4\cdot 2\text{H}_2\text{O}$ undergo low field spin gap transitions Δ and then a magnetic saturation B_C at higher fields [Fig. 1.1 (a)]. [25] These are quantum phase transitions because the critical

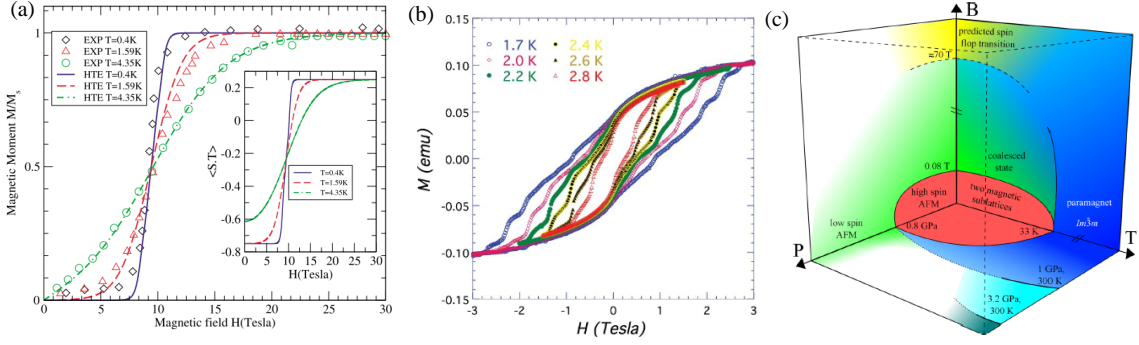


Figure 1.1: (a) Magnetization curve of the spin-ladder complex $(5\text{IAP})_2\text{CuBr}_4 \cdot 2\text{H}_2\text{O}$, revealing the spin gap transition and the fully saturated magnetic state. [17] (b) Quantum tunneling of magnetization in the single-molecule magnet Mn_{12} -acetate. [18] (c) Phase diagram of the bimetallic quantum magnet $[\text{Ru}_2(\text{O}_2\text{CMe})_4]_3[\text{Cr}(\text{CN})_6]$, revealing the pressure-driven spin-crossover transition. [19]

exponents extracted from scaling functions before and after Δ and B_C are inherently different. Moreover, the transitions occur at experimentally realizable fields. [17] In the single-molecule magnet Mn_{12} -acetate, quantum tunnelling of the magnetization is observed (as a staircase structure) at low temperatures [Fig. 1.1 (b)]. [18] Pressure can also drive new quantum phases away from equilibrium, as is the case for the bimetallic quantum magnet $[\text{Ru}_2(\text{O}_2\text{CMe})_4]_3[\text{Cr}(\text{CN})_6]$. At 1 GPa, the material undergoes a spin crossover transition from a high \rightarrow low spin state. [19] In the metal-organic system $[\text{CuF}_2(\text{H}_2\text{O})_2]_2\text{pyz}$, a giant pressure dependence of the magnetic exchange (involving the reorientation of magnetic orbitals) is observed. [5] In the materials discussed in this dissertation, we observe field-driven magnetic quantum phase transitions at experimentally realizable energy scales due to the molecular nature of the systems and investigate the microscopic properties across them. By doing so, we reveal the specific local lattice distortions that accompany these quantum phase transitions.

Although most molecule-based materials have been well-studied with bulk techniques such as magnetic susceptibility, magnetometry, and polarization, spectroscopy

offers a complementary opportunity to investigate properties, as it is a microscopic probe of local structure and dynamics. Furthermore, it is well-suited for studying materials under extremes. This is because tuning parameters such as magnetic field, pressure, and temperature alter the local bond lengths and angles. Figure 1.2 summarizes the spectroscopic and crystallographic response of several molecule-based materials under the aforementioned tuning parameters. With applied magnetic field, materials can be driven through new magnetic states such as metal-insulator phase transitions, spin-flop transitions, cycloidal \rightarrow collinear transitions, and quantum critical phases. [26–30] In all of these cases, magnetization saturates at a finite field – the mechanisms that materials undergo to arrive at that state, however, are altogether unique and provide insight into the underlying magnetic ordering in molecule-based systems towards the design of novel magnetic complexes [Fig. 1.2 (a,b)]. Applied pressure can also trigger non-equilibrium phases. In the coordination polymer $\text{CuF}_2(\text{H}_2\text{O})_2(\text{pyrazine})$, pressure induces a change in dimensionality from a quasi-two-dimensional to a quasi-one-dimensional state via a Jahn-Teller rotation. [31] In both $[\text{CuF}_2(\text{H}_2\text{O})_2(\text{pyz})]$ and $\text{CuF}_2(\text{H}_2\text{O})_2(3\text{-chloropyridine})$ applied pressure leads to a spin-crossover transition. [Fig. 1.2 (e-g)]. [32, 33] Finally, although not formally categorized as a quantum transition, temperature also drives unique phases in quantum materials. For example, a ferroelectric phase transition is observed in DMACoF (DMA = dimethylammonium), evidenced by a disappearance of features above 170 K. [34] Additionally, in $\text{HHTP}\cdot 4\text{H}_2\text{O}$ (HHTP = hexahydroxytriphenylene), temperature drives a hydrogen-bonded order-disorder transition into a polar phase [Fig. 1.2 (c,d)]. [35]

In this dissertation, I explore the vibrational properties of several multiferroics and quantum magnets including the hybrid organic-inorganic perovskite family $[(\text{CH}_3)_2\text{NH}_2]M(\text{HCOO})_3$ ($M=\text{Mn,Co,Ni}$), two novel copper-containing coordina-

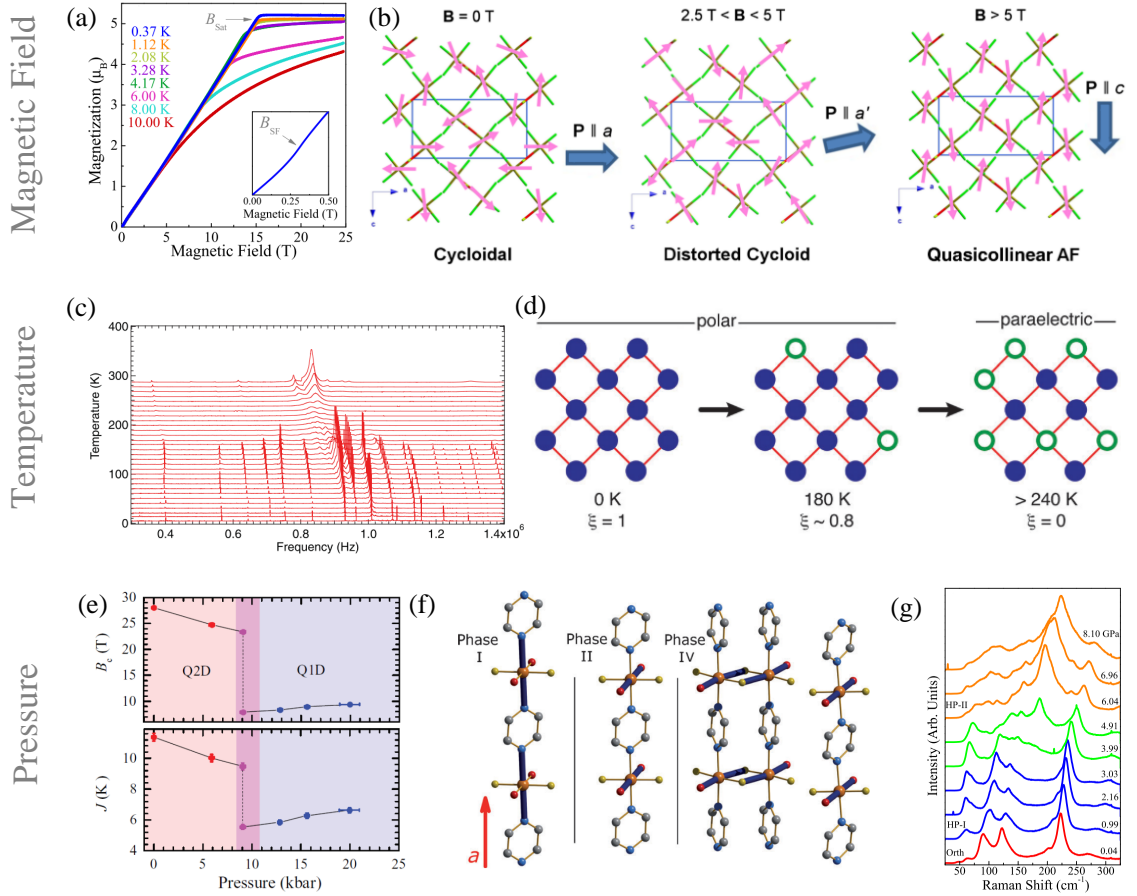


Figure 1.2: Summary of the spectroscopic and crystallographic response of several molecule-based materials under tuning parameters such as magnetic field, temperature, and pressure. (a) Magnetization curves as a function of temperature for $[(\text{CH}_3)_2\text{Mn}(\text{HCOO})_3]$. [30] (b) Low temperature magnetic structures at different magnetic fields in the molecular multiferroic $(\text{NH}_4)_2[\text{FeCl}_5 \cdot (\text{H}_2\text{O})]$. [28] (c) Infrared spectra as a function of temperature of DMACoF, revealing the disappearance of modes near 170 K and the development of the ferroelectric phase. [34] (d) Polar vs paraelectric states in $\text{HHTP} \cdot 4\text{H}_2\text{O}$; below T_C , the majority of sites share the same order parameter whereas above T_C , there is an equal population of both states. [35] (e) Summary of how the saturation fields and the exchange parameters change in $\text{CuF}_2(\text{H}_2\text{O})_2(\text{py}_2)$ as a function of pressure. [31] (f) Pressure-driven Jahn-Teller reorientations in $[\text{CuF}_2(\text{H}_2\text{O})_2(\text{py}_2)]$ [33] (g) Spectroscopic response of $\text{CuF}_2(\text{H}_2\text{O})_2(3\text{-chloropyridine})$ as a function of pressure, where the different colors denote new phase transitions. [36]

tion complexes $[\text{Cu}(\text{pyz})_2(2\text{-HOpy})_2](\text{PF}_6)_2$ and $[\text{Cu}(\text{pyz})_{1.5}(4\text{-HOpy})_2](\text{ClO}_4)_2$, and an entirely molecular multiferroic $(\text{NH}_4)_2[\text{FeCl}_5 \cdot (\text{H}_2\text{O})]$ under magnetic field, temperature, and pressure. Our findings are summarized in Table 1.1. Specifically, we focus on the interplay between spins and lattice excitations, an effect known as magnetoelastic coupling, where an applied magnetic field can modify the overall structure. The overall goal is to uncover the local lattice distortions that underlie unique phases such as ferroelectricity, spin-flop transitions, and field-driven quantum phases. Moreover, by tracking these microscopic changes with various tuning parameters, we understand the role of individual lattice distortions through the transitions. Interesting structure-property relations are unveiled through *B*-site substitution in the perovskite systems (in terms of the overall material energy scales for magnetic saturation) as well as through magnetic and structural dimensionality across the broader family of copper-containing coordination polymers. Overall, this dissertation explores the microscopic mechanisms of the development of unique material phases – namely magnetic quantum phase transitions – and motivates further exploration of functionality in non-equilibrium states.

In order to explore how different charge and spin states impact fundamental excitations of the lattice and the mechanisms that underlie the field dependent properties above T_N [37, 38], we measure the infrared vibrational response of $[(\text{CH}_3)_2\text{NH}_2]\text{Mn}(\text{HCOO})_3$ and compare our findings with complementary lattice dynamics calculations and prior magnetization measurements [30]. We find that doublet splitting of the formate bending mode across T_C functions as a ferroelectric order parameter and that, remarkably and counter-intuitively, the same phonon mode is sensitive to the development of the fully saturated magnetic state above 15.3 T. A single fundamental excitation in the form of a phonon thus underpins the development of the ferroic phases and magnetoelectric coupling - even though T_C and T_N are

Table 1.1: Scientific problems and important findings in this dissertation.

| Model Compound | Scientific Problem | Our Findings |
|--|--|--|
| $[(\text{CH}_3)_2\text{NH}_2]M(\text{HCOO})_3$ ($M=\text{Mn,Co,Ni}$) | <ul style="list-style-type: none"> • Lattice changes across the order-disorder ferroelectric transition • Spin-lattice coupling across/towards the magnetic quantum phase transition • <i>B</i>-site substitution to unveil structure property relations | <ul style="list-style-type: none"> • Formate bend links ferroicities in Mn complex • Mn and Ni materials adopt similar mechanisms in development of ferroelectricity; Co system reveals additional fine structure • <i>B</i>-site substitution of Ni and Co drastically alters magnetic energy scales • Mn and Ni utilize formate bend to reach magnetic saturation; Co introduces formate stretching distortions • Development of field-temperature phase diagrams |
| $[\text{Cu}(\text{pyz})_2(2\text{-HOpy})_2](\text{PF}_6)_2$ and $\text{Cu}(\text{pyz})_{1.5}(4\text{-HOpy})_2(\text{ClO}_4)_2$ | <ul style="list-style-type: none"> • Mechanism of hydrogen-bond development and spin-lattice coupling in copper-containing coordination polymers • Spin-phonon coupling strength as a function of magnetic dimensionality • Microscopic mechanism of pressure-induced structural transitions | <ul style="list-style-type: none"> • Hydrogen bonding more apparent in layered versus ladder material • Magnetoelastic coupling across magnetic quantum phase transition mediated by pyrazine-related distortions • Spin-phonon coupling strength reaches a maximum in spin ladder due to intermediate dimensionality • Subgroup analysis reveals high-pressure phase in ClO_4^- complex may be ferroelectric |
| $(\text{NH}_4)_2[\text{FeCl}_5 \cdot (\text{H}_2\text{O})]$ | <ul style="list-style-type: none"> • Coupling mechanism of polarization and spin at high magnetic fields • Correlation between bulk (polarization and magnetization) and microscopic (magneto-infrared spectroscopy) techniques • Structural distortions across the magnetic quantum phase transition | <ul style="list-style-type: none"> • High-field polarization quenching at quasicollinear \rightarrow collinear sinusoidal magnetic transition • Spin-lattice coupling across magnetic quantum phase transition involves majority of low-frequency modes • Observation of spin-phonon and electron-phonon coupling |

quite different. We anticipate that similar lattice entanglements with charge and spin may provide a controlled route to enhanced coupling and high temperature effects in other materials with coexisting electric and magnetic orders [39–42].

The discovery that $[(\text{CH}_3)_2\text{NH}_2]\text{Mn}(\text{HCOO})_3$ had an experimentally accessible magnetic quantum phase transition motivated our extension to the Co and Ni analogs. The overall goal was to explore how lattice distortions and magnetic energy scales change with *B*-site substitution. In addition to uncovering the magnetic field-temperature phase diagrams of $[(\text{CH}_3)_2\text{NH}_2]M(\text{HCOO})_3$ ($M=\text{Mn},\text{Co},\text{Ni}$), we unravel the microscopic details of the mechanisms involved in the development of ferroelectricity and the fully saturated magnetic state. The Mn and Ni complexes are overall quite similar, despite their large energy scale differences, whereas the Co analog displays strikingly different mechanisms in the development of polarization and the fully saturated magnetic state. These differences largely arise from distortions of the CoO_6 octahedra. Taken together, these findings reveal that *B*-site substitution is a powerful tool for the control of magnetic energy scales and the mechanisms that underlie ferroelectricity and magnetism.

Similar interactions – in simpler model systems – provide a platform with which to investigate structure-property relations. We combine infrared spectroscopy with several different physical tuning techniques to measure two copper-containing coordination polymers, $[\text{Cu}(\text{pyz})_2(2\text{-HOpy})_2](\text{PF}_6)_2$ and $[\text{Cu}(\text{pyz})_{1.5}(4\text{-HOpy})_2](\text{ClO}_4)_2$. Analysis of the pyrazine-related vibrational modes provides a superb local probe of magnetoelastic effects because this ligand functions as the primary exchange pathway and is present in both systems. Variable temperature and high pressure spectroscopy reveal improved hydrogen bonding in the PF_6^- complex due to the natural tendency for two-dimensional layers to compress. These effects are less apparent in the ClO_4^- system because the important distortions are intra- rather than inter-ladder in na-

ture. Applied field drives $[\text{Cu}(\text{pyz})_2(2\text{-HOpy})_2](\text{PF}_6)_2$ through a magnetic quantum phase transition at $B_C = 19$ T that involves several different pyrazine-related vibrations. In contrast, only one mode – the out-of-plane pyrazine distortion – is active in $[\text{Cu}(\text{pyz})_{1.5}(4\text{-HOpy})_2](\text{ClO}_4)_2$. This is because Cu dimers (which tend to develop at low temperature) are less reliant on a series of local lattice distortions rather than a single displacement to facilitate the development of the fully saturated state. These findings – together with similar magneto-infrared work on other copper complexes – are key to developing an unusual set of structure-property relations involving both magnetic dimensionality and spin-lattice interactions. While zero-dimensional (or “dot-like”) systems connected only by intermolecular hydrogen bonds display no spin-lattice coupling across this type of field-driven transition, coupling increases in the one-dimensional case, reaches a maximum in the ladder, and falls again in layered analogs. The availability of the intermediate dimensionality system, $[\text{Cu}(\text{pyz})_{1.5}(4\text{-HOpy})_2](\text{ClO}_4)_2$, is crucial to unveiling this trend.

Through our prior work on $[(\text{CH}_3)_2\text{NH}_2]M(\text{HCOO})_3$ ($M=\text{Mn}^{2+}, \text{Co}^{2+}, \text{Ni}^{2+}$) and the copper-containing quantum magnets, we have shown that hydrogen- and halogen-bonding interactions, although inherently weak, can mediate magnetic exchange, introduce frustration, and drive magnetic quantum phase transitions. In order to uncover the high magnetic field coupling mechanism of P and B in $(\text{NH}_4)_2[\text{FeCl}_5 \cdot (\text{H}_2\text{O})]$ and to explore the structural distortions that this system undergoes through the various magnetic phases and across the magnetic quantum phase transition, we bring together pulsed-field polarization techniques, magneto-infrared spectroscopy, and lattice dynamics calculations. We show that high-field polarization is quenched by the quasicollinear \rightarrow collinear sinusoidal magnetic transition. Remarkably, spin-lattice coupling across the magnetic quantum phase transition reveals that nearly all low-frequency displacement patterns modulate magnetic exchange – notably, they do

so by altering hydrogen- and halogen-bonding interactions. This is entirely different than other molecular multiferroics, where only one or two modes are magneto-active. An analysis of bulk vs microscopic techniques reveals that magneto-infrared measurements are sensitive to both spin-phonon and electron-phonon coupling. Because $(\text{NH}_4)_2[\text{FeCl}_5 \cdot (\text{H}_2\text{O})]$ breaks time reversal, rotational, mirror plane, and inversion symmetry, this work opens the door to the exploration of other molecular multiferroics in order to uncover exotic coupling phenomena that may exist between spin, charge, and lattice degrees of freedom.

The remainder of the dissertation is organized as follows: Chapter 2 presents a literature survey covering topics such as the complex magnetic phenomena that arise in molecule-based materials and how they manifest in complex systems. Chapter 3 describes the fundamentals of spectroscopy, important measurement techniques, and sample preparation. Chapter 4 is devoted to our study of the ferroelectric and magnetic ferroicities in $[(\text{CH}_3)_2\text{NH}_2]\text{Mn}(\text{HCOO})_3$. Chapter 5 details the structure-property relations in the $[(\text{CH}_3)_2\text{NH}_2]M(\text{HCOO})_3$ ($M=\text{Mn}, \text{Co}, \text{Ni}$) family of multiferroics. Chapter 6 presents our magneto-infrared, temperature, and high pressure investigation of two copper-containing coordination polymers towards understanding spin-phonon coupling across a broader family. Chapter 7 discusses pulsed-field polarization and magneto-infrared techniques on $(\text{NH}_4)_2[\text{FeCl}_5 \cdot (\text{H}_2\text{O})]$, unveiling the coupling mechanisms between charge, structure, and magnetism. Finally, Chapter 8 summarizes my work.

Chapter 2

Literature survey

2.1 Multifunctional and multiferroic materials

Multifunctional materials integrate nearly independent properties into a single system that can be accessed and controlled simultaneously. [43] These properties, especially as they relate to condensed matter science, include but are not limited to tunable electronic bands, magnetic interactions, and lattice distortions. [44] The coupling of charge, spin and lattice degrees of freedom allows additional features to emerge due to interactions between these degrees of freedom. Some prominent examples include multiferroics, shape memory polymers, and magnetic and electronic sensors for data storage. [45–47] These materials often display associated properties such as electrical conductivity, interesting optical responses, and colossal magnetoresistance. [48, 49]

2.1.1 Multiferroic materials

One important example of a multifunctional material is a multiferroic. Multiferroic materials are defined as having at least two of the ferroic orders in the same phase,

with these orders being ferroelectricity, ferromagnetism, ferroelasticity, and ferrotoroidicity. [50, 51] The definition of multiferroics, however, turns out to be rather flexible. The implications of ferrotoroidicity in multiferroics are not extensively studied due to the lack of physical materials to study and the difficulty in accessing the phase, and therefore this order is often left out of the general definition. [52] Additionally, other types of order like antiferromagnetism and ferrimagnetism are now included. [47, 53] A magnetoelectric multiferroic focuses on the former two orders (ferroelectricity and ferromagnetism) because of important applications in low-powered data storage and the development of magnetoelectrics. [54]

What makes multiferroics unique is the prospect of phase control by other tuning parameters. [55] Usually, applied electric field E (magnetic field H , stress σ) can tune the polarization (magnetization M , strain ε). However, multiferroics are powerful in that these properties can be driven by their non-conjugate tuning parameters. Figure 2.1 presents a schematic of multiferroic control with respect to time-reversal and space-inversion symmetries. [52]

Two types of multiferroics exist. Type-I multiferroics describe systems where the ferroelectricity and magnetism arise due to different sources. Here, the electronic and magnetic transitions are generally far apart, with the magnetic transition occurring at much lower temperatures. This phenomenon is more common, but the coupling between the two ferroic orders is inherently weaker. [53] Prominent examples of this type include $[(\text{CH}_3)_2\text{NH}_2]\text{Mn}(\text{HCOO})_3$, BiFeO_3 , and BiMnO_3 [56–59]. Alternatively, in type-II multiferroics, ferroelectricity and magnetism stem from the same source, making the coupling between the two rather large. [60] Generally, the development of a magnetically ordered state strongly enhances the ferroelectric response. TbMnO_3 is a prominent example of a type-II multiferroic due to the presence of multiple magnetic ordering transitions and a nonzero electric polarization that accompanies

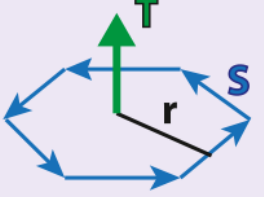
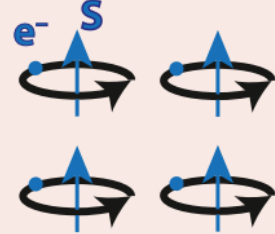
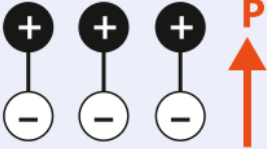
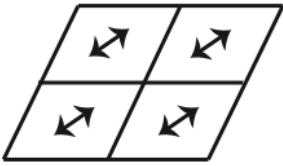
| <div style="text-align: center;">SPACE</div> <div style="text-align: right;">TIME</div> | CHANGE | INVARIANT |
|---|--|--|
| CHANGE | a.) Ferrotoroidic  | b.) Ferromagnetic  |
| INVARIANT | c.) Ferroelectric  | d.) Ferroelastic  |

Figure 2.1: Schematic of multiferroic control. Ferrotoroidicity, ferromagnetism, ferroelectricity, and ferroelasticity are depicted with respect to time-reversal and space-inversion symmetries. [52]

the lowest. Other examples include $\text{Ni}_3\text{V}_2\text{O}_6$, MnWO_4 , and $(\text{NH}_4)_2[\text{FeCl}_5 \cdot (\text{H}_2\text{O})]$. [53,61]

A primary challenge in the field lies in identifying magnetoelectric materials. Ferroelectricity and magnetism are typically mutually exclusive because of their requirements for d orbitals. Ferroelectricity requires d orbitals to be empty which creates a lattice distortion. For example, in a perfectly cubic perovskite oxide ABO_3 configuration, the $2p$ highest occupied molecular orbitals (t_{1u} , t_{2u} , t_{1g}) on oxygen and the $3d$ transition metal lowest unoccupied molecular orbital (t_{2g}) are orthogonal and therefore do not participate in metal-oxygen bonding. The primary bonding forces are inner σ orbitals and ionic interactions. [62] Upon a space group change, the metal ion becomes displaced within the octahedron and the cubic symmetry is lowered (Fig. 2.2). This allows the orbitals to overlap, and the asymmetry creates a spontaneous dipole moment. A typical perovskite oxide ferroelectric material possesses formal charges corresponding to d^0 electron configurations on the metal ion. When the d orbital becomes partially occupied, the tendency for the material to

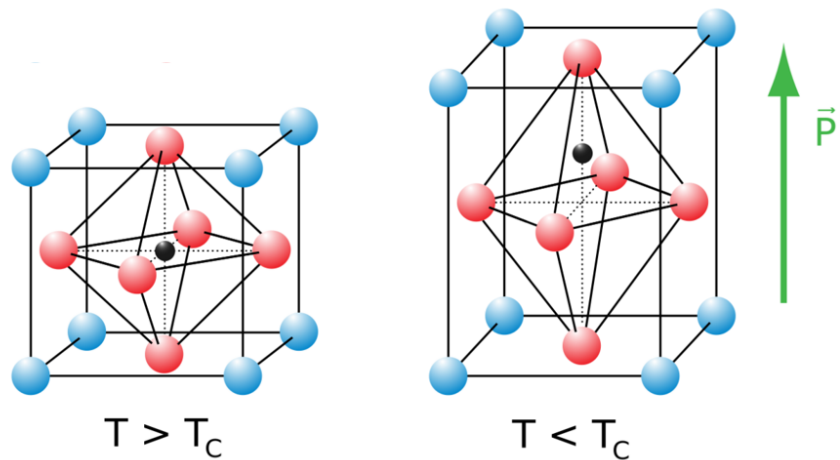


Figure 2.2: Schematic of a perovskite oxide above and below the ferroelectric transition. Applied electric field shifts the central atom to an off-center position, inducing ferroelectricity.

undergo a ferroelectric transition is eliminated. [63] This can be explained with a number of effects including the size of the metal ion, the tendency for the material to undergo a more dominant transition, electronic properties, magnetic properties, or some combination of these. [64] On the other hand, ferromagnetism requires partially filled d orbitals to induce a magnetic moment. Transition metal centers are obvious choices for substitution. Thus, the two properties are counter indicative. This is why unique and clear approaches have to be used.

2.1.2 Molecular multiferroics vs oxide multiferroics

Molecule-based materials offer a unique opportunity to explore the properties of multiferroics at achievable experimental fields. They differ from typical oxide multiferroics, which are rigid and high-energy in nature. What makes molecule-based analogs attractive is that they sport similar interactions, soft lattices and flexible architectures, and experimentally-realizable critical fields - although as a group, they are vastly under-explored compared to their oxide counterparts. [55, 65–69] These molecular complexes also differ with respect to conventional magnets, as they can be synthesized in a variety of structures and dimensions and introduce new phenomena and mechanisms as well as the combination of properties not observed in commercial magnets. The well-established hosting behavior of molecule-based materials aids in the development of ferroelectric properties. [1] By introducing building blocks and counterions with well-known polar characteristics, the material easily adopts similar properties. For example, in many hybrid organic-inorganic perovskites, order-disorder transitions of counterions can drive ferroelectricity. [70–72] Because these materials are relatively soft, counterion ordering via hydrogen bonding distorts the framework and displaces the metal ion within the oxygen octahedra, inducing ferroelectricity. In this dissertation, we investigate the microscopic response of a molecule-

based multiferroic through the order-disorder ferroelectric transition.

The first organic ferromagnet $[\text{Fe}^{\text{III}}(\text{C}_5\text{Me}_5)_2]^+[\text{TCNE}]^-$ (Me=methyl, TCNE=tetracyanoethylene) – although it was ionic, zero-dimensional, and organic-solvent soluble in nature – magnetically ordered despite large through-space separations between the spin sites. [73] Naturally, this led to the search for molecule-based systems with unique magnetic, electronic, and structural properties. One of the first examples, a porous molecular crystal $[\text{Mn}_3(\text{HCOO})_6](\text{C}_2\text{H}_5\text{OH})$, was simultaneously ferroelectric and ferrimagnetic below 8.5 K. [1, 74, 75] The discovery that these systems could host inherent multiferroic properties propelled worldwide interest and spearheaded the development of new phenomena, synthetic strategies, and materials. [1, 76] Some of the overarching material categories include organic-inorganic hybrids, organic magnets, molecular magnets, and nanoscale materials. At the current state, the list of multiferroic molecular systems is quite extensive, and includes nearly every transition metal/organic ligand/dimensionality combination. [50, 77–79] Interestingly, the list of materials includes both type-I and type-II multiferroics, providing a low energy scale comparison to traditional oxides.

The most intriguing aspect of molecule-based multiferroics is that intermolecular interactions can control the inherent properties of the system, including ordering temperatures, the low temperature ground state, and frustration/broken symmetry. Moreover, these systems can be fine-tuned to reveal specific properties by substituting different ligands (and thereby altering the superexchange pathway), introducing and modifying hydrogen bonding lengths, and varying both the metal center and counterion. This flexibility makes these systems much more versatile than conventional magnetic materials. In this dissertation, we highlight two families of organic multiferroics: a hybrid organic-inorganic complex $[(\text{CH}_3)_2\text{NH}_2]M(\text{HCOO})_3$ ($M=\text{Mn}, \text{Co}, \text{Ni}$) and a completely molecular system $(\text{NH}_4)_2[\text{FeCl}_5 \cdot (\text{H}_2\text{O})]$. The latter has strong sim-

ilarities to the lead perovskite halides.

2.1.3 Magnetoelastic coupling

The interplay of structure and magnetism in magnetic materials leads to unique functionalities and phenomena. Magnetoelastic coupling describes a phenomenon where a change of the magnetic state of a system induces a change of the crystal lattice (volume, size). This effect can be understood through the cross coupling of stress and magnetic field – applied magnetic field H induces strain effects ε , or applied strain σ changes the magnetic state M . These relations are known as the magnetostrictive effect and the magnetomechanical effect, respectively. Table 2.1 summarizes some of the important magnetoelastic effects along with their corresponding inverse effects.

Magnetostriction is an intrinsic property of a material related to magnetoelastic coupling. When a system is magnetized, the shape of the magnet is affected. Stress and magnetic field are related according to Le Chatelier’s principle via:

$$\left(\frac{d\gamma}{dH}\right)_\sigma = \left(\frac{dB}{d\sigma}\right)_H \quad (2.1)$$

where γ is the saturation magnetostriction under a given mechanical stress σ and

Table 2.1: Summary of important direct and corresponding inverse magnetoelastic effects.

| Direct effects | Indirect effects |
|---|---|
| <i>Magnetostrictive effect</i> | <i>Magnetomechanical effect</i> |
| Applied magnetic field changes physical dimension of a ferromagnetic material | Applied mechanical stress alters the magnetic state of a ferromagnetic material |
| <i>Magnetovolume effect</i> | <i>Nagaoka-Honda effect</i> |
| Magnetization drives a volume change near T_C | Change in volume affects magnetic state |

B is the flux density for a magnetizing field H . Therefore, when the product $\sigma\gamma$ is positive, the flux density increases with stress; when $\sigma\gamma$ is negative, B decreases under stress. A system ultimately undergoes a magnetoelastic deformation in order to reach the most energetically favorable state. For example, it may be energetically favorable for a cubic crystal to deform slightly under magnetic field – this increase in anisotropy decreases the cost in elastic energy.

Spectroscopy is a highly sensitive technique that enables the investigation of coupling phenomena between multiple degrees of freedom. One of the most important examples is the coupling between spin and lattice degrees of freedom, a relationship known as spin-lattice coupling. Spectroscopy under magnetic field offers a unique opportunity to study microscopic changes in the lattice as a function of magnetic field. In this way, small distortions within specific bond lengths and angles can be tracked with field to reveal the microscopic mechanisms that materials undergo to magnetically saturate and to correlate to specific displacement patterns. If field-induced frequency shifts are large, spin-phonon coupling constants can be extracted across the magnetic transition via:

$$\omega = \omega_0 + \lambda \langle S_i \cdot S_j \rangle \quad (2.2)$$

where ω and ω_0 are the unperturbed and perturbed phonon frequencies, $\langle S_i \cdot S_j \rangle$ is the nearest-neighbor spin-spin correlation function, and λ is the mode-dependent spin-phonon coupling constant. [20,80,81] The value of λ provides insight into the strength between the lattice and the spin. Small values of lambda indicate that a specific distortion is not very sensitive to the transition – this is the case in materials like CrSiTe_3 and $[(\text{CH}_3)_2\text{NH}_2]\text{Mn}(\text{HCOO})_3$. [82, 83] Examples of spin-phonon coupling can also be seen in materials like $\text{Mn}[\text{N}(\text{CN})_2]_2$ [29] or $[\text{Cu}(\text{pyz})_2(\text{HF}_2)]\text{PF}_6$ [84], as well as a large portion of this dissertation.

2.2 Magnetism and magnetically-driven phase transitions

Magnetically-ordered (collective) states are of particular interest to the systems in this dissertation. There are several different conformations in which spins can align in a material. Figure 2.3 describes the important cases. Paramagnetism (PM) describes electrons that are randomly oriented but under applied field can become aligned. This is often the configuration of metal-containing materials at room temperature. Ferromagnetism (FM) is a phenomenon in which all spins are aligned within a material to produce a bulk magnetization. In contrast, antiferromagnetism (AFM) describes a material in which the spins are anti-parallel in a uniform fashion so that there is a net magnetization of zero. Ferrimagnetism (FiM) differs from AFM in that the anti-parallel spins are uneven, opposing moments, leading to a small net magnetization. Non-collinear antiferromagnetism (NC-AFM) describes a complex magnetic structure such as a spiral, cycloid, or canted antiferromagnet. [64] Systems with transition metals are often included in this category because they have competing antiferromagnetic and ferromagnetic interatomic exchange interactions.

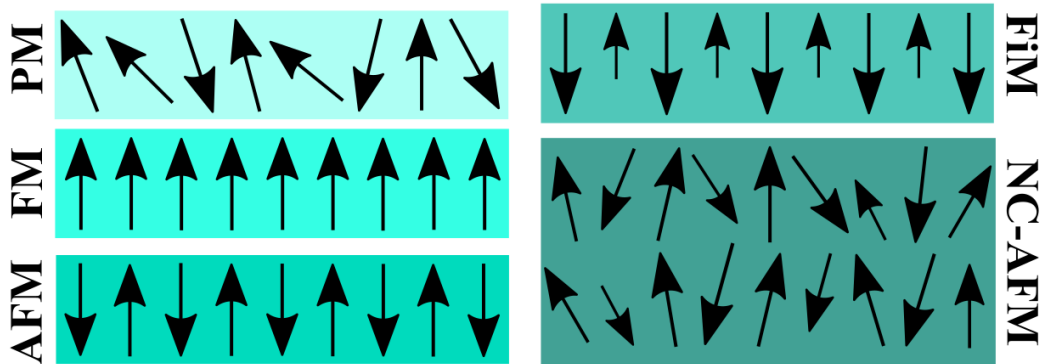


Figure 2.3: Ordering of spins in magnetic materials. PM represents paramagnetism, FM represents a material in the ferromagnetic state, AFM stands for antiferromagnetism, FiM symbolizes ferrimagnetism, and NC-AFM stands for non-collinear antiferromagnetism like cycloidal, spiral, or canted antiferromagnets.

Long-range-ordered magnetic states occur because of exchange interactions between magnetic moments. Exchange interactions are electrostatic – charges of the same sign repel when they are in close proximity. However, the overall wave function must be antisymmetric for electrons, meaning that the spin component of the wave function must either be the antisymmetric singlet state χ_S where $S=0$ or the symmetric triplet state χ_T where $S=1$. We consider a simple two-electron model. The wave functions for the singlet Ψ_S and triplet case Ψ_T are written as:

$$\Psi_S = \frac{1}{\sqrt{2}}[\psi_a(r_1)\psi_b(r_2) + \psi_a(r_2)\psi_b(r_1)]\chi_S \quad (2.3)$$

$$\Psi_T = \frac{1}{\sqrt{2}}[\psi_a(r_1)\psi_b(r_2) - \psi_a(r_2)\psi_b(r_1)]\chi_T \quad (2.4)$$

where $\psi(r_1)$ and $\psi(r_2)$ represent the states of the first and second electrons. The energies of these two possible states are then:

$$E_S = \int \Psi_S^* \hat{H} \Psi_S dr_1 dr_2 \quad (2.5)$$

$$E_T = \int \Psi_T^* \hat{H} \Psi_T dr_1 dr_2. \quad (2.6)$$

The difference between these states is parameterized as:

$$J = \frac{E_S - E_T}{2} = \int \psi_a^*(r_1)\psi_b^*(r_2)\hat{H}\psi_a(r_2)\psi_b(r_1)dr_1dr_2 \quad (2.7)$$

in order to extract the exchange constant J . Therefore, the spin-dependent term is written as:

$$\hat{H}^{spin} = -2JS_1 \cdot S_2. \quad (2.8)$$

Of course, this is a simplified approach as we are only looking at a two-electron model. Nevertheless, in an extending solid, interactions between all neighboring atoms should behave similarly, which leads to the Hamiltonian of the Heisenberg model:

$$\hat{H} = -2 \sum_{i>j} J_{ij} S_i \cdot S_j \quad (2.9)$$

where J_{ij} is the exchange constant between the i^{th} and j^{th} spins. When $J > 0$, the energy of the singlet state is larger than that of the triplet state and the triplet $S=1$ state is energetically favored. Alternatively, if $J < 0$, the singlet $S=0$ state is favored.

2.2.1 Exchange pathways

Two main types of exchange interactions exist in solids – direct and indirect exchange. Direct exchange occurs when the electrons on neighboring magnetic atoms interact directly, in which case there is no need for an intermediary. Figure 2.4 displays two possible direct exchange configurations that can exist between metal centers in octahedral environments – the metal centers in the first and second cases share a

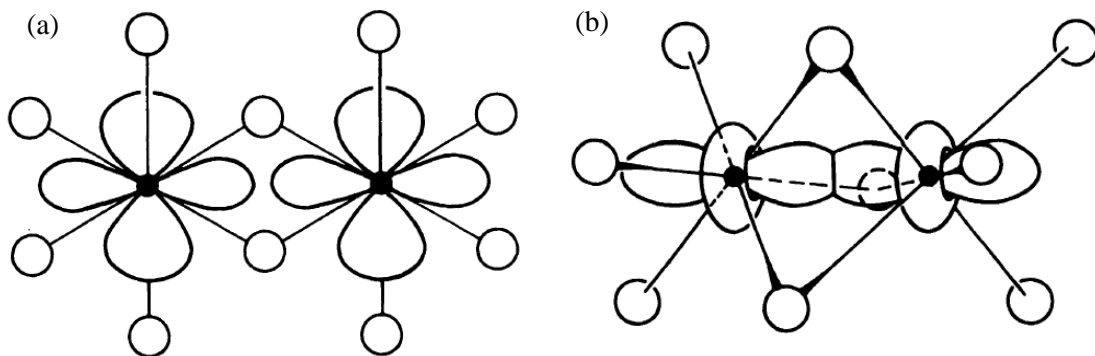


Figure 2.4: Symmetry relations for overlapping orbitals in octahedral environments that share either (a) a common edge or (b) a common face. These conformations display direct exchange interactions, as there is no need for an intermediary. [85]

common edge or face, respectively. However, direct exchange is not often possible, or at least not the dominant exchange pathway in systems. This is because there is a lack of direct overlap between neighboring magnetic orbitals in a real system. This is the case in materials like rare earth oxides, where the $4f$ electrons are strongly localized and therefore lie close to the nucleus, providing little electron density to interact with neighboring ion atoms. Moreover, it is difficult to control magnetic properties because the superexchange angle is extremely sensitive to external stimuli.

Therefore, it is more often the case that magnetic materials exhibit indirect exchange interactions. There are several different mechanisms of indirect exchange including superexchange (short-range, ferromagnetic, antiferromagnetic), Ruderman-Kittel-Kasuya-Yosida RKKY coupling (long range, oscillating sign), and double exchange (mixed valency). [64] Here, we focus our discussion on superexchange mechanisms because of the ability to control magnetic properties in solids due to the introduction of chemical tunability and flexibility. It is important to note that solids may have both direct and indirect interactions, but the indirect mechanisms are usually larger.

Indirect exchange interactions occur via a superexchange pathway, where a non-magnetic ion mediates two non-neighboring magnetic ions. The most fundamental and simple superexchange pathway is that of two metals and an oxygen $M-O-M$. These pathways arise because there is a kinetic energy advantage for the antiferromagnetic state. Considering a system with one unpaired electron on each magnetic center, the ground state is antiferromagnetic. These electrons can delocalize to develop excited states that are still antiferromagnetic in nature. Conversely, the ferromagnetic state only has one possible ground state due to the Pauli Exclusion Principle.

The fact that this interaction involves metal and oxygen orbitals makes it a

second order process derived from second-order perturbation theory. [64] Therefore, the energy involved in this interaction is proportional to the square of the matrix element over the energy required to develop the excited state. Hence,

$$J \sim -\frac{t^2}{U} \quad (2.10)$$

where t is the hopping integral and U is Coulomb energy. [64] This “hopping” is what leads to the stabilization of the singlet state over the triplet state.

2.2.2 Goodenough-Kanamori-Anderson rules

The hopping integral t is actually consistent of two parts. The first is a potential energy contribution in the form of electron repulsion. This part favors the ferromagnetic state, but it is usually quite small. The other part is the kinetic energy contribution, which is dependent upon the degree of overlap of the orbitals within the superexchange pathway. [64] The sign and the value of the superexchange depends on the metal-oxygen-metal angle and which d orbitals are involved in the exchange interaction.

The Goodenough-Kanamori rules – first postulated by Goodenough in 1955 [86] and later confirmed and expanded on by Kanamori in 1959 [87] – provide a semi-empirical guideline for determining if a cation-cation (direct) or cation-anion-cation (indirect) superexchange will be ferromagnetic or antiferromagnetic in nature. In 1959, Anderson [88] provided a more theoretical explanation for how electrons align in superexchange pathways. There are guidelines for both 180° and 90° cation-anion-cation interactions, but we focus primarily on the 180° interactions as they pertain to the materials in this dissertation. For an exchange interaction to be antiferromagnetic, two ions must have lobes of magnetic orbitals pointing toward each other in such a way that the orbitals would have a reasonable overlap integral. Figure

2.5 (left) displays two examples of antiferromagnetic superexchange. An example of strong exchange is given as the overlap of a $d_{x^2-y^2}$ of one metal center through a $p\sigma$ orbital to a $d_{x^2-y^2}$ of the second metal center. Weaker antiferromagnetic exchanges can occur as well ($d_{yz}-p\pi-d_{yz}$). Is it clear, even from a visual examination, that the overlap integral is clearly much smaller in the latter. Conversely, a ferromagnetic superexchange requires that orbitals are arranged in such a way that they are expected to be in contact but to have no overlap integral. This is likely the case between exchanges of different metal d orbitals ($d_{x^2-y^2}-p\sigma-d_{z^2}$) or interactions that occur via a 90° exchange.

Later, a more detailed mathematical solution for the total antiferromagnetic interaction J_{tot} was determined, which builds off of the principles of Eqn. 2.10. It was found that J_{tot} is the sum of both the effective antiferromagnetic Heisenberg exchange J (oxygen $p \rightarrow$ metal d interaction) and the energy of an intermediate state when there are two holes on the same oxygen p orbital J' (metal $d \rightarrow$ metal

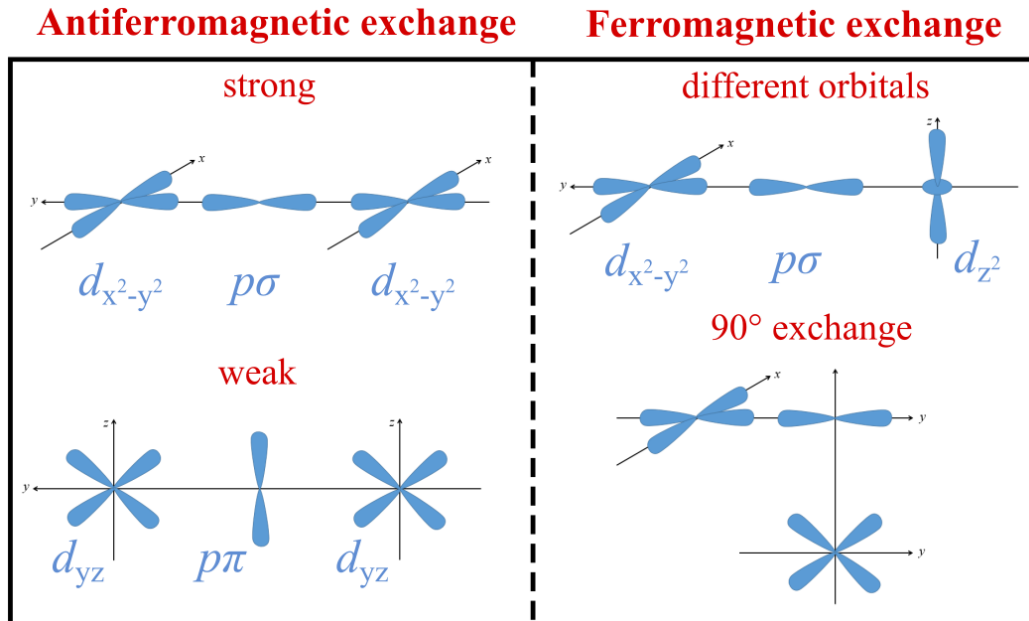


Figure 2.5: Summary of the semi-empirical Goodenough-Kanamori rules. Both antiferromagnetic and ferromagnetic superexchange pathways are depicted. [85]

d interaction). Hence, $J_{\text{tot}} = J + J'$ – these energies are represented by Fig 2.6 (a) and (b), respectively. The antiferromagnetic Heisenberg exchange J is given as:

$$J = \frac{2t_{pd}^4}{\Delta^2 U_{dd}} \quad (2.11)$$

where t_{pd} are possible hopping integrals from metal d to oxygen p orbitals and then on to the second metal d orbital, Δ is the charge transfer energy, and U_{dd} is the energy of the intermediate state (when the electrons are in the $\bar{\varepsilon}_p$ state). These pathways are numbered in Fig. 2.6 (a). Alternatively, J' is given as:

$$J' = \frac{4t_{pd}^4}{\Delta^2(2\Delta + U_{pp})} \quad (2.12)$$

where the factor of 4 comes from the fact that twice as many routes exist in Fig. 2.6 (b) than in (a) – the sequence of electron hops can be interchanged from sites i and j to the oxygen atoms. The energy here is $2\Delta + U_{pp}$ because it takes into account charge transfer as well as Coulomb repulsion. Therefore, the total expanded antiferromagnetic interaction is given as:

$$J_{\text{tot}} = 2t_{dd}^2 \left(\frac{1}{U_{dd}} + \frac{1}{\Delta + U_{pp/2}} \right). \quad (2.13)$$

This is the case for a 180° exchange interaction. The equation for the 90° case is obviously different. For more information on this subject, see reference [89].

2.3 Hydrogen and halogen bonding

Hydrogen bonds also provide effective routes to induce ferroelectricity and mediate magnetic exchange in molecule-based magnets. These interactions play a pivotal role in assembly mechanisms, superconductivity, and exchange due to their long-range

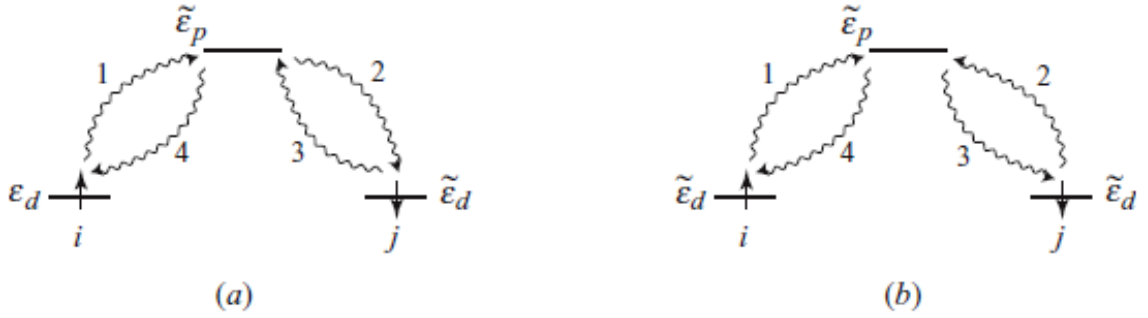


Figure 2.6: (a) Two neighboring d sites with an oxygen ion in between. The wavy lines represent virtual hoppings of a d hole from one site to the other via p levels. The numbers give one possible sequence of consecutive hoppings. This energy corresponds to J . (b) Another sequence of hoppings that transfers a d hole from each metal to the p , so that there are two holes at the same oxygen. This energy corresponds to J' . [89]

flexibility. [36] Recently, hydrogen-bonded systems have been emerging as alternative routes to covalently-bonded magnetic materials. These types of systems are often organic-based molecular magnets and are generally much more versatile than conventional magnetic materials – they have lower energy scales and flexible architectures which allow exotic quantum phenomena like complex magnetic structure to emerge at realizable fields. [90] The emergence of materials with hydrogen bonding or π - π stacking of aromatic rings plays an important role in coordination compounds with unique magnetic properties. [91]

Hydrogen bonds contribute to both electronic and magnetic transitions. In many molecule-based multiferroics – like the $[(\text{CH}_3)_2\text{NH}_2]M(\text{HCOO}_3)$ ($M=\text{Mn}, \text{Ni}, \text{Co}$) family and $(\text{NH}_4)_2[\text{FeCl}_5 \cdot (\text{H}_2\text{O})]$ discussed in this dissertation – a decrease in temperature allows hydrogen bonds to develop through an order-disorder transition. In $[(\text{CH}_3)_2\text{NH}_2]\text{Mn}(\text{HCOO}_3)$ at room temperature, an ammonium counterion rotates along a three-fold axis. Below the order-disorder transition, hydrogen bonding interactions develop between the counterion and the cage, distorting the metal-oxygen

octahedra and inducing ferroelectricity. [56] This is similar to the transition in molecular $\text{HHTP}\cdot 4\text{H}_2\text{O}$ (HHTP = hexahydroxytriphenylene). [35]

However, what makes these interactions unique is the prospect of mediating magnetic exchange. Figure 2.7 summarizes the hydrogen bonding interactions in several molecular materials and how they enable magnetic exchange. Some important examples include the family of V_{12} molecular magnets, [94] $[\text{Cu}(\text{IDA})(\text{ImP})]_n$ (H_2IDA = iminodiacetic acid and ImP = imidazo[1-a]-pyridine), [92] and $\text{VOHPO}_4 \cdot \frac{1}{2}\text{H}_2\text{O}$. [93] Hydrogen bonds, in general, strengthen as a function of decreasing temperature. This is because these interactions overtake thermal fluctuations as materials relax into their ground state. These interactions can increase the magnetic lattice dimensionality, as is the case for the well-known single molecular magnet $\text{Mn}^{II}[\text{Mn}^{II}(\text{MeOH})_3]_8(\mu\text{-CN})_{30}[\text{Mo}^{\text{V}}(\text{CN})_3]_6\cdot 5\text{MeOH}\cdot 2\text{H}_2\text{O}$ [11]. A rare case arises in the molecule-based magnet $(\text{NH}_4)_2[\text{FeCl}_5(\text{H}_2\text{O})]$, where hydrogen bonding inter-

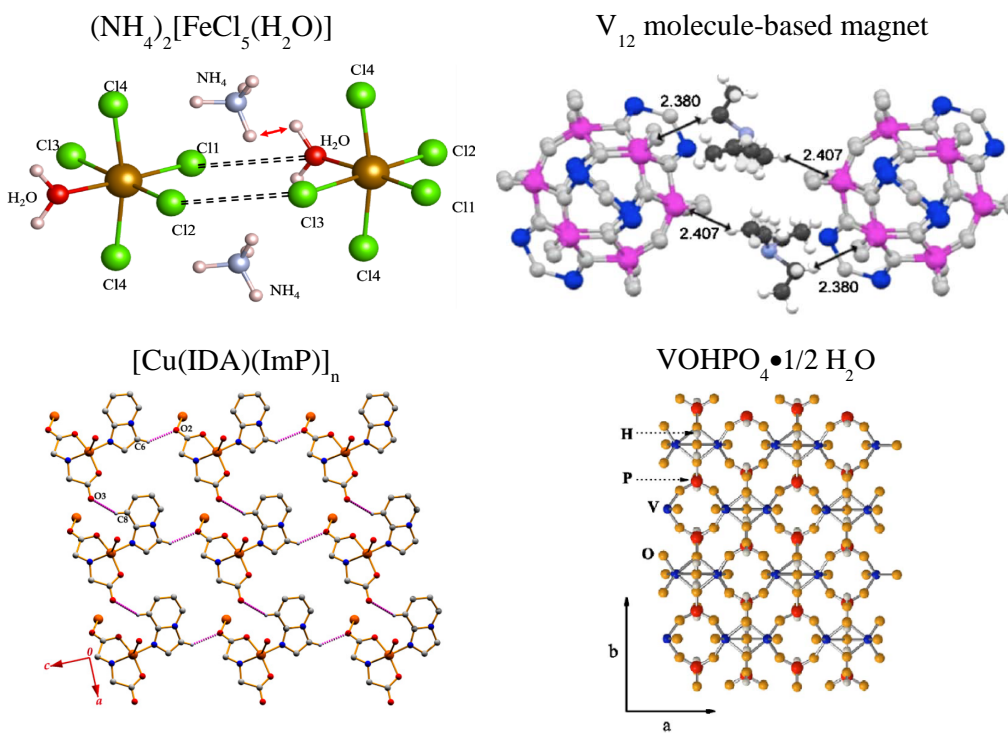


Figure 2.7: Summary of hydrogen bonded molecular magnetic materials. [90, 92–94]

actions hold the system together and mediate magnetic exchange. [61] One of the important magnetic exchange interactions is shown in Fig. 2.7 (a) - this system is discussed in detail later in Chapter 7.

Intermolecular halogen \cdots halogen bonds also play an important role in the functionality of molecule-based materials. [95] These bonds are characterized by a distance shorter than the sum of the van der Waals radii [96] and, as with hydrogen-bonding interactions, introduce chemical flexibility and overall low energy scales. [97] Importantly, they are also capable of mediating magnetic exchange in materials such as the the series of halogen-substituted pyridine compounds 5-iodo-2-aminopyridine, $\text{CuX}_2(\text{pyrazine-N,N}'\text{-dioxide})(\text{H}_2\text{O})_2$ ($\text{X}=\text{Cl},\text{Br}$) and $(\text{NH}_4)_2[\text{FeCl}_5\cdot(\text{H}_2\text{O})]$. [61, 95, 98] In this work, we focus primarily on $\text{Cl}\cdots\text{Cl}$ interactions in a molecular multiferroic.

2.4 Classical versus quantum phase transitions

The past twenty years have seen an insurgence of interest in the unique properties that arise in quantum matter. [21] This is largely due to the discovery that perovskites – namely $\text{YBa}_2\text{Cu}_3\text{O}_7$ – exhibit exotic properties like high-temperature superconductivity. [99] In a broad sense, the aim of studying quantum matter is to understand and describe the interaction of particles at sufficiently low temperatures so that quantum mechanics, rather than temperature-dependent properties, emerge. [24] In these states, exotic magnetic and electronic phases can be driven with external parameters other than temperature. The effects of thermal broadening are thus eliminated.

Classical phase transitions are those that are driven by temperature. Energy scales are determined by $k_B T$, and above the transition temperature, these energies destroy any order in the system. Typical classical transitions include liquid-solid

phase transitions or paramagnet-ferromagnet phase transitions. In both of these cases, temperature drives the material through the generally sharp transition – it is sharp since a particular symmetry operator either exists or does not. However, gradual second-order transitions exist in certain types of systems. [100–102] Below the transition temperature, the behavior of systems can be described with Bloch’s Law according to:

$$M(T) = M_0[1 - (T/T_C)]^{3/2} \quad (2.14)$$

where M_0 is the spontaneous magnetization at 0 K and T_C is the Curie temperature. However, near T_C , the critical exponent is not necessarily 3/2. The relationships changes to:

$$\chi \propto (T - T_C)^{-\gamma}; T > T_C \quad (2.15)$$

$$M \propto (T_C - T)^\beta; T < T_C \quad (2.16)$$

$$M \propto H^{1/\delta}; T = T_C \quad (2.17)$$

where γ , β , and δ depend on the dimensionality of the system and describe the nature of the transition. [64] In a continuous phase transition, the critical exponent gives insight into the dimensionality of the system d , the dimensionality of the order parameter D , and whether the ordering forces in the system are short or long range in nature. [64] Table 2.2 summarizes the critical exponents for various models.

Because spectroscopy is a microscopic probe of the lattice, it is useful in tracking phase transitions as a function of temperature. This is because small temperature steps can be taken through the transition; sharp slope changes can be identified and analyzed by tracking the peak position of phonons versus temperature. Spectroscopy

Table 2.2: Critical exponents (β , γ , δ) for various models.

| Model | Mean-field | Ising | Ising | Heisenberg |
|----------|---------------|---------------|-----------|------------|
| D | any | 1 | 1 | 3 |
| d | any | 2 | 3 | 3 |
| β | $\frac{1}{2}$ | $\frac{1}{8}$ | 0.326 | 0.367 |
| γ | 1 | $\frac{7}{4}$ | 1.2376(6) | 1.388(3) |
| δ | 3 | 15 | 4.78 | 4.78 |

d =dimensionality of the system; D =dimensionality of the order parameter

also offers a unique opportunity in that it can identify which particular distortions contribute to the transition, unveiling the underlying mechanism of the development of properties such as magnetization and polarization.

On the other hand, quantum phase transitions occur (by definition) at zero temperature. They differ from classical phase transitions in that thermal fluctuations are absent, allowing quantum fluctuations – demanded by Heisenberg’s uncertainty principle – to become the dominant mechanisms. [24] These transitions are controlled by an external tuning parameter g rather than temperature. Near $g=g_c$ and at sufficiently low temperatures, emergent quantum properties like metal-insulator transitions [103] and superconductivity [104] arise. Figure 2.8 displays a general phase diagram near the vicinity of a quantum critical point with g and T . As discussed below, g can be any physical or chemical tuning parameter.

Quantum phase transitions have been uncovered in many systems including transition metal oxides, superconducting cuprates, and heavy fermion compounds, [105] and can be driven with a number of external stimuli. For example, in spin-ladder materials like $\text{Cu}(\text{DEP})\text{Br}_2$ or $\text{Cu}_2(\text{C}_5\text{H}_{12}\text{N}_2)_2\text{Cl}_4$, quantum phase transitions in the form a spin gap transition can be driven with applied magnetic field. [106, 107] Applied pressure drives a transition from a quasi-two-dimensional to a quasi-one-dimensional antiferromagnetic phase in the coordination polymer $\text{CuF}_2(\text{H}_2\text{O})_2(\text{pyrazine})$ at 9.1 kbar. [31] Additionally, chemical doping can drive these unique phases, as is the case

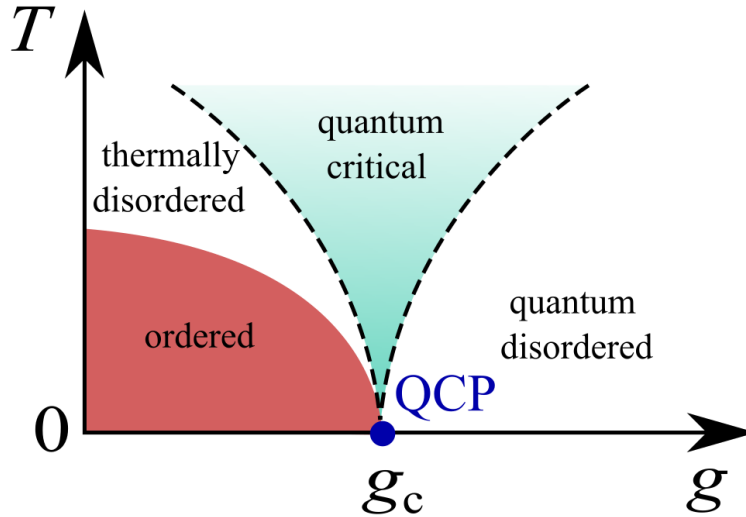


Figure 2.8: General phase diagram near the vicinity of a quantum critical point (labelled QCP) as a function of both a control parameter g and temperature T . When $r < 0$ and temperature is low, the material is in an ordered state. At $T=0$ K and $r=0$, the quantum critical point exists. Above this, the system becomes quantum disordered. [99]

in $\text{Pr}_{2-x}\text{Ce}_x\text{CuO}_{4-\delta}$. [108] Of course, $\text{YBa}_2\text{Cu}_3\text{O}_y$ is famous for its quantum critical behavior below the superconducting dome. These findings are summarized in Fig. 2.9. In this dissertation, we primarily focus on magnetic quantum phase transitions in molecule-based magnets and the lattice distortions that these systems undergo as they cross through the transition.

Magnetic quantum phase transitions, in which field drives exotic changes in the magnetic structure, are among the most well-studied types. In the quasi-one-dimensional quantum Heisenberg magnet $[\text{Cu}(\text{pyz})(\text{H}_2\text{O})(\text{gly})_2](\text{ClO}_4)_2$, the magnetic ground state is one of quantum disorder; applied field drives the system through a quantum phase transition to the fully saturated state at 13.3 T. [22] Alternatively, $[\text{Cu}(\text{pyz})(\text{gly})](\text{ClO}_4)$ undergoes two unique magnetic quantum phase transitions including the i) quantum-disordered paramagnet \rightarrow long-range ordered (LRO) state and the ii) LRO \rightarrow ferromagnetic state. [22] Although copper-containing materials are ideal candidates to investigate quantum effects due to the quantum $S=1/2$ na-

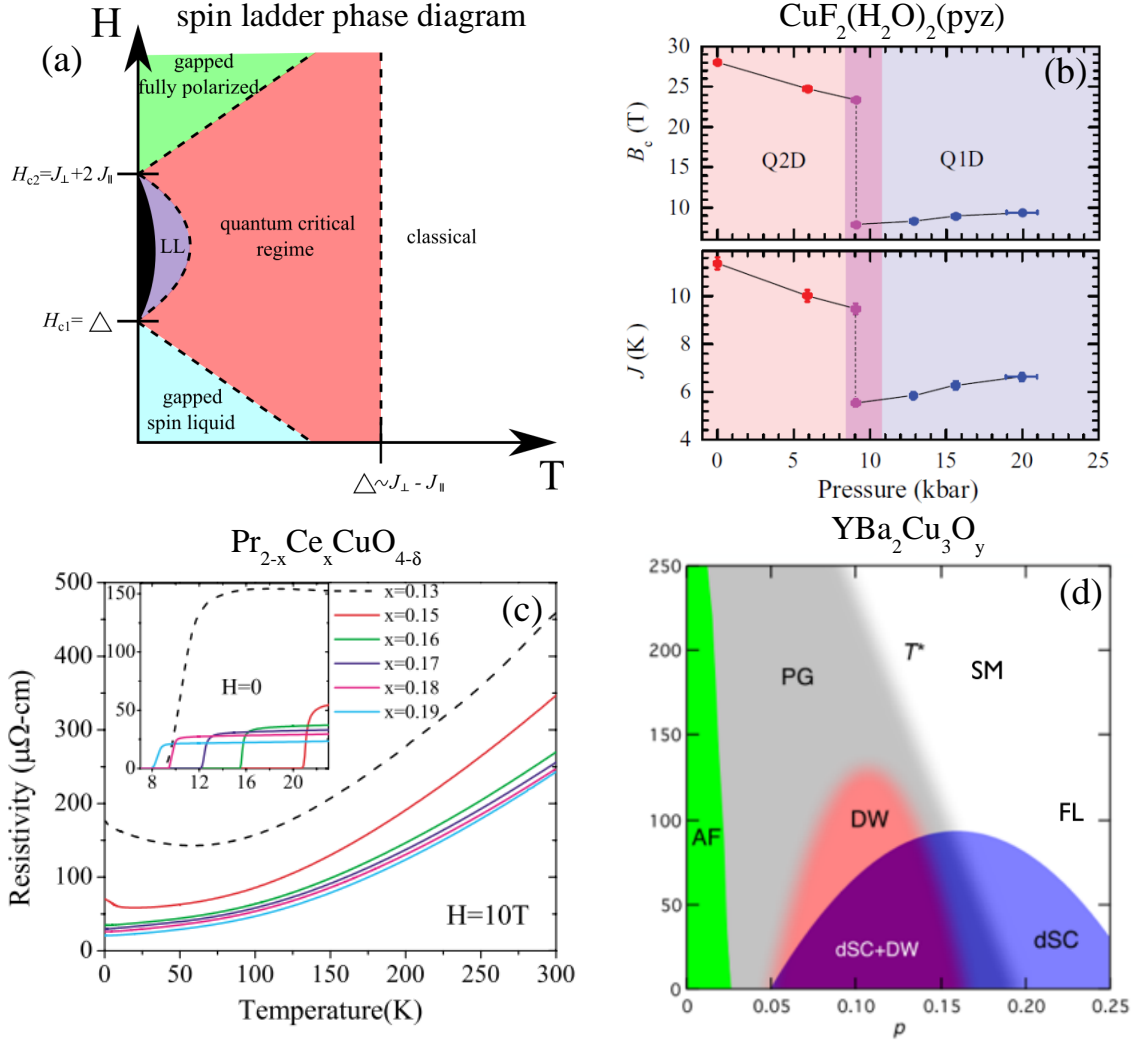


Figure 2.9: (a) General phase diagram for a spin ladder complex. H_{c1} and H_{c2} are the quantum critical points corresponding to the spin gap and the fully saturated magnetic state, respectively. [106] (b) Saturation field and J exchanges as a function of pressure, revealing a magnetic transition. (c) Resistivity versus temperature at various doping concentrations of $\text{Pr}_{2-x}\text{Ce}_x\text{CuO}_{4-\delta}$. [108] (d) Temperature-hole density phase diagram of $\text{YBa}_2\text{Cu}_3\text{O}_7$. [109]

ture of the spin, other metal-containing materials display magnetic quantum phase transitions, as is the case for $[\text{Ni}(\text{HF}_2)(\text{pyz})_2]\text{SbF}_6$. These materials are summarized in Fig. 2.10. [32]

2.4.1 Magnetic field drives magnetic quantum phase transitions

One important way to drive complex quantum phase transitions is through the application of magnetic field. This is because applied field can drive novel spin states and properties. Some of these properties include polarization and magnetoelectric coupling [28], band gap and color changes [110], and strain [111], although in this dissertation, we focus our attention on microscopic changes in the lattice like bond lengths and angles and what happens to them through phase transitions. What is interesting is that depending on the magnetic ground state of a system, various mag-

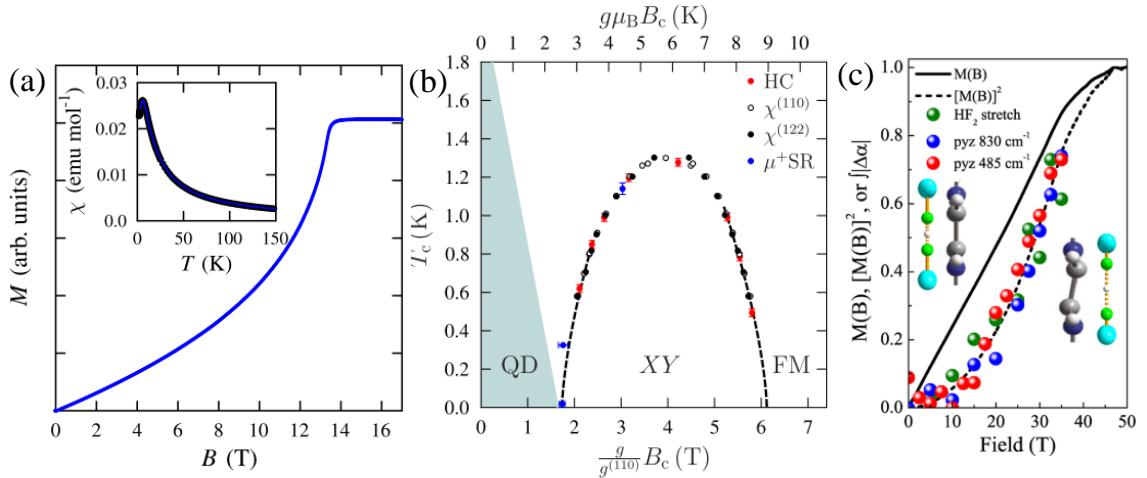


Figure 2.10: Summary of different magnetic quantum phase transitions in molecule-based materials including (a) magnetization saturation in $[\text{Cu}(\text{pyz})(\text{H}_2\text{O})(\text{gly})_2](\text{ClO}_4)_2$, (b) the B - T phase diagram of a quantum magnet $[\text{Cu}(\text{pyz})(\text{gly})](\text{ClO}_4)$ showing two quantum critical points, and (c) the microscopic mechanism that $[\text{Ni}(\text{HF}_2)(\text{pyz})_2]\text{SbF}_6$ undergoes to reach the quantum phase transition. [22, 32]

netic transitions can be driven. Nevertheless, under high enough magnetic field, all systems reach magnetic saturation in which their spins are fully aligned in the direction of the applied field – how materials reach this final state is, however, dependent upon both the direction of the applied field and the overall magnetic sublattice of the system.

Antiferromagnetic systems – which describe all of the molecular materials discussed in this dissertation – have a net magnetic moment of zero ($\uparrow\downarrow\uparrow\downarrow\uparrow$). If the applied field is parallel to the sublattice magnetization, a unique transition called a spin flop occurs. With low magnetic field, the moments are unaffected. At a critical field B_{SF} , the spins suddenly rotate and cant with magnetic field until they saturate at B_C . Figure 2.11 describes this phenomena. Alternatively, when field is applied perpendicular to the sublattice magnetization, the magnetic moments rotate gradually until they fully align with the direction of applied field.

In order to quantify these effects, we investigate the total energy of a magnetic system E , which is given as:

$$E = -MB\cos\theta - MB\cos\phi + AM^2\cos(\theta + \phi). \quad (2.18)$$

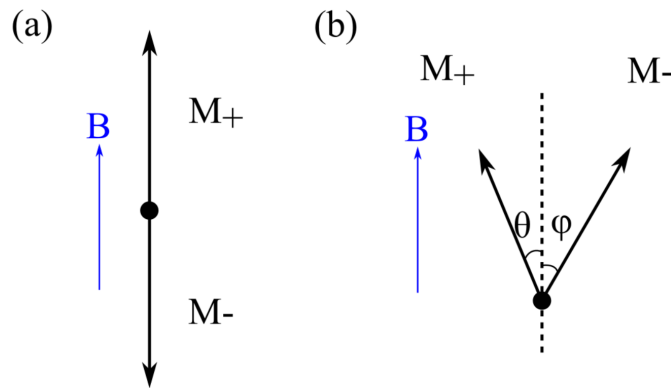


Figure 2.11: When magnetic field is applied parallel to the sublattice magnetization, (a) the spins are unaffected at low fields and (b) at a critical field, the system undergoes a spin-flop transition. [64]

Here, A represents a constant associated with the exchange coupling. In order to account for magnetic anisotropy in systems, an additional term is necessary of the form

$$-\frac{1}{2}\Delta(\cos^2\theta + \cos^2\phi) \quad (2.19)$$

where Δ is a constant. This takes into account competing magnetic sublattices, which are common in correlated systems, and the fact that magnetization prefers a certain crystallographic axis. The energy for an antiferromagnet [Fig. 2.11 (a)] is given by:

$$E = AM^2 - \Delta. \quad (2.20)$$

Conversely, that of the spin-flop case [Fig. 2.11 (b)] is given as:

$$E = -2MB\cos\theta + AM^2\cos 2\theta - \Delta\cos^2\theta. \quad (2.21)$$

Since $\partial E/\partial\theta = 0$, we know that a minimum energy must exist when $\theta = \cos^{-1}[B/2M]$, which ignores the anisotropy term. Substitution of this equation back into E reveals the results shown in Fig. 2.12. Below the spin-flop transition B_{SF} , the antiferromagnetic conformation has the lowest energy. Above B_{SF} these energies switch and the spin-flop phase demonstrates the lowest energy.

In addition to these low-field transitions, antiferromagnetic materials also undergo magnetically driven quantum phase transitions in which at sufficiently low temperatures, field drives the spins to the fully saturated magnetic state. These transitions are most easily investigated with molecule-based magnetic materials, since their saturation fields are generally accessible with powered magnets. Because these materials

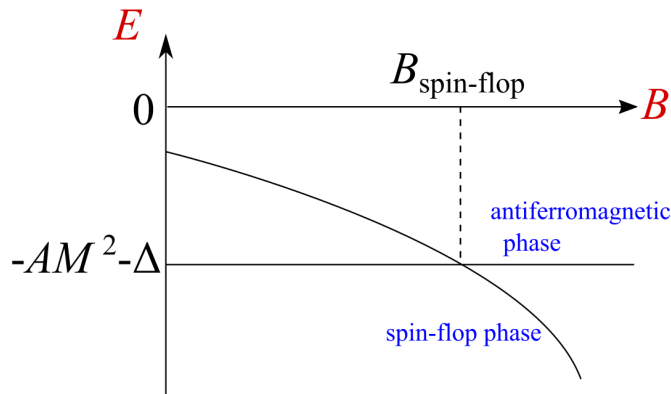


Figure 2.12: Energies of the antiferromagnetic and spin-flop phases as a function of increasing magnetic field.

are comprised of organic linkers between the metal centers, the lattices are flexible and often distort with magnetic field. Given the total magnetic exchange equation

$$J_{tot} = J_{AFM} + J_{FM}, \quad (2.22)$$

field-induced lattice distortions reduce the antiferromagnetic component J_{AFM} , allowing the ferromagnetic component J_{FM} to become the dominant exchange. These distortions are measured with magneto-infrared or magneto-Raman spectroscopic techniques. Microscopic changes in the lattice with magnetic field oftentimes track the square of the magnetization [112], demonstrating that the spin and the lattice are intimately coupled in these systems and revealing the microscopic mechanisms that these systems undergo in order to drive through magnetic quantum phase transitions. These effects are studied in the infrared as well as the optical region. [29, 110]

A number of materials have been studied in this regard. For example, in $\text{Co}[\text{N}(\text{CN})_2]$ and $\text{Mn}[\text{N}(\text{CN})_2]_2$, distortions of the Co-N octahedra and Mn displacements changes in response to applied magnetic field. [29, 113] In the quasi-two-dimensional magnet $[\text{Cu}(\text{HF}_2)(\text{pyz})_2]\text{BF}_4$, pyrazine deformations track the transition to the fully saturated magnetic state. [114] These findings led to the discovery that

magneto-active distortions and the fully polarized state could be linked. In the works discussed in this dissertation, we present a unifying picture of magneto-infrared active distortions and how they compliment and drive the magnetic quantum phase transition.

2.5 Materials of interest in this work

2.5.1 $[(\text{CH}_3)_2\text{NH}_2]M(\text{HCOO})_3$ ($M=\text{Mn}^{2+}$, Co^{2+} , Ni^{2+}) molecule-based magnets

Hybrid organic-inorganic framework structures have attracted considerable attention recently due to their unique properties. They are similar to traditional metal organic frameworks in that their cavities can absorb gases and allow for shape-selective catalysis. [115] However, they are more robust, with rigid organic linkers and inorganic clusters at the joints, and they can be tailored for specific functionalities contingent upon their size and chemical environment. [116] Compounds of the perovskite oxide formula allow room for spacial adjustment of the cation and transition metal ion constituents. The metal ions donate a magnetic component while the organic ligands provide control of the oxidation state, polarizability, and ferroelectricity. [70] Hybrid frameworks, by definition, are extended networks with infinite bonding connectivity in at least one dimension. They have an M - L - M connectivity, where M is a metal ion center and L is a ligand. [117, 118] This is a basis for many physical properties including ferromagnetism and conductivity because the connectivity mediates magnetic exchange. Applications of these multifunctional materials range from energy storage to microelectronics, and now with new discoveries, they can be multiferroic. [119]

$[(\text{CH}_3)_2\text{NH}_2]M(\text{HCOO})_3$ ($M = \text{Mn}^{2+}$, Co^{2+} , Ni^{2+}) is a family of hybrid organic-

inorganic perovskites and molecular multiferroics with an array of interesting properties. [56] These systems possess the perovskitelike ABX_3 structure, where A is an amine, B is a transition metal ion, and X is an $HCOO^-$ ligand that connects the metal centers [Fig. 2.13 (c)]. At room temperature, the metal centers are surrounded by symmetric oxygen octahedra and are connected in a pseudo-cubic fashion via formate ligands [Fig. 2.13 (a)]. Rotating dimethylammonium cations sit in the middle of the cavity along a three-fold axis. The counterion behavior introduces a number of chemical complexities – they are linked to the framework via hydrogen bonding ($N-H \cdots O$), and the nitrogen is disordered over three equivalent positions. Below an order/disorder transition T_C , hydrogen bonding overtakes thermal fluctuations and the nitrogen atom locks into one of three positions. This transition is associated with a space group change from a rhombohedral ($R\bar{3}c$) to a monoclinic

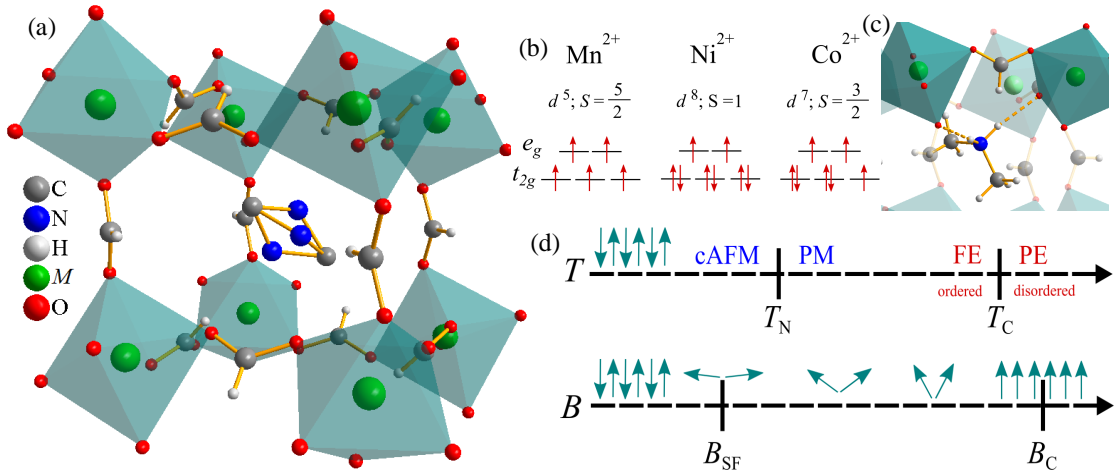


Figure 2.13: (a) Crystal structure of $[(CH_3)_2NH_2]M(HCOO)_3$ ($M=Mn^{2+}, Co^{2+}, Ni^{2+}$) at room temperature showing the metal centers, formate ligands, and disordered dimethylammonium. [56] (b) Electronic and spin states for the various metal centers. (c) Close-up view of the dimethylammonium counterion in the low-temperature, ordered state. (d) Temperature and magnetic field energy scales showing the characteristic transitions. cAFM = canted antiferromagnet, PM = paramagnet, FE = ferroelectric, PE = paraelectric, B_{SF} = spin flop field, and B_C = saturation field. [120]

(Cc) lattice system – below this transition, the materials become ferroelectric. [121] The M -O bonds, which are equal at room temperature, become slightly unique at low temperature, distorting the octahedra and the framework. [56, 122] Hydrogen bonding interactions through T_C in the Mn^{2+} complex have been investigated via neutron scattering, revealing the specific distortions responsible for the phase transition. [123] Recent theoretical modeling also shows that the overall polarization is derived from the dipole moment as well as the tilting angle of the cations, creating spontaneous polar domains below T_C . [38] Below T_C , polarization is enhanced by magnetic field [Fig. 2.14 (b)], although there is some debate about the extent of this magnetoelectric coupling. [37, 38, 124]

With a further decrease in temperature, these materials order magnetically, going from a high-temperature paramagnetic phase to a low-temperature non-collinear antiferromagnetic state below T_N . [56, 125, 126] This transition, along with the order/disorder transition, is seen in heat capacity measurements [Fig. 2.14 (a)]. Local

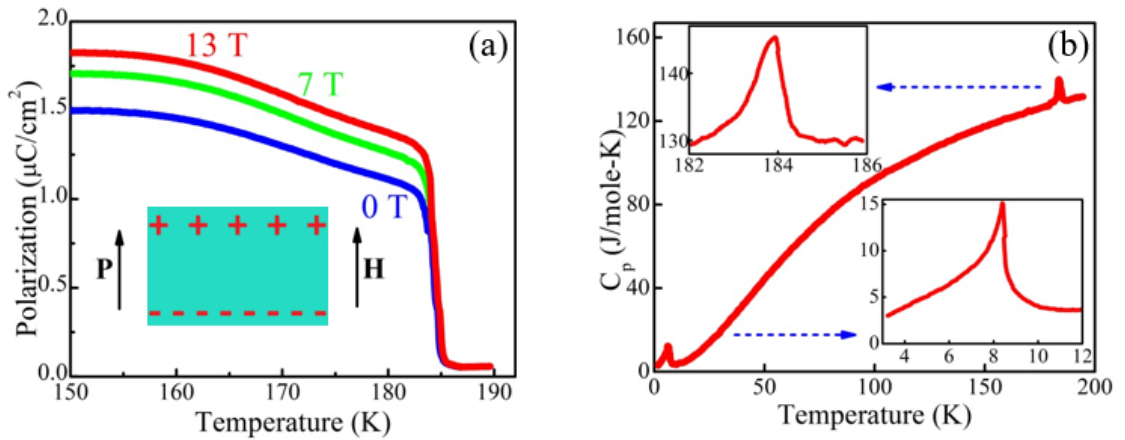


Figure 2.14: (a) Electric polarization in $[(CH_3)_2NH_2]Mn(HCOO)_3$ was applied in conjunction with magnetic fields of 0, 7, and 13 T. It is clear that ferroelectricity improves with application of magnetic fields, showing a direct magnetoelectric effect. [37] (b) Heat capacity of $[(CH_3)_2NH_2]Mn(HCOO)_3$ reveals the structural and magnetic transitions. [56] Similar results are seen in the Ni^{2+} and Co^{2+} complexes, albeit at different energy scales.

paramagnetic metals are linked by organic ligands to create a superexchange pathway of Mn-O-C-O-Mn. The bridging ligands effectively mediate magnetic coupling between the manganese ions, which act as the local spin carriers. Below the magnetic transition temperature, spin canting of 0.08° occurs due to spin-orbit coupling. Magnetic field also drives a series of transitions. Magnetization measurements reveal a spin flop B_{SF} in all complexes and a saturation field B_{C} in the Mn^{2+} complex. [30] These energy scales are schematically summarized in Fig. 2.13 (d) and quantitatively tabulated in Table 2.3. The magnetic field-temperature phase diagram, which tracks these transitions as a function of temperature, is shown in Fig. 2.15. [30]

Naturally, B -site substitution modifies the magnetic properties. [61, 127] The Mn^{2+} system has received the most attention thus far because, as we discuss in this dissertation, energy scales are experimentally accessible. Less is known about the Co and Ni analogs. Data from our investigations and other work suggest that the general character of the temperature- and magnetic-field-driven transitions are similar, although the exact values of T_{C} , T_{N} , B_{SF} , and B_{C} vary depending on the identity of the metal center. In $[(\text{CH}_3)_2\text{NH}_2]\text{Co}(\text{HCOO})_3$, the magnetic moment also changes

Table 2.3: Comparison of important properties in $[(\text{CH}_3)_2\text{NH}_2]M(\text{HCOO})_3$ ($M=\text{Mn}^{2+}$, Co^{2+} , Ni^{2+}). Here, P is the polarization, J is the dominant exchange energy (calculated according to molecular field theory [126] as well as DFT) and other symbols are defined in the caption of Figure 1. Parameters measured in other works are cited, whereas ‡ indicates values derived in this dissertation. [120]

| Property | Mn | Co | Ni |
|--------------------------|-----------------|----------------|-----------------|
| S | 5/2 | 3/2 | 1 |
| T_{C} (K) | 185 [56] | 165 [56] | 180 [56] |
| T_{N} (K) | 8.5 [56, 126] | 14.9 [56, 126] | 38.5 [56, 126] |
| B_{SF} (T) | 0.31 [30] | 11.2‡ | 7.7‡ |
| B_{C} (T) | 15.3 [30] | 88‡ | 125‡ |
| P (C/cm ²) | 1.5 [37] | – | – |
| J (K) | -0.64 [56, 126] | -3.2 [56, 126] | -6.79 [56, 126] |
| J (K) DFT | -1.12‡ | -3.79‡ | -24.6‡ |

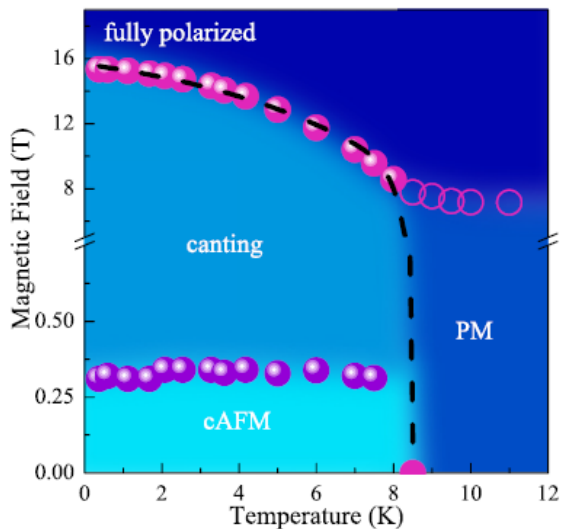


Figure 2.15: Magnetic field-temperature phase diagram of $[(\text{CH}_3)_2\text{NH}_2]\text{Mn}(\text{HCOO})_3$, highlighting the canted antiferromagnetic (cAFM), canting, fully polarized, and paramagnetic (PM) regions. [30] Long-range interactions fall off above the Néel transition at 8.5 K.

across T_C , suggesting a modification of the spin state at the ferroelectric transition [Fig. 2.16 (a)]. [40] This is not seen in the other analogs. [40] The Co compound also exhibits glassy magnetism due to the presence of magnetic phase coexistence near $T_N=14.9$ K [Fig. 2.16 (b)]. [125,128] Detailed vibrational mode assignments have been proposed for the Ni compound, and dielectric and magnetization measurements reveal signatures of the transitions. [56,129]

2.5.2 $[\text{Cu}(\text{pyz})_2(2\text{-HOpy})_2](\text{PF}_6)_2$ and $[\text{Cu}(\text{pyz})_{1.5}(4\text{-HOpy})_2](\text{ClO}_4)_2$ copper halide complexes

Molecule-based materials offer fascinating opportunities to investigate the interplay between structure and magnetism. [130–135] Soft ligands, which link the metal centers and introduce characteristically low energy scales and flexible architectures, are crucial to driving new quantum phases and exciting functionality. [4, 24, 136–139] Copper halide complexes are outstanding platforms with which to explore these

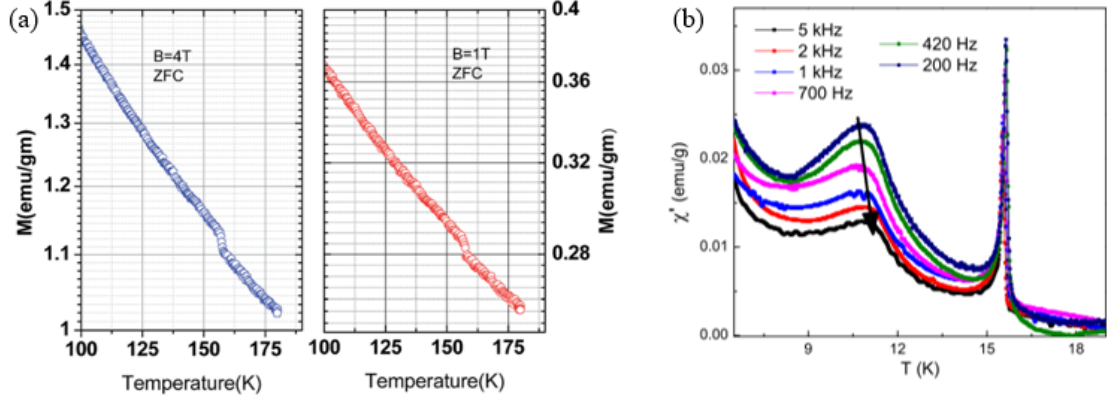


Figure 2.16: (a) Magnetization versus temperature of $[(\text{CH}_3)_2\text{NH}_2]\text{Co}(\text{HCOO})_3$ at 4 and 1 T. The jump in magnetization coincides with the structural transition, indicating a possible change in the magnetic moment of the Co^{2+} ion. [40] (b) Temperature dependence of the ac susceptibility in $[(\text{CH}_3)_2\text{NH}_2]\text{Co}(\text{HCOO})_3$, showing two transitions at 15.1 K and 11 K. The shift in frequency of the 11 K peak is indicative of glassy nature or magnetic frustration between two competing magnetic phases. [125]

ideas. They sport low-dimensional quantum ($S=1/2$) behavior, strong hydrogen bonds that act as exchange pathways, and magnetic quantum phase transitions at experimentally-realizable fields that emanate from the overall low magnetic energy scales. [140–142] This allows for a complete study of their unique magnetic properties, since J values are generally small. [143] Quantum phase transitions are different from traditional phase transitions in that they are governed by a physical tuning parameter like magnetic field, composition, or pressure rather than by thermal fluctuations. [21–24] Those involving applied field are most well studied. These materials also provide a platform for unraveling some of the properties of high-temperature copper oxides. [144, 145] Copper halide complexes crystallize in a variety of patterns and dimensionalities, ranging from zero-dimensional systems to three-dimensional networks. [31, 130, 146, 147] Figure 2.17 summarizes the various cases. In this dissertation, we focus on two copper halide complexes $[\text{Cu}(\text{pyz})_2(2\text{-HOpy})_2](\text{PF}_6)_2$ and $[\text{Cu}(\text{pyz})_{1.5}(4\text{-HOpy})_2](\text{ClO}_4)_2$.

$[\text{Cu}(\text{pyz})_2(2\text{-HOpy})_2](\text{PF}_6)_2$ is a highly isolated two-dimensional $S=1/2$ Heisen-

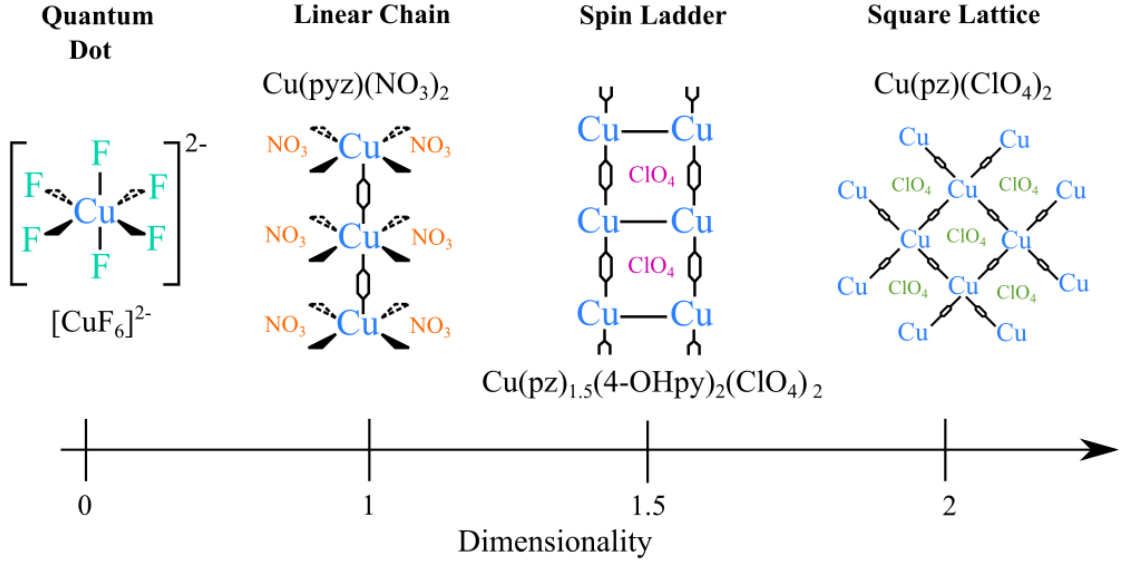


Figure 2.17: Summary of Cu halide complexes as a function of increasing dimensionality.

berg antiferromagnet. The Cu^{2+} centers are six-coordinated and linked via pyrazine ligands in the ab -plane to create an infinitely-extending, two-dimensional square lattice. These layers are stabilized along the c -axis via hydrogen-bonding interactions from pyridone ligands to uncoordinated PF_6^- anions [Fig. 2.18 (a)]. [148] Antiferromagnetism develops below $T_N = 1.37$ K, and the intralayer exchange strength is 6.8 K. The latter corresponds to a magnetic saturation field of 19 T. [148] Although two-dimensional magnetism is (in general) well-studied, [13, 143] the large layer isolation in $[\text{Cu}(\text{pyz})_2(2\text{-HOpy})_2](\text{PF}_6)_2$ sets it apart. [149, 150]

The structure of $[\text{Cu}(\text{pyz})_{1.5}(4\text{-HOpy})_2](\text{ClO}_4)_2$ is quite different. [148] In this material, the Cu^{2+} centers are coupled through pyrazine ligands along the a - and b -axis. Here, Cu^{2+} is five-coordinated, and pyridone serves as a capping ligand for the metal centers. They are stabilized in a staggered formation by hydrogen bonds to semi-coordinated perchlorate (ClO_4^-) groups [Fig. 2.18 (b)]. Thus, the system is a spin ladder in which $\text{Cu} \cdots \text{Cu}$ interactions are oriented along the b -axis but do not extend in other directions. Instead, hydrogen-bonding interactions hold the ladders

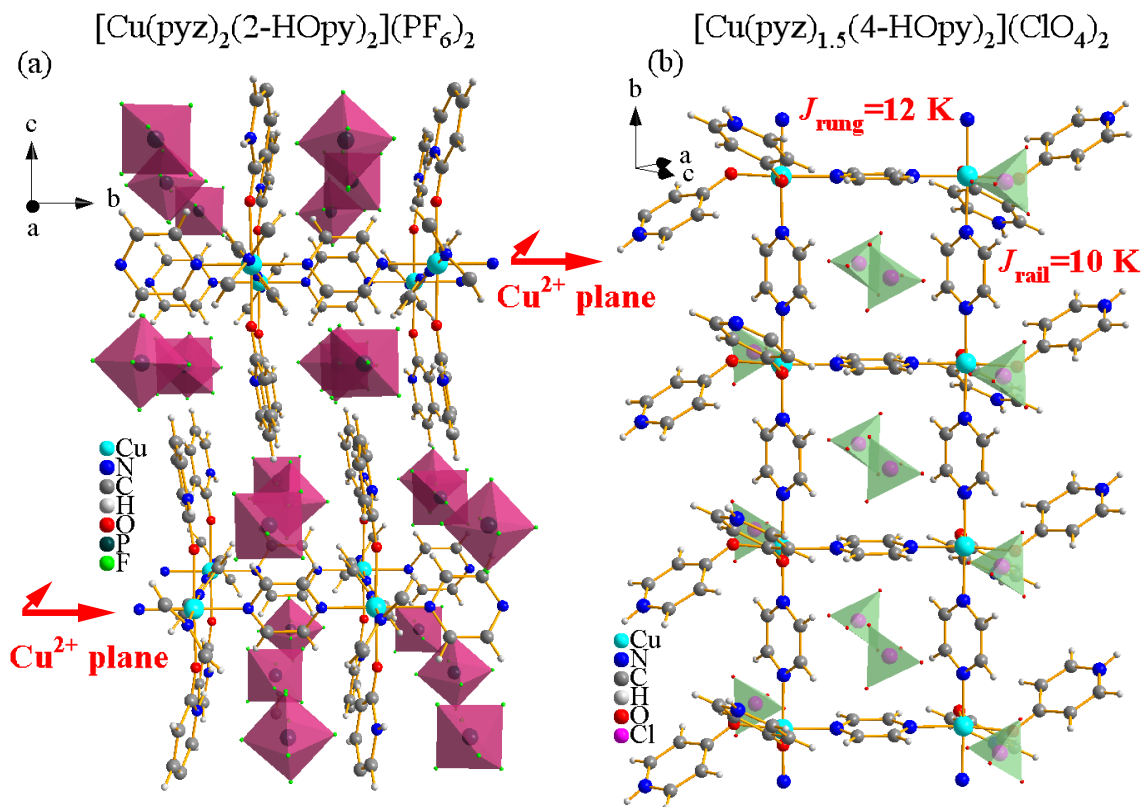


Figure 2.18: (a) Crystal structure of $[\text{Cu}(\text{pyz})_2(2\text{-HOpy})_2](\text{PF}_6)_2$ emphasizing the layered, infinitely extending Cu^{2+} planes. (b) View of the ladder structure $[\text{Cu}(\text{pyz})_{1.5}(4\text{-HOpy})_2](\text{ClO}_4)_2$. Exchange strengths of the rung vs rail are indicated. [148]

together. Susceptibility measurements give exchange interactions of $J_{\text{rung}}=10.4$ K and $J_{\text{rail}}=12$ K, resulting in $J_{\text{rung}}/J_{\text{rail}}=0.87$ – very close to an isotropic value. [148] This material bridges an important gap in the field of low-dimensional magnetism by providing a physical realization of a spin-ladder system with modest energy scales and $J_{\text{rung}}/J_{\text{rail}}$ close to 1.0. High field magnetization reveals a spin gap Δ at 4 T and a 24 T saturation field B_C . [148] Table 2.4 summarizes these properties. Importantly, the magnetic quantum phase transitions are accessible with powered magnets. This allows exploration of properties across B_C .

2.5.3 Hydrogen-bonded multiferroic $(\text{NH}_4)_2[\text{FeCl}_5 \cdot (\text{H}_2\text{O})]$

$(\text{NH}_4)_2[\text{FeCl}_5 \cdot (\text{H}_2\text{O})]$ is the multiferroic member of the $A_2[\text{FeX}_5(\text{H}_2\text{O})]$ ($X =$ halide ion, $A =$ alkali metal or ammonium) family of erythrosiderite-type compounds. In this system, $[\text{FeCl}_5(\text{H}_2\text{O})]^{2-}$ groups are arranged in a herringbone-like connectivity along the a -axis; the structure is governed by ionic as well as hydrogen bonding interactions ($\text{O-H} \cdots \text{Cl}$), making this a rare case of a purely molecular multiferroic. Ammonium (NH_4^+) units are present to fill voids and balance charge [Fig. 2.19 (a)].

This system sports a series of transitions with temperature [Fig 2.19 (c)] including a 79 K order-disorder structural transition associated with the development of hydrogen bonds from the NH_4^+ counterions [151], magnetic ordering of the $S=5/2$ Fe^{3+} centers below $T_N=7.25$ K to an incommensurate-collinear sinusoidal structure, [61, 152]

Table 2.4: Summary of properties comparing $[\text{Cu}(\text{pyz})_2(2\text{-HOpy})_2](\text{PF}_6)_2$ and $[\text{Cu}(\text{pyz})_{1.5}(4\text{-HOpy})_2](\text{ClO}_4)_2$. Values derived in this work are labeled with a ‡.

| Anion | T_N (K) | Δ (T) | B_C (T) | J (K) | P_C (GPa) |
|------------------|-----------|--------------|-----------|-----------------------------|-------------|
| PF_6^- | 1.37 | – | 19 | 6.8 (ab -plane) | 3.7‡ |
| ClO_4^- | < 1.5 | 4 | 24 | 10.4 (rung); 12.0 (rail) | 4.5‡ |

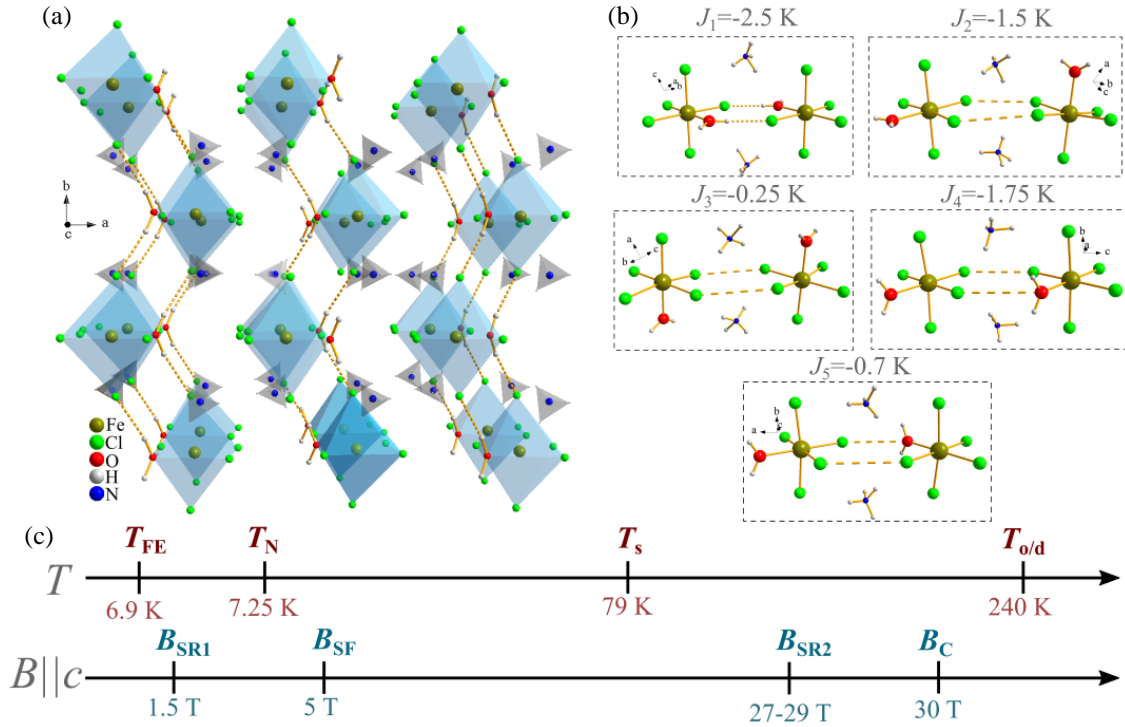


Figure 2.19: (a) Crystal structure of $(\text{NH}_4)_2[\text{FeCl}_5(\text{H}_2\text{O})]$. Hydrogen-bonding interactions (O-H \cdots Cl) govern the herringbone-like connectivity. [61] (b) Summary of the various exchange pathways mediated by hydrogen- and ionic-bonding, along with the strength of each pathway. (c) Summary of the important temperature- and field-driven transitions. $T_{\text{o/d}}$ is a reported order/disorder transition, T_{S} is an isostructural distortion, and T_{N} and T_{FE} give the Néel and ferroelectric transitions, respectively. Along the field axis, B_{SR1} and B_{SF} are the low-field spin reorientation and spin-flop transitions; B_{SR2} and B_{C} are the high-field spin reorientation and the saturation field. [61]

and the onset of ferroelectricity below $T_C= 6.9$ K that arises due to a transition to an incommensurate-cycloidal spin state. [61, 153] The structural transition at 79 K is not associated with a space group change, unlike many other molecule-based materials. [120, 154]

The magnetic and electronic properties of $(\text{NH}_4)_2[\text{FeCl}_5 \cdot (\text{H}_2\text{O})]$ are quite complex and intimately linked. At zero magnetic field, the spins lie in the ac plane; low-field susceptibility measurements reveal that the magnetic easy axis is along a . The magnetic ground state gives rise to five important exchange couplings (J_1 - J_5) which are antiferromagnetic in nature [Fig 2.19 (b)]. [61] These include multiple superexchange pathways: $\text{Fe-Cl} \cdots \text{Cl-Fe}$, $\text{Fe-O} \cdots \text{Cl-Fe}$, and $\text{Fe-O-H} \cdots \text{Cl-Fe}$. [155] However, the spins lying within the ac plane are ordered ferromagnetically – despite the overall antiferromagnetic nature – and drive magnetic frustration in this system, different than the K and Rb analogs. With applied magnetic field, $(\text{NH}_4)_2[\text{FeCl}_5 \cdot (\text{H}_2\text{O})]$ undergoes a series of spin-flop transitions between 3 and 5 T along with magnetic saturation near 30 T. [61, 90] Figure 2.20 summarizes (a) the first B - T phase diagram at low magnetic fields [61] and the (b) more recent, full-field B - T phase diagram

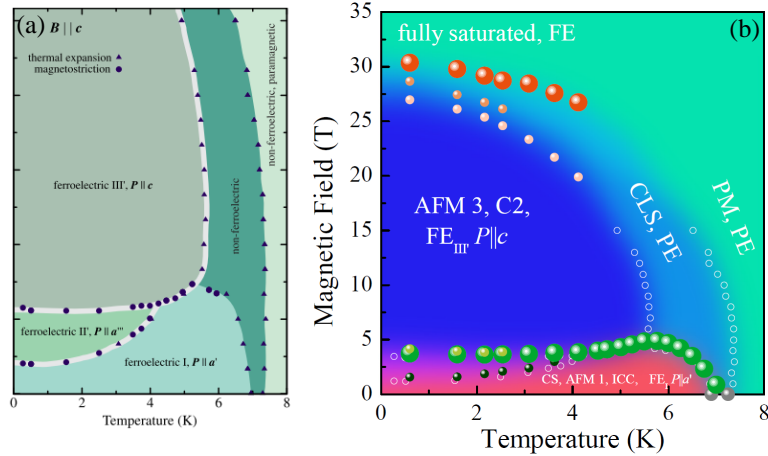


Figure 2.20: (a) Low field B - T phase diagram of $(\text{NH}_4)_2[\text{FeCl}_5 \cdot (\text{H}_2\text{O})]$, highlighting the different ferroelectric phases. [61] (b) Full B - T phase diagram, including the small spin reorientations that lead up to magnetic saturation. [90]

that includes the high field spin reorientations and the full field magnetic saturation transition. [90] In the work presented later in this dissertation, we investigate the polarization effects associated with the high-field transitions.

Fascinatingly, the magnetic spin-flop transitions are also accompanied by spontaneous electric polarization changes. This is in contrast to the isostructural analogs, which have only one magnetic transition and no spontaneous electric polarization. [155] In zero magnetic field, the spontaneous electric polarization lies within the ab plane, nearly pointing along the a -axis ($P_a=3 \mu\text{Cm}^{-2}$, $P_b= 0.3 \mu\text{Cm}^{-2}$, $P_c=0 \mu\text{Cm}^{-2}$ at 3 K). Applied magnetic field (~ 4 T) along a causes the spins to slightly reorient, where they are directed $\sim 2^\circ$ towards the b -axis. An increase in magnetic field to approximately 5 T rotates the polarization 90° from the ab plane to the c -axis [Fig. 2.21 (a-c)]. [61] It therefore follows that polarization is zero along the c -direction when $B \parallel a$ until 5 T, at which point polarization continues to grow with increasing magnetic field. Similar effects occur with $B \parallel a$. Small, low-field reorientations also change the value of the electric polarization, as seen by the distinct increase in Fig. 2.21 (c) at 2 T. Figure 2.21 (e) displays the magnetic field dependences of the electric polarizations for magnetic field applied along a . At nearly 5 T, abrupt suppressions of P_a and P_b along with the induction of P_c reveals the spin reorientation as a function of magnetic field from the ab plane into the c direction. [61] Figure 2.21 (d) displays the low-temperature magnetization vs magnetic field response of $(\text{NH}_4)_2[\text{FeCl}_5 \cdot (\text{H}_2\text{O})]$, supporting the fact that the spontaneous electric polarization and magnetic spin-flop transitions occur simultaneously – no spin flop transitions occurs with $B \parallel b$ because unlike the a and c -axes, the orientation is nearly unchanged. [61]

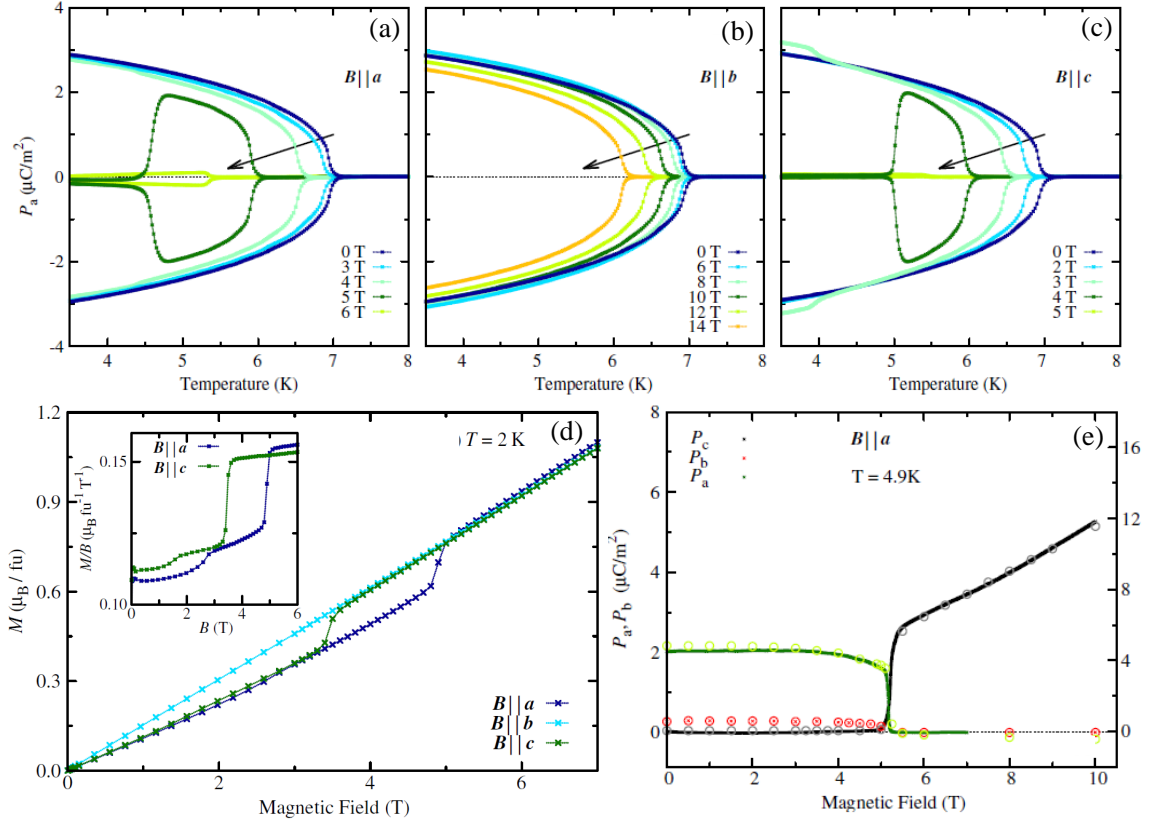


Figure 2.21: (a-c) Temperature dependences of spontaneous electric polarization P_a for magnetic fields applied parallel to the a , b and c axes. (d) Magnetization versus magnetic field applied parallel to a , b and c . (e) Magnetic field dependence of the electric polarization P_a , P_b , and P_c as a function of magnetic field. [61]

Chapter 3

Methods

3.1 Optical spectroscopy

Spectroscopy describes the interaction of light with matter and is essential for the microscopic study of quantum materials. The promotion of electrons to high energy states gives rise to characteristic, material-dependent excitations – the interpretation of the absorption spectra is fundamental in understanding the intimate coupling of the lattice, magnetic and electronic aspects of a system. Infrared spectroscopy is particularly well-suited for studying these properties, as it is a microscopic technique that probes fundamental excitations of the crystalline lattice. Accordingly, it gives rise to a number of important topics including the investigation of phonons and electronic properties, phonon displacement patterns through phase transitions, the extraction of important order parameters, mechanisms that drive quantum phase transitions, and many other physical properties of a material. [83, 156–158]

3.1.1 Maxwell's equations

In order to understand the interactions between light and matter, which is the foundation of spectroscopy, a firm understanding of Maxwell's equations is necessary. These equations describe how electric field generates a magnetic field, and vice versa. There are four microscopic equations – two describe how fields emerge from charge, and two express how fields circulate around their respective sources. These equations, which take into account total charge and total current, are:

$$\nabla \cdot \mathbf{E} = \frac{\rho}{\epsilon_0} \quad (3.1)$$

$$\nabla \cdot \mathbf{B} = 0 \quad (3.2)$$

$$\nabla \times \mathbf{E} = -\frac{\partial \mathbf{B}}{\partial t} \quad (3.3)$$

$$\nabla \times \mathbf{B} = \mu_0 \mathbf{J} + \mu_0 \epsilon_0 \frac{\partial \mathbf{E}}{\partial t}. \quad (3.4)$$

Here, \mathbf{E} and \mathbf{B} are electric and magnetic fields, ρ and \mathbf{J} are the charge and current densities, and ϵ_0 and μ_0 are the permittivity and permeability of free space, respectively. Equation 3.1, Gauss's Law, describes how an electric field \mathbf{E} generates electric charges. Generally, field lines develop because electric fields point away from a positive charge and towards a negative charge. Gauss's law for magnetism, Eqn. 3.2, states that magnetic fields, unlike electric fields, only exist in loops and no net magnetic charges occur. However, the Maxwell-Faraday equation (Eqn. 3.3) shows that an electric field loop can only occur in regions where there is a changing magnetic field. Finally, Eqn. 3.4, Ampere's law with Maxwell's correction, summarizes the relationship between electric and magnetic fields: a change in the electric field can create a magnetic field, and vice versa. In this way, an electromagnetic wave travels through empty space.

Maxwell's microscopic equations take into account the contribution of each charged particle, making it nearly impossible to solve optical problems. Therefore, the equations can be rewritten in terms of macroscopic quantities, since a spectroscopic measurement probes materials on the order of a wavelength of light rather than on the atomic level. [159] The new equations therefore become:

$$\nabla \cdot \mathbf{D} = \rho^{ext} \quad (3.5)$$

$$\nabla \cdot \mathbf{B} = 0 \quad (3.6)$$

$$\nabla \times \mathbf{E} = -\frac{\partial \mathbf{B}}{\partial t} \quad (3.7)$$

$$\nabla \times \mathbf{H} = \frac{\partial \mathbf{D}}{\partial t} + \mathbf{J}^{cond} + \mathbf{J}^{ext}. \quad (3.8)$$

Here, \mathbf{E} and \mathbf{H} are electric field and magnetic fields, \mathbf{D} is the displacement field, \mathbf{B} is magnetic induction, \mathbf{J}^{cond} is current density due to the conduction electrons, and \mathbf{J}^{ext} and ρ^{ext} are current and charge density. In an isotropic medium, and within a linear approximation, the following relationships can be assumed:

$$\mathbf{P} = \chi_e \mathbf{E} \quad (3.9)$$

$$\mathbf{M} = \chi_m \mathbf{H} \quad (3.10)$$

$$\mathbf{J}^{cond} = \sigma \mathbf{E} \quad (3.11)$$

$$\mathbf{D} = \varepsilon \mathbf{E} \quad (3.12)$$

$$\mathbf{B} = \mu \mathbf{H}, \quad (3.13)$$

where \mathbf{P} is the polarization, \mathbf{M} is the magnetization, χ_e is the electric susceptibility, χ_m is the magnetic susceptibility, σ is the conductivity, ε is the dielectric constant,

and μ is the magnetic permeability. These properties can be introduced into Eqns. 3.5-3.8 to give a new set of equations which are no longer exact.

These inexact equations can be simplified by considering the interaction of light and a medium. In an isotropic medium, $p^{ext}=0$ and there is no spatial variation in ε . Therefore, these equations can be combined to obtain the wave equation for a plane wave that propagates in an energy-absorbing medium:

$$\nabla^2 \mathbf{E} = \frac{\mu}{c^2} \frac{\partial^2 \mathbf{E}}{\partial t^2}. \quad (3.14)$$

Because experiments on optical properties are generally performed using monochromatic light, the wave vector used to describe the propagation of a single plane within an isotropic medium is:

$$\mathbf{E} = \mathbf{E}_0 e^{i(\mathbf{k}\mathbf{r} - \omega t)} \quad (3.15)$$

where \mathbf{k} is the wave vector and ω is the frequency. Substitution into Eqn. 3.14 gives:

$$k^2 = \frac{\omega^2}{c^2} \varepsilon(\omega). \quad (3.16)$$

The propagation constant can be expressed by the complex index of refraction $\tilde{N} = \sqrt{\varepsilon(\omega)}$ to give:

$$k = \frac{\tilde{N}\omega}{c}. \quad (3.17)$$

$\tilde{N}(\omega)$ can be defined as

$$\tilde{N}(\omega) = n(\omega) + i\kappa(\omega) \quad (3.18)$$

and the complex dielectric function as:

$$\varepsilon(\omega) = \varepsilon_1 + \varepsilon_2. \quad (3.19)$$

Here, n is the refractive index and κ is the extinction coefficient. The real and imaginary parts of $\tilde{N}(\omega)$ and $\varepsilon(\omega)$ are given as:

$$\varepsilon_1 = n^2 - \kappa^2 \quad (3.20)$$

$$\varepsilon_2 = 2n\kappa. \quad (3.21)$$

Based off of these equations, several different relations can be derived. Below, we focus on the extraction of the absorption coefficient α . Because my experiments are performed on solids, the incoming electromagnetic wave is dampened upon contact. Therefore, Eqn. 3.15 can be rewritten as:

$$E(x, t) = E_0 e^{i[(\tilde{N}\omega/c)x - \omega t]} = E_0 e^{-(2\pi\kappa/\lambda_\omega)x} e^{i(kx - \omega t)}. \quad (3.22)$$

Here, $2\pi\kappa/\lambda_\omega$ gives the attenuation of the wave amplitude and λ_ω is the wavelength of light in a vacuum. Because the intensity I of a given wave is proportional to the square of the electric field (EE^*), it can be compared to Beer's Law by:

$$I = EE^* = I_0 e^{-\alpha x}. \quad (3.23)$$

In this way, the absorption α and the extinction coefficient κ are related as:

$$\alpha = \frac{2\omega\kappa}{c} = \frac{4\pi\kappa}{\lambda_\omega}. \quad (3.24)$$

Additionally, α is related to the imaginary part of the dielectric function via:

$$\alpha = \frac{\omega\varepsilon_2}{cn}. \quad (3.25)$$

The dielectric function expression for a medium with a finite conductivity is given as:

$$\varepsilon(\omega) = 1 + \frac{i\sigma(\omega)}{\omega\varepsilon_0} \quad (3.26)$$

and the absorption as:

$$\alpha = \frac{\sigma_1}{n\varepsilon_0c}. \quad (3.27)$$

Conductivity $\sigma(\omega)$ is complex and has both real σ_1 and imaginary σ_2 components. Various relationships can arise between the functions $\varepsilon(\omega)$, $\sigma(\omega)$, and $\tilde{N}(\omega)$. In this work, we will primarily be interested in $\alpha(\omega)$.

3.1.2 The harmonic oscillator and infrared spectroscopy

The harmonic oscillator is commonly used to understand the vibrational spectra of a system. The Schrödinger equation for the diatomic oscillator problem can be treated quantum mechanically to give [160]:

$$\frac{\hbar^2}{2\mu} \frac{d^2\psi}{dx^2} + V(x)\psi(x) = E\psi(x). \quad (3.28)$$

Here, $\hbar = h/2\pi$, μ is the effective mass, the potential energy $V(x) = \frac{1}{2}kx^2$, k is the force constant, and x is the vibrational coordinate $r - r_e$. By solving this equation for quantized energy values, the new equation yields:

$$E_\omega = h\omega\left(n + \frac{1}{2}\right), n = 0, 1, 2\dots \quad (3.29)$$

with

$$\omega = \frac{1}{2\pi} \left(\frac{k}{\mu}\right)^{1/2} \quad (3.30)$$

where ω is the vibrational frequency and n is the vibrational quantum number. Figure 3.1 displays the energies of the harmonic oscillator potential well. The harmonic oscillator is parabolic and each energy level is equidistant from the next – the separation between them is always equal to $h\omega$. However, this is not the case for a real molecule or material. In fact, separation in materials becomes increasingly smaller with n as the energy approaches the dissociation energy. The difference between the dissociation energy and the lowest point of the potential well is described as D_e . The energy between the $n=0$ (zero-point energy) and the dissociation energy is given by D_0 – this value is measured experimentally. These two energies are related via:

$$D_0 = D_e - \frac{1}{2}h\omega. \quad (3.31)$$

Therefore, since D_e is now quantifiable, the Morse potential energy function is given by:

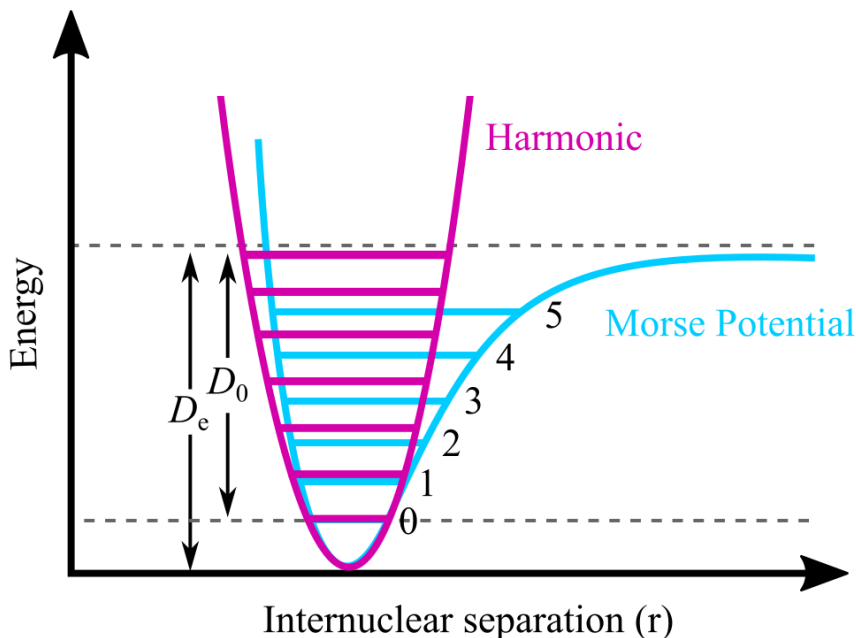


Figure 3.1: Potential wells of the harmonic oscillator and the anharmonic (Morse) potential.

$$V(x) = D_e(1 - e^{-ax})^2 \quad (3.32)$$

where a describes the curvature of the bottom of the potential well and $x = \frac{r-r_0}{r_0}$. This potential energy function is much more realistic in terms of a material and can be substituted into Eqn. 3.28 to give:

$$E_\omega = hc\omega_e(n + \frac{1}{2}) - hc\omega_e x_e(n + \frac{1}{2})^2 + \dots, n = 0, 1, 2... \quad (3.33)$$

where x_e is the anharmonicity constant. [160] The harmonic oscillator approximation is best when n , and the differences between the harmonic and the anharmonic potentials, are small. Based on quantum mechanics and anharmonic oscillator selection rules, all transitions for $\pm\Delta n$ are allowed. Transitions to higher energy levels ($\Delta n = \pm 2, \pm 3...$) are called “overtone modes” and typically much less intense than the fundamental. [160] Lattice dynamics are based upon harmonic oscillator or anharmonic oscillators and describe phenomena such as electromagnetic waves, molecular bonding, and complex lattice vibrations. [161–163]

Infrared spectroscopy can be performed as a transmittance or reflectance experiment. These measurements are crucial for the unveiling of the symmetry of materials, important thermal and electrical properties, and displacement patterns of specific distortions. In this dissertation, we primarily focus on transmittance. Beer’s law, which relates the absorption of a material to the attenuation of light, is therefore implemented. The general equation is given as:

$$I = I_0 e^{-\alpha d} \quad (3.34)$$

where I_0 and I are the intensities of the incident and transmitted beams, α is the absorption coefficient, and d is the thickness of the material. However, spectroscopists

expand on this equation and measure transmittance T (with negligible reflectance) and absorbance A via:

$$T = \frac{I}{I_0} \quad (3.35)$$

$$A = -\ln \frac{I}{I_0} = \alpha d. \quad (3.36)$$

By combining and rearranging these equations, the absorption coefficient, which is material dependent, can be directly calculated:

$$\alpha = -\frac{1}{hd} \ln(T\omega). \quad (3.37)$$

Here, h is the concentration. The incident beam loses some of its energy to the molecular vibration. In this way, absorption as a function of frequency $T(\omega)$ is determined. The infrared spectrum is therefore obtained by plotting intensity vs energy, which is proportional to the energy difference between the ground and excited states. [164]

An important selection rule for infrared absorption spectroscopy is that there must exist a change in the dipole moment during the mode motion – this type of motion is considered to be infrared active. The intensity of the transition to different vibrational states is dependent upon the transition moment integral M :

$$M = \int \psi'_{vib} * \mu(r) \psi''_{vib} dr, \quad (3.38)$$

where ψ'_{vib} describes the excited state and ψ'' the ground state. The dipole moment μ – which is a function of r – expands as a Taylor series about the equilibrium position $r = r_e$. By substituting this expanded equation back into Eqn. 3.38, M can be evaluated. [165] The vibrational response is not allowed if the overlap is equal to zero. If the overlap is nonzero, the transition is thus allowed. The higher power

terms in this series are neglected. The measured infrared intensity is related to the square of the moment operator via:

$$I \propto \left| \frac{d\mu}{dr} \right|_{r_e}^2. \quad (3.39)$$

The vibrations of a solid are different than those of liquids or gases due to the systematic arrangement of molecules, atoms, or ions within a crystalline state. Characteristics of crystalline solids include long-range periodicity, strong intermolecular interactions, selection rules, and confinement effects, among others, which cause energy levels to broaden into bands. [166,167] Phonons, which are collective excitations of a lattice, result from this long-range periodicity. In these excitations, the motion of one atom depends on that of the next. [163] Within a three-dimensional crystalline system where N is the number of atoms in one unit cell, distortions of the lattice are describable in terms of $3N$ branches for the phonon dispersion curves. These dispersion curves contain three acoustic branches and $3N-3$ optical branches. The acoustic phonons refer to translations of the lattice – these are transformations of translational modes in a molecule. On the other hand, optical phonons are the vibrations of a molecule. These motions are generally more interesting to spectroscopists. Figure 3.2 displays the dispersion curves. Optical spectroscopy probes excitations at $k=0$, while inelastic neutron scattering techniques probe the dispersion throughout the entire Brillouin zone. For our techniques, we are only concerned with the optical excitations at $k=0$. As a rule of thumb, these excitations follow:

$$\omega^2 = 2k \left[\frac{1}{M_1} + \frac{1}{M_2} \right] \quad (3.40)$$

where k is the force constant and M_1 and M_2 are two atoms in a linear chain. This can be shortened to

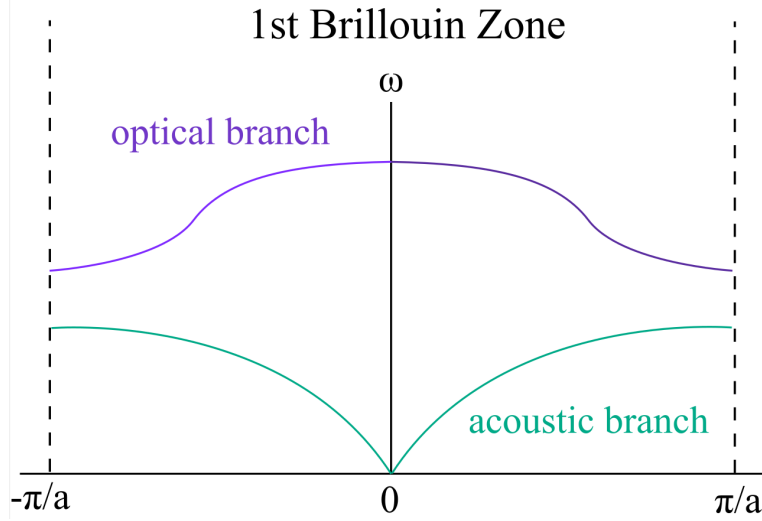


Figure 3.2: Dispersion curves for optical and acoustic branches.

$$\omega \propto \sqrt{\frac{k}{\mu}} \quad (3.41)$$

where μ is the reduced mass. For convenience, phonons in a solid are often divided into localized modes (similar to what exists in an isolated molecule) and collective modes (which can be very long range).

Phonons are normal modes that vibrate with the same frequency and a fixed phase relation. The number of vibrations in a crystalline solid is determined by the overall symmetry of the unit cell in combination with the symmetry of individual molecules within the system. The number of phonons can change with phase transitions and give insight into the specific symmetry aspects of the material. For example, in the molecule based multiferroic $[(\text{CH}_3)_2\text{NH}_2]\text{Mn}(\text{HCOO})_3$, the irreducible representation of the room temperature, paraelectric phase ($R\bar{3}c$ space group) is $\Gamma_{\text{optic}} = 9A_{1g} + 10A_{1u} + 11A_{2g} + 11A_{2u} + 21E_u + 20E_g$. It is clear that in this system, although the number of infrared and Raman active modes are similar, they are not identical. Across the order-disorder transition, the structure lowers in symmetry to a monoclinic space group (Cc) with no inversion symmetry, where the number of

modes increases. This is evidenced by the low temperature irreducible representation $\Gamma_{optic} = 70A' + 71A''$. The rule of mutual exclusion, however, states that a normal mode can be either infrared or Raman active in a system with an inversion center, but not both. This is because in a material with inversion symmetry, infrared active modes must be of ungerade symmetry and Raman active modes must be of gerade symmetry. Of course, in real systems – especially those with low symmetry – Raman modes may appear in infrared spectra and vice versa. The study of phonons in solids is fundamentally important in materials science, as they underlie principles such as thermal and electrical conductivity and give insight into both the elastic and the optical properties of crystalline materials.

3.1.2.1 Lattice dynamics calculations of solids

Density functional theory (DFT) offers a way forward in understanding the vibrations of solids. DFT is one of the most widely used first principles quantum mechanical methods for calculations involving electronic structures of atoms, molecules, and condensed states. [168] It is commonly used to understand the various structural, electronic, and magnetic characteristics of materials. Although it is computationally simple (it takes into account three variables – the three Cartesian directions – as opposed to the $3N$ variables in a many-body wavefunction), it yields high-accuracy calculations of a broad range of scientific problem across chemistry, physics, and materials science. In this work, density functional theory was used to reveal the the structure of $[(\text{CH}_3)_2\text{NH}_2]\text{Mn}(\text{HCOO})_3$ in different magnetic states and to assign vibrations and give displacement patterns of $(\text{NH}_4)_2[\text{FeCl}_5 \cdot (\text{H}_2\text{O})]$. These patterns can be animated to reveal the motion of specific distortions.

3.2 Spectroscopic instrumentation

Spectroscopy describes the intimate interaction of electromagnetic radiation with matter. Electromagnetic radiation spans a broad range of energies from radio frequencies to the infrared region to higher energy x-rays. Based on the energy at which the system is probed, information about the atoms, molecules, or crystal structure can be extracted. The spectrum is therefore a graphical representation of the material-dependent characteristics of a system.

In this work, we are primarily concerned with infrared vibrational spectroscopy, where electrons are promoted from one vibrational energy to another. This interaction can be measured in several ways including absorption and reflection, and it provides information about the vibrations in a solid. Therefore, infrared spectroscopy is a microscopic probe of fundamental excitations of the lattice. In order to understand the vibrations in our systems, we utilize several different spectrometers with overlapping energy ranges from 20 cm^{-1} - 5000 cm^{-1} . These spectrometers are shown in Fig. 3.3. The details of these instruments, along with modifications to access low temperatures and high magnetic fields, are discussed in the following sections.

3.2.1 Fourier transform spectroscopy

In this work, two Fourier transform infrared spectrometers – the Bruker IFS 113v and Bruker Equinox 55 – are utilized. Because they are Fourier transform infrared spectrometers, they measure an interferogram which can then be converted to a single beam spectrum with a Fourier transform. [169] The general theory of interferometers is understood from the basis of the Michelson interferometer.

The schematic in Fig. 3.4 (a) summarizes the optical path of a Michelson interferometer. Here, the source beam strikes a 50/50 beamsplitter, which splits the signal into two. Some of this light passes through to the movable mirror M_1 while

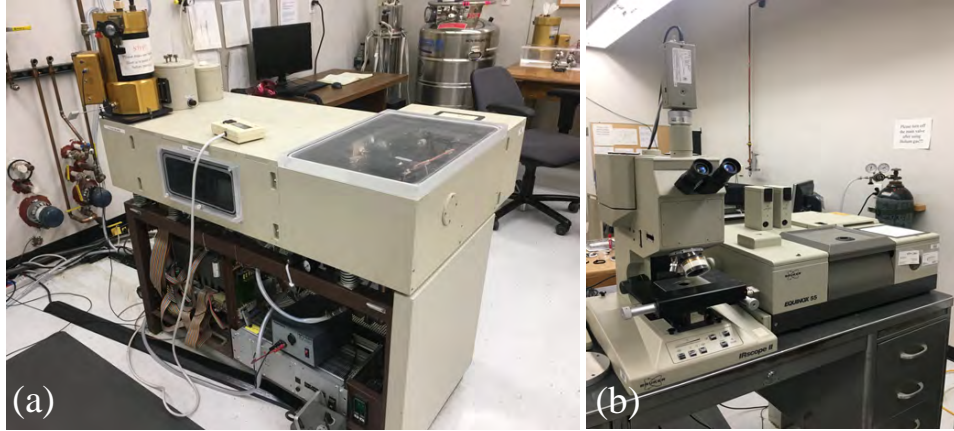


Figure 3.3: Experiments were carried out on a variety of spectrometers including (a) far-infrared measurements on the Bruker IFS 113v ($20\text{-}700\text{ cm}^{-1}$) and (b) middle-infrared measurements on the Bruker Equinox 55 with Bruker IR Scope II attachment ($500\text{-}5000\text{ cm}^{-1}$).

another part is directed 90° from the first to the fixed mirror M_2 . Both beams are then reflected and recombine at the detector into a single beam, causing an interference of signals. A portion of this recombined light is directed back to the source, but the recombined light pertaining to the measurement proceeds to the detector via the sample of interest. The moving mirror becomes important, as the total interferogram is obtained by varying the optical path lengths between the two mirrors and recording the signal as a function of these distances. The interference function $I(x)$ is given as the intensity of both recombined beams – a plot of $I(x)$ versus the displacement of the moving mirror x gives the interferogram. Figure 3.4 (b) shows the two monochromatic signals and how they constructively and destructively combine to form the interferogram. If M_2 (the moving mirror) travels at a constant velocity, $I(x)$ is related to the source intensity $B(\omega)$ via:

$$I(x) = 1/2 \int_0^\infty B(\omega) \cos 2\pi\omega dx. \quad (3.42)$$

Here, ω is the frequency. Therefore, $I(x)$ describes the cosine Fourier transform of

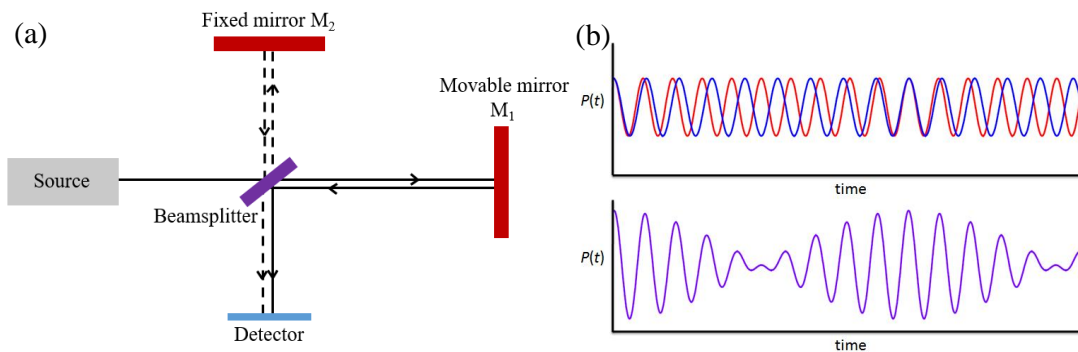


Figure 3.4: (a) Schematic view of a Michelson interferometer. The beamsplitter divides the source beam and sends signals to the movable mirror M_1 and the fixed mirror M_2 . These beams are reflected and brought back together, resulting in an interference pattern at the detector. (b) The combination of two signals yields the interference pattern, which is plotted as power versus time.

$B(\omega)$ – it provides insight on the resulting spectrum. As we previously mentioned, the Fourier transform converts the interferogram into a single channel spectrum. By taking a ratio of the sample to the reference spectrum, the transmittance spectrum is observed.

3.2.2 Bruker IFS 113v Fourier transform infrared spectrometer

The Bruker IFS 113v measures the entire infrared region ($21\text{-}5000\text{ cm}^{-1}$) due to the multiplex advantage and operates under vacuum in order to reduce atmospheric noise. This system is capable of measuring both transmittance and reflectance, although the work presented in this dissertation was carried out in transmittance. This is because magneto-infrared studies – which make up a large majority of this work – must be done in transmittance. This instrument measures the complete far infrared region, which is important to capture metal-containing vibrations. Four main chambers exist in this spectrometer, including the source, interferometer, sample, and detector. These regions are highlighted in Fig. 3.5.

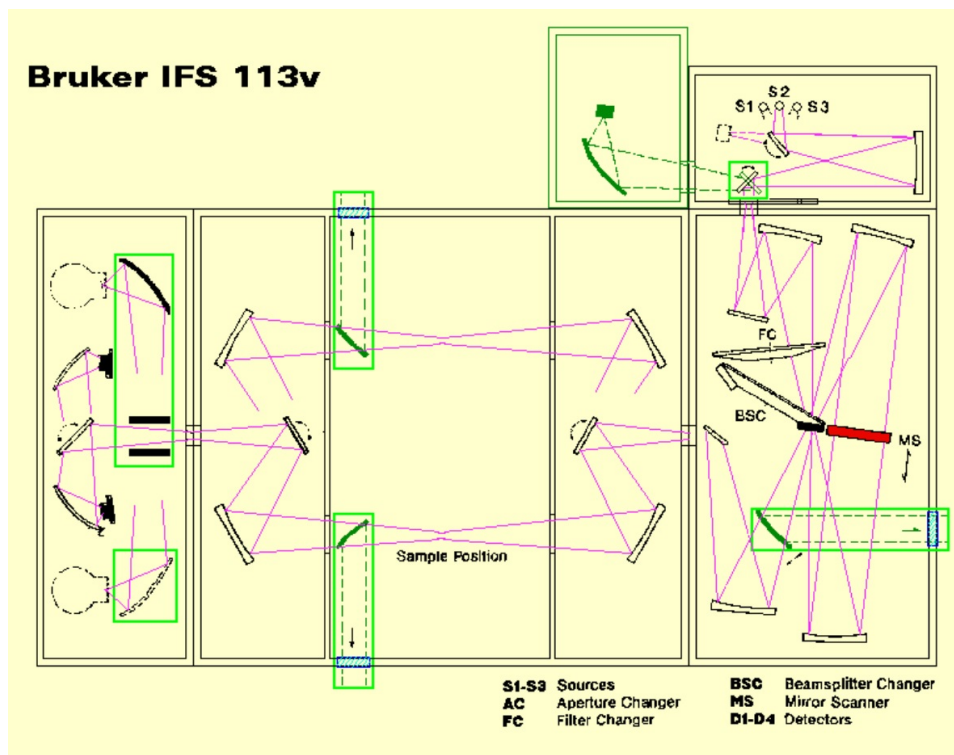


Figure 3.5: Schematic view of the Bruker IFS 113v FTIR spectrometer.

In order to access the full spectroscopic range, multiple sources and beamsplitters are implemented. These are summarized in Table 3.1. The Si and B-doped Si bolometers are cooled with liquid helium in order to provide increased sensitivity. The beamsplitters are mounted on a rotating wheel so that they can be changed without breaking the vacuum. In our lab, they are accessed sequentially – without breaking vacuum or changing alignment.

3.2.3 Bruker Equinox 55 FTIR spectrometer with Bruker IR Scope II

The majority of my middle-infrared measurements were performed on a Bruker Equinox 55 FTIR spectrometer. This instrument has a working range of 600-7,500 cm^{-1} and operates under a nitrogen gas purge. Equipped with a Bruker IR Scope

Table 3.1: Operating parameters for the Bruker IFS 113v.

| Range (cm ⁻¹) | Source | Beam splitter | Opt. Filter | Polarizer | Detector |
|---------------------------|----------|-----------------|-------------|-----------|-------------------------------|
| 10-50 | Hg arc | Mylar 50 μ | Black PE | 1 | Si bolometer, DTGS |
| 30-120 | Hg arc | Mylar 23 μ | Black PE | 1 | Si bolometer, DTGS |
| 50-240 | Hg arc | Mylar 12 μ | Black PE | 1 | Si bolometer, DTGS |
| 100-600 | Hg arc | Mylar 3.5 μ | Black PE | 1 | Si bolometer, DTGS |
| 450-4000 | Globalar | KBr | open | 2 | B-doped Si bolometer, DTGS |

PE = polyethylene. Polarizer 1 = wire grid on oriented PE, Polarizer 2 = wire grid on AgBr

II microscope attachment and a rotating objective nose piece ($\times 4$, $\times 15$, $\times 36$), this system is capable of studying very small samples with high accuracy. The optical pathway is shown in Fig. 3.6. It sports a series of sources, beamsplitters, and detectors, and is capable of measuring in both transmittance and reflectance. The details of the available sources and the energy ranges they probe are listed in Table 3.2.

3.3 Measurements under extreme conditions

3.3.1 Magnetometry

Magnetization is a powerful tool towards the understanding of competing magnetic phases in materials. In this work, we use magnetization to map the phase space of the different competing phases in several molecule-based magnets. In a pulsed-field magnetization setup, current is applied to a compensated coil, inducing magnetic field. The induced voltage can be obtained via Maxwell’s equation (Eqn. 3.7):

$$\nabla \times E = -\frac{dB}{dt}. \tag{3.43}$$

This can be rearranged to give the voltage in a single turn of coil by:

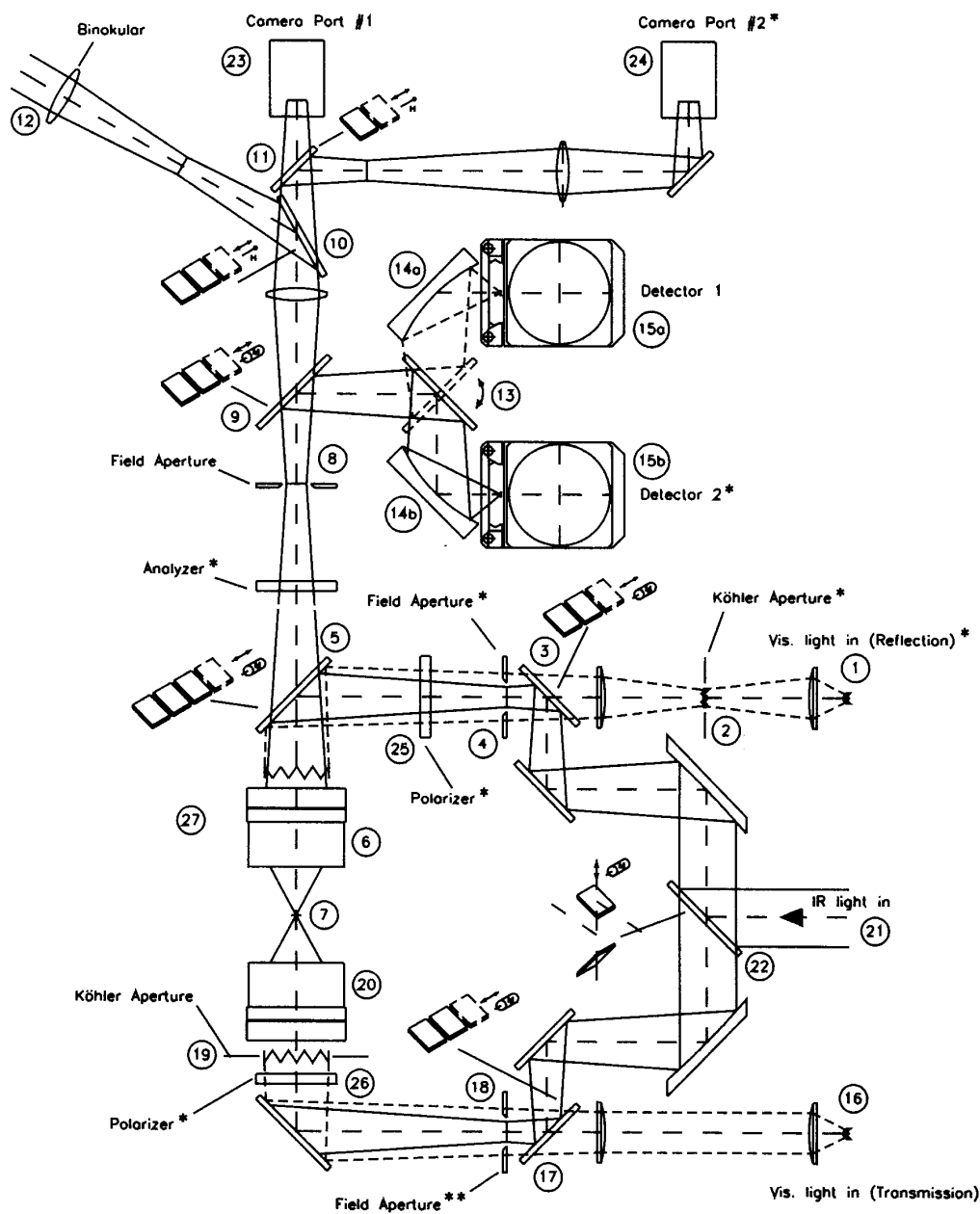


Figure 3.6: Optical path of Bruker IRscope II.

1,16-visible light source; 2,19- visible light aperture; 3,22- motorized switch mirror;
 4,18- optional iris or knife edge aperture; 5,9,10,17- beamsplitter changer; 6-
 objective lens; 7- sample; 8- iris or knife edge aperture; 12- binocular eyepiece; 13-
 two position detector selection mirror; 14- mirror routing to detector; 15- detector;
 20- condenser; 21- IR beam (from spectrometer); 23,24-camera port; 25,26,27-
 polarizer.

Table 3.2: Important parameters of operation for the Bruker IRscope II.

| Range (cm ⁻¹) | Source | Beamsplitter | Detector |
|--------------------------------------|----------|--------------|----------|
| 600-7500 | Globar | KBr | MCT |
| 4000-12000 (near-infrared polarizer) | Tungsten | Quartz | InSb |
| 9000 -17000 (visible polarizer) | Tungsten | Quartz | Si diode |

$$V = \frac{d\phi}{dt} \tag{3.44}$$

where ϕ is the flux, which is the surface integral of B through the coil. Since $B = \mu_0(H+M)$, V contains a contribution of V_M , where

$$V_M \propto \frac{dM}{dt} = \left(\frac{dM}{dH}\right)\left(\frac{dH}{dT}\right). \tag{3.45}$$

In the experiment, dH/dt is given by the pulsed field. Therefore, by integrating V_M , we can obtain M .

3.3.2 Pulsed-field polarization

In this dissertation, we implement pulsed-field polarization techniques as a complement to the spectroscopic work in magnetic field. A pulsed-field polarization measurement involves the simultaneous measurement of the electric polarization as a function of magnetic field. This type of measurement is especially important for materials which exhibit magnetoelectric characteristics, as the coupling between the two is directly probed. This is done on a 65 T short-pulse magnet. In this setup, electric field is measured by immersing the sample in liquid helium – various scenar-

ios of poling can be performed. The sample can be poled from above the ordering temperature down to base temperature (4.2 K) in order to ensure the presence of a single electric domain; if the sample is not susceptible to multiple domains, this step is not necessary. Additionally, electric current can be continuously applied during the magnetic field pulse or not. The electric polarization change $\Delta P(H)$ is measured as the magnetic field is pulsed, producing both the magnetoelectric current and polarization responses of the material up to 65 T.

3.3.3 Spectroscopy under extremes

Spectroscopy is particularly well-suited to explore the properties of materials under extreme conditions, as it is a microscopic technique and is therefore a local probe of lattice changes through phase transitions. This discussion focuses on low temperature, high magnetic field, and high pressure work.

3.3.3.1 Variable temperature spectroscopy

Low temperature experiments were performed with an open-flow cryostat system under high vacuum. For the Bruker IFS 113v, an APD Heli-Tran LT-3-110 model system is implemented. Figure 3.7 summarizes the low-temperature setup.

A helium gas cylinder is used to elevate pressure within a liquid helium dewar and force liquid helium first into a vacuumed transfer line and then into the open flow cryostat. Here, the sample is cooled. Liquid helium evaporates and directed through the transfer line to precool, exiting the system at the shield outlet port. This mechanism keeps the transfer line cool. Temperature is controlled via an internal heater inside the cryostat in combination with the flowmeter. An adjustment knob on the top of the cryostat also allows for control of the helium flow. A heater is installed near the base of the cryostat in order to keep the sample and rubber o-

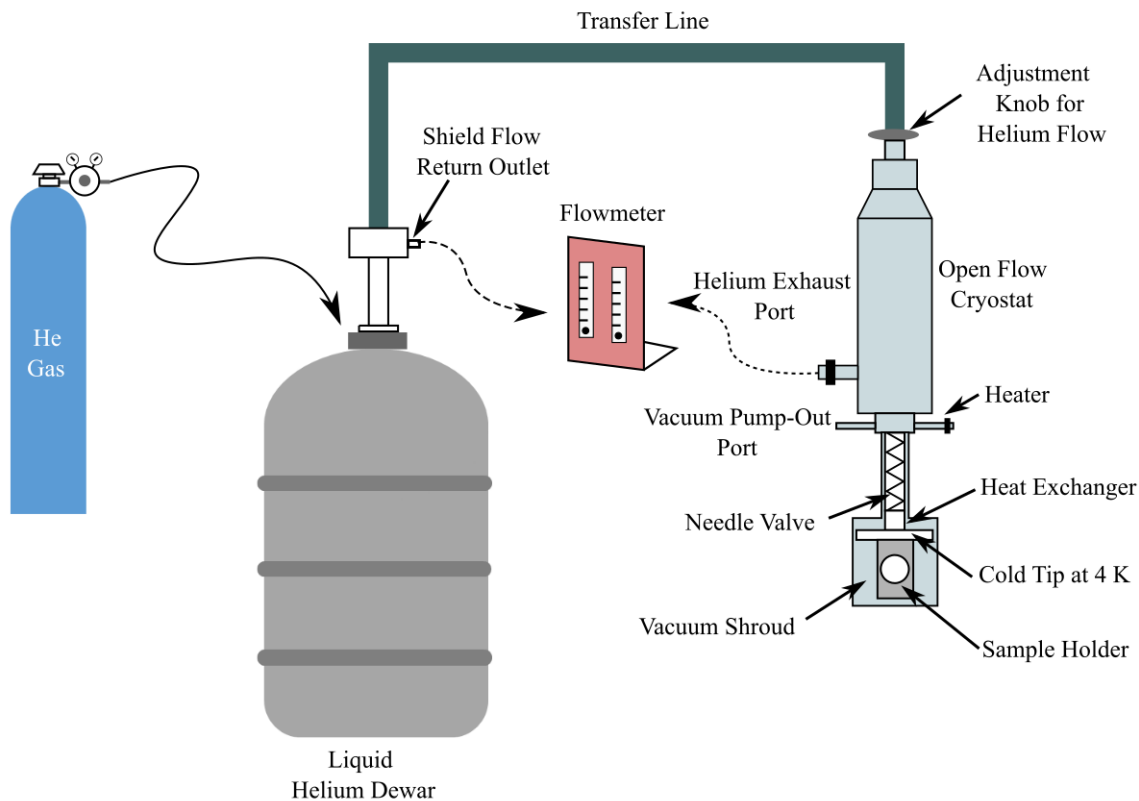


Figure 3.7: Schematic of the LT-3-110 Heli-Tran open flow cryostat in a low-temperature setup.

rings from freezing during the experiment. The sample is mounted on the sample holder which is located at the base of the cryostat – a hole through this apparatus allows for light to pass through. Throughout the experiment, the sample remains under vacuum and light passes through appropriate windows (polyethylene for far-infrared, KBr for middle-infrared). In order to ensure that the sample is truly at the correct temperature, crycon grease is placed between the cryostat and the sample holder. This improves thermal contact. Samples are mounted with various adhesives including, rubber cement, GE varnish, or silver paste. The cryostat end of this setup is shown in Fig. 3.8 (a). It fits nicely into the spectrometer sample chamber or between the objective and the computer-controlled stage.

Cryogenic experiments on the Bruker Equinox 55 are performed with an Oxford

Instruments Microstat He [Fig. 3.8 (b)]. The cooling mechanism for this system differs from that of the Bruker 113V in that the helium is mechanically pumped into the cryostat rather than pushed with helium gas. Figure 3.9 summarizes this setup. Helium flow is controlled with an Oxford gas flow controller and a mechanical pump. The flow controller regulates the amount of helium directed through the transfer line and into the side-loading cryostat. After cooling, helium is recovered through the transfer line. Temperature is controlled with an Oxford Intelligent Temperature Controller ITC 601 – the proportional band (P), integral action time (I), and derivative action time (D) are automatically adjusted. Temperatures lower than 4.2 K are achieved by lowering the pressure in the heat exchanger. The cryostat is designed for optical microscopy, with a side loading design and a short working distance. Measurements are performed under high vacuum in transmittance or reflectance.

3.3.3.2 Magneto-infrared techniques

High magnetic fields are accessed at both the National High Magnetic Field Laboratory (NHMFL) in Tallahassee, FL and Los Alamos, NM. Equipped with dozens of magnets and a variety of measurement techniques, these facilities support the inves-

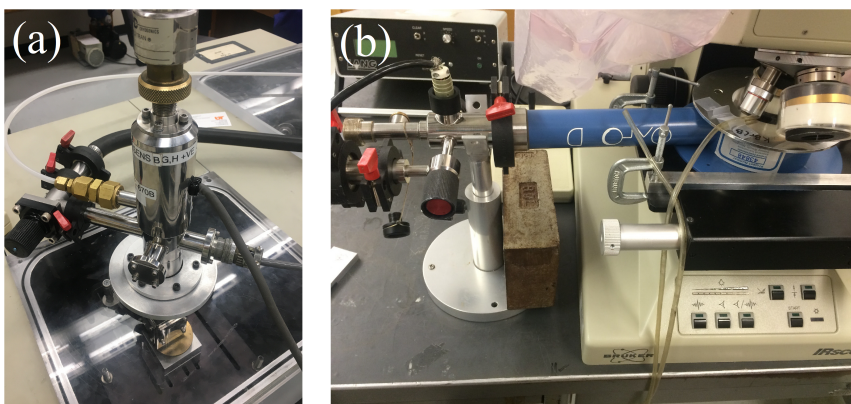


Figure 3.8: Cryostats used for optical measurements on (a) the Bruker 113v and (b) the Bruker Equinox 55 FTIR spectrometer with Bruker IR Scope II attachment.

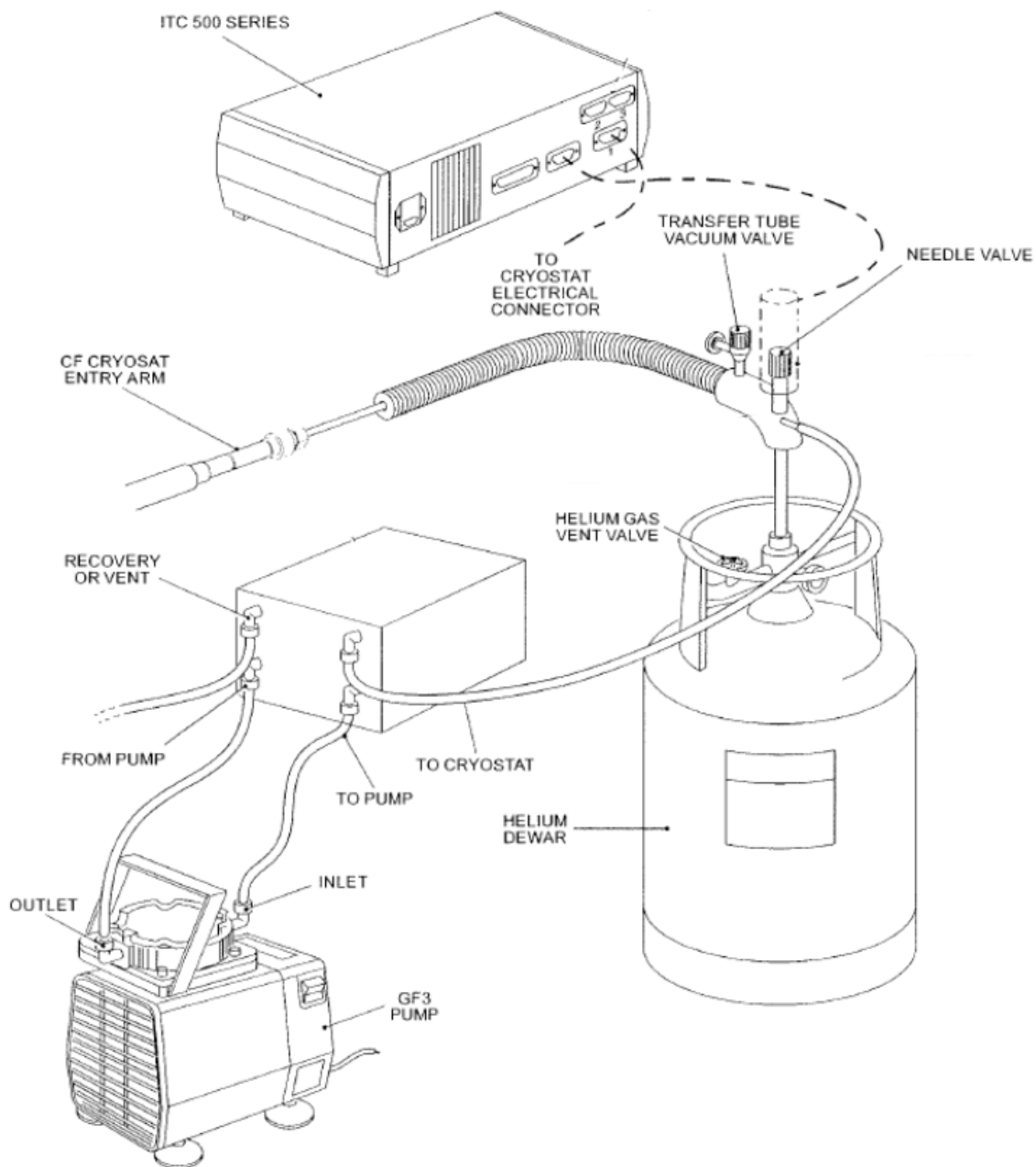


Figure 3.9: Summary of the low-temperature setup for the Bruker Equinox 55.

tigation of interdisciplinary science problems and the development of new magnetic materials.

Figure 3.10 displays a schematic of the magneto-infrared setup. Infrared radiation is emitted from the spectrometer and directed down a pipe via a pair of off-axis parabolic mirrors. The light is directed down the measurement probe, transmitted through the sample, and collected by a bolometer. The bolometer transforms the light into an electric signal which is then amplified, filtered, and returned to the spectrometer. The sample and bolometer, which are both mounted on the probe, are cooled by submerging the measurement probe into a liquid helium bath. A small amount of helium exchange gas within the probe ensures that the sample is at base temperature (4.2 K). The sample is placed directly at field center (35 T). Since no reference beam is measured in the sample probe, we analyze the magneto-infrared response by looking at changes in the absorption difference $\Delta\alpha = \alpha(\omega, B=35 \text{ T}) - (\alpha(\omega, B=0 \text{ T}))$. Single or polycrystalline samples can be measured. Measurements are taken on a Bruker IFS 66v spectrometer.

3.3.3.3 High pressure infrared spectroscopy

High pressures are attained via diamond anvil cell techniques. Figure 3.11 summarizes this measurement. A metal gasket sits between two 5 μm diamond faces. The gasket has a hole drilled in the center (on the order to 200 nm) that houses the sample, pressure medium, and ruby balls, and allows light to pass through the setup. In order to apply pressure, four screws on the cell are turned which brings the diamonds closer together and compresses the sample. Pressures are applied step-wise and allowed to stabilize, meaning that each measurement is taken at a fixed pressure.

Polycrystalline samples are individually loaded into the diamond anvil cell along with a pressure medium in order to ensure that applied pressure is quasi-hydrostatic.

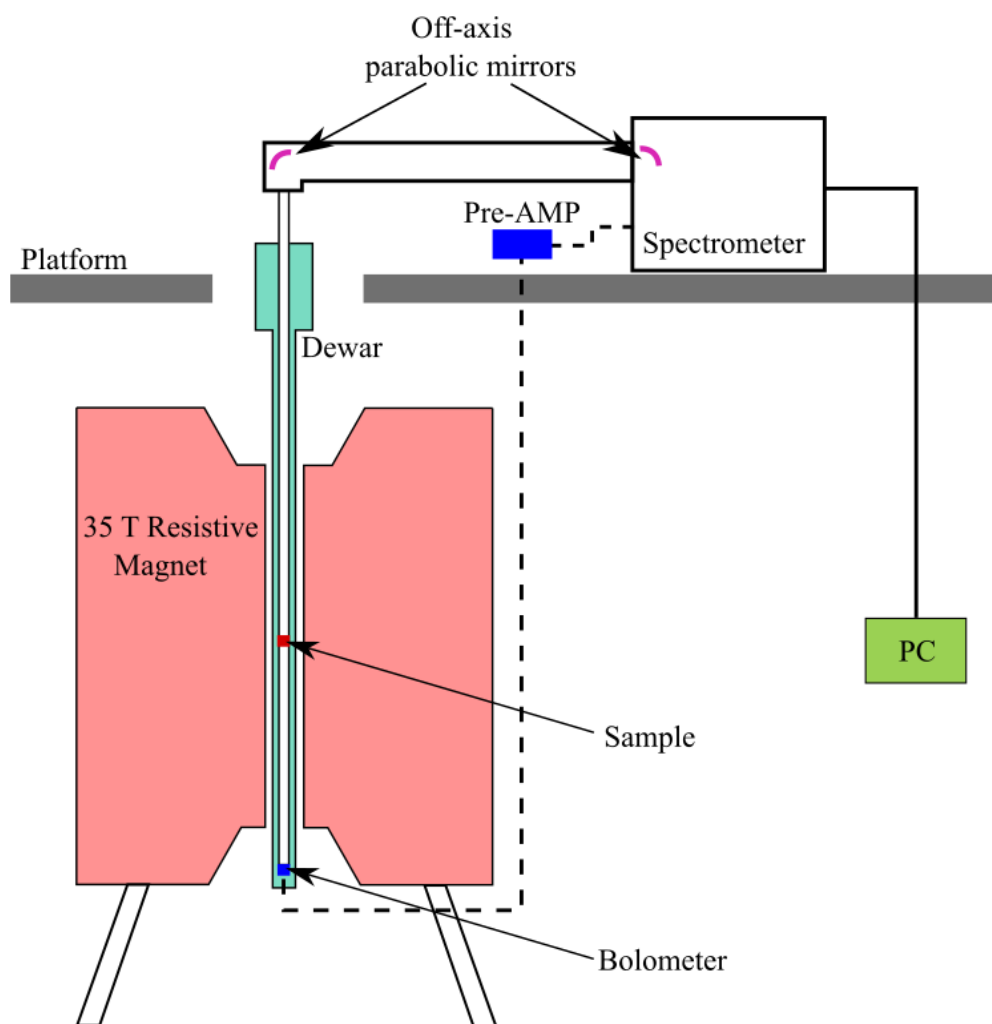


Figure 3.10: Schematic view of the 35 T Resistive Magnet at the National High Magnetic Field Laboratory in Tallahassee, FL.

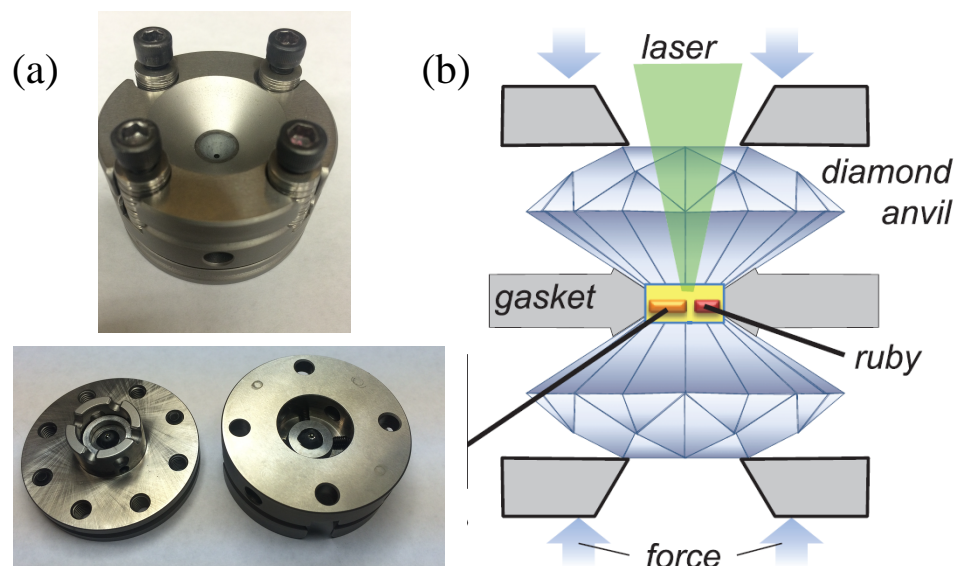


Figure 3.11: (a) Pictures and (b) schematic representation of a diamond anvil cell. [170]

An annealed ruby ball is included in the cell, and fluorescence measurements are taken at each pressure. This is because ruby has a well-known linear dependence between wavelength and pressure. [171] Far infrared measurements ($100\text{-}700\text{ cm}^{-1}$) are taken on a Bruker Hyperion spectrometer with a helium-cooled bolometer detector.

3.4 Materials of interest: sample preparation and complementary calculations

3.4.1 Synthetic procedures

Single and polycrystalline samples of $[(\text{CH}_3)_2\text{NH}_2]M(\text{HCOO})_3$ ($M=\text{Mn}^{2+}, \text{Co}^{2+}, \text{Ni}^{2+}$) were provided by Naresh Dalal from Florida State University. [56] $[\text{Cu}(\text{pyz})_2(2\text{-HOpy})_2](\text{PF}_6)_2$ and $[\text{Cu}(\text{pyz})_{1.5}(4\text{-HOpy})_2](\text{ClO}_4)_2$ were provided by Chris Landee from Clark University – they were grown via conventional solution chemistry techniques [148]. Single crystals of $(\text{NH}_4)_2[\text{FeCl}_5 \cdot (\text{H}_2\text{O})]$

were grown by Wei Tian at Oak Ridge National Laboratory under solvothermal conditions. [61,153]

3.4.2 Magnetometry

Magnetization measurements were carried out at the National High Magnetic Field Laboratory in Los Alamos, NM with the 65 T pulsed-field magnet. This magnet is equipped with a 1.5 mm long, 1500-turn compensated-coil susceptometer constructed from 50 gauge high-purity copper wire. [30,150] The sample probe is placed directly into a liquid helium bath, and the sample – located inside a small, non-magnetic ampoule – sits directly at the center of the field. Single or polycrystalline samples are loaded into a 1.3 mm diameter ampoule that can be moved in and out of the coil and thus the center of magnetic field. By subtracting the empty coil data from that measured with the sample (under identical conditions) an accurate value of M can be obtained. [120] The susceptometer (along with the sample probe) is placed in a ^3He cryostat, providing measurements on temperatures down to 0.32 K. The de Haas-van Alphen effect of copper in the coils of the susceptometer calibrates the field to one part in 1000. [150] Fields up to 65 T are driven with a capacitor bank. A Quantum Design PPMS was used to benchmark magnetic moments.

3.4.3 Pulsed-field polarization

Pulsed-field polarization measurements were performed on the 65 T pulsed-field magnet at the National High Magnetic Field Laboratory in Los Alamos, NM. Two silver leads are attached to the sample on parallel faces; polarization is measured along the axis perpendicular to these faces. The crystals are attached to the probe with a small amount of vacuum grease. The probe is then immersed into a liquid helium bath, where the samples are aligned to sit directly at the center of magnetic field.

Electric field was measured in a two step process by (i) poling – applying an electric field $E = -100$ V at $B = 0$ T through T_N down to base temperature – and then (ii) applying the same voltage as the magnetic field was pulsed. This process ensured that a single electric domain was maintained throughout the pulse. In particular, we measured various configurations of P and B . Temperature is controlled with a heater near the sample space.

3.4.4 Infrared transmittance measurements

In order to perform infrared transmittance measurements, we mixed single crystals with paraffin for the far infrared region and KBr middle infrared region. The advantage of this technique is the ability to control optical density. Different concentrations of pellets were employed in order to capture each feature. Grain sizes in most cases were on the order of $10\ \mu\text{m}$. Absorption was calculated from transmittance measurements as $\alpha(\omega) = -\frac{1}{hd}\ln[T(\omega)]$, where $T(\omega)$ is the measured transmittance, h is the concentration, and d is the thickness. Temperature ramp rates were generally on the order of $0.2 - 1$ K/min. Spectral resolutions of $0.5-2\ \text{cm}^{-1}$ were employed depending on the measurement. [120]

3.4.5 Magneto-infrared experiments

Magneto-infrared measurements were performed at the National High Magnetic Field Laboratory in Tallahassee, FL at 4.2 K using the 35 T resistive magnet. In this setup, there is no single beam reference – we can only obtain the response of the material as a function of applied magnetic field. Therefore, in order to emphasize small spectral changes with field, we calculate absorption differences as $\Delta\alpha = \alpha(\omega, B) - \alpha(\omega = 0)$. From these spectra, we can quantify effects for specific phonons via an integration of the absolute value of $\Delta\alpha$ over a small energy window and plotting these differences vs

magnetic field. [120] In this way, we develop trends that follow field-induced frequency shifts with much less noise and error. However in $[\text{Cu}(\text{pyz})_2(2\text{-HOpy})_2](\text{PF}_6)_2$ and $[\text{Cu}(\text{pyz})_{1.5}(4\text{-HOpy})_2](\text{ClO}_4)_2$, field-induced changes turned out to be much larger than in the $[(\text{CH}_3)_2\text{NH}_2]M(\text{HCOO})_3$ ($M=\text{Mn}^{2+}, \text{Co}^{2+}, \text{Ni}^{2+}$) family along with some of the modes in $(\text{NH}_4)_2[\text{FeCl}_5 \cdot (\text{H}_2\text{O})]$ – we were able to track frequency shifts $\Delta\omega$ directly because of the excellent signal to noise ratios. [120]

3.4.6 Lattice dynamics calculations

Structural relaxations, energies, and lattice dynamics calculations were performed on $[(\text{CH}_3)_2\text{NH}_2]\text{Mn}(\text{HCOO})_3$ using density functional theory (DFT) plus the on-site repulsion (U) method [172, 173] as implemented in VASP [174, 175] to reveal structures in different magnetic states as well as mode assignments and displacement patterns. The on-site (U) and nearest neighbor repulsion (V) are set to standard values of 4 and 1 eV for Mn, respectively. The electron-ion interactions were treated using the projected augmented wave method [83, 176, 177].

Chapter 4

Phonon mode links ferroicities in multiferroic



In this chapter, I discuss the combination of magneto-infrared spectroscopy, magnetization, and lattice dynamics calculations to explore the phase transitions in multiferroic $[(\text{CH}_3)_2\text{NH}_2]\text{Mn}(\text{HCOO})_3$. Both the 185 K ferroelectric transition and the magnetically-driven transition to the fully saturated state at 15.3 T involve the formate bending mode, direct evidence of a common connection between the two types of ferroicities and for how lattice distortions promote high temperature magnetoelectric coupling in this system.

4.1 Understanding the lattice dynamics of $[(\text{CH}_3)_2\text{NH}_2]\text{Mn}(\text{HCOO})_3$ as a function of temperature

Figure 4.1 (a) displays the infrared response of $[(\text{CH}_3)_2\text{NH}_2]\text{Mn}(\text{HCOO})_3$ at 300 K. We assign the spectral features via comparison with chemically similar materials and complementary dynamics calculations [29, 122, 178, 179]. Localized counterion and ligand modes resonate above 600 cm^{-1} and more collective, manganese-related features appear below 300 cm^{-1} . Table 4.1 summarizes the behavior of several key modes. The 794 cm^{-1} peak, assigned here as a formate bend, is of special importance because, as we shall see, it underlies the development of both polarization and magnetic saturation.

Figure 4.1 (b) displays a close-up view of the 794 cm^{-1} formate bending mode. This feature breaks into a strong doublet across the 185 K order-disorder transition due to the formation of two different types of hydrogen bonds between $(\text{CH}_3)_2\text{NH}_2^+$ and the formate ligands. The splitting is 6 cm^{-1} - large for an order-disorder ferroelectric. Additional fine structure due to the development of three unique Mn-O-C-O-Mn superexchange pathways at low temperature might be anticipated but is not resolved in $[(\text{CH}_3)_2\text{NH}_2]\text{Mn}(\text{HCOO})_3$ due to bond length similarities [178].

Table 4.1: Frequencies and assignments for important modes in $[(\text{CH}_3)_2\text{NH}_2]\text{Mn}(\text{HCOO})_3$ at 300 and 4 K.

| Mode Assignments | ω 300 K (cm^{-1}) | ω 4 K (cm^{-1}) |
|-------------------------|-------------------------------------|-----------------------------------|
| $\nu(\text{Mn-O}_{eq})$ | 292 | 296 |
| $\delta(\text{HCOO}^-)$ | 794 | 794, 800 |
| $\rho(\text{NH}_2)$ | 891 | 930 |
| $\nu_{as}(\text{CNC})$ | 1025 | 1030 |
| $\delta(\text{NH}_2)$ | 1632 | 1644 |

ν =symmetric stretching, ν_{as} =asymmetric stretching, ρ =rocking, δ =bending

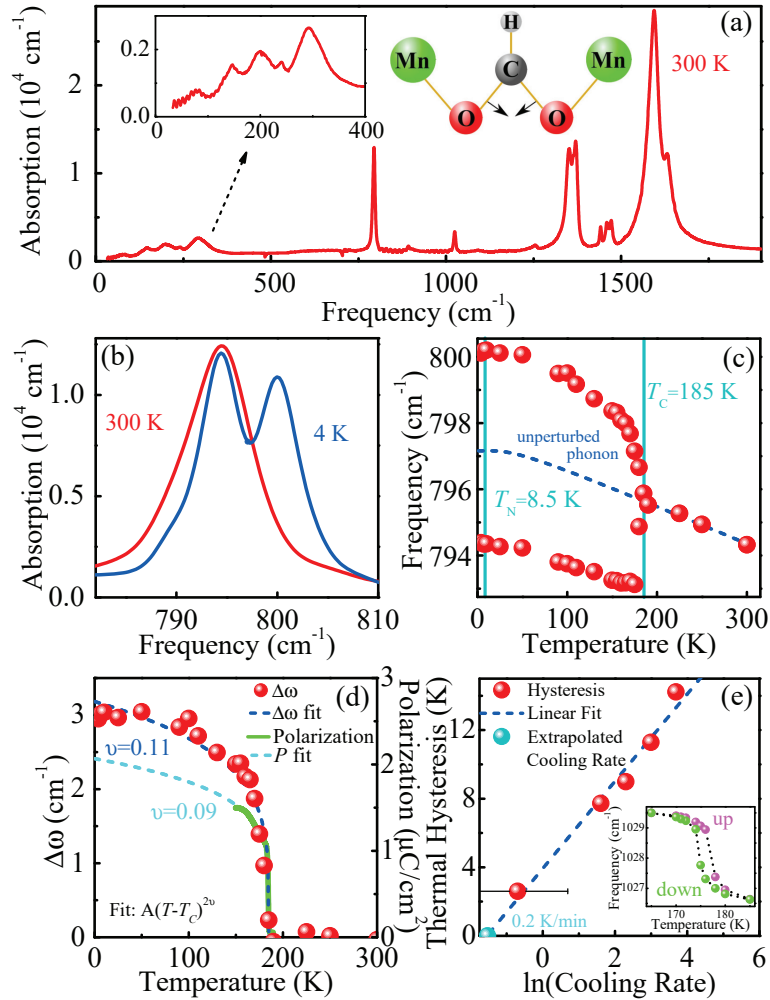


Figure 4.1: (a) Infrared response of $[(\text{CH}_3)_2\text{NH}_2]\text{Mn}(\text{HCOO})_3$ at room temperature and displacement pattern of formate bending mode. Inset: low frequency region of the spectra which has mostly Mn-containing modes. (b) Close-up view of the infrared-active formate bending mode. (c) Frequency versus temperature plot that reveals doublet splitting of the formate bending mode across T_C . An anharmonic fit of the high temperature data points reveals the behavior of the unperturbed phonon. Error bars are on the order of the symbol size. (d) Splitting of the formate bending mode vs. temperature, a power law fit to this data, and polarization from Ref. Wang2013. (e) Width of the hysteresis around T_C vs. cooling rate. The loop closes when the cooling rate is $< \approx 0.2 \text{ K/min}$. Inset: hysteresis of the C-N-C asymmetric bending mode at 0.5 K/min.

Figure 4.1 (c) tracks peak position versus temperature. A fit to the data above T_C characterizes traditional anharmonic effects. The anharmonic fit of the high-temperature data points follows the form $\omega = \omega_0 + C[1 + 2/e^{0.144\omega_0/T} - 1]$ where ω_0 is 797.8 cm^{-1} and C is -0.6538 . Below T_C , the fit represents the unperturbed phonon response (i.e. what would be expected in the absence of the transition). Figure 4.1 (d) displays the splitting of the formate bending mode plotted as a difference between the high frequency branch and the aforementioned anharmonic fit. The experimental polarization from Ref. 37 is included as well. The coincidence of the two data sets demonstrates that the doublet splitting of the formate bending mode functions as an order parameter for the ferroelectric transition. A power law fit of the form $A(T_C - T)^{2\nu}$ reveals a critical exponent (ν) of 0.11 - clearly different from mean field behavior (0.25) and suggestive of a quasi-two-dimensional system [180]. The latter may lead to interesting applications in layered microelectronics. A ν of 0.11 is also in reasonable agreement with that obtained from fits to the polarization. The latter has more points around T_C and fewer at low temperature [37]. As shown in Fig. 4.1 (e), the hysteresis around the ferroelectric transition closes with decreasing sweep rate.

4.2 Spin-lattice coupling across the magnetically-driven transition in $[(\text{CH}_3)_2\text{NH}_2]\text{Mn}(\text{HCOO})_3$

We now turn to the spectroscopic response across the magnetically-driven transition. Figure 4.2 (a) displays a close-up view of the absorption of $[(\text{CH}_3)_2\text{NH}_2]\text{Mn}(\text{HCOO})_3$ near the formate bending mode along with the absorption difference spectra, $\Delta\alpha(\omega, B) = \alpha(\omega, B = 35 \text{ T}) - \alpha(\omega, B = 0 \text{ T})$. Changes are on the order of 3% at full field. Figure 4.2 (b) illustrates the development of the absorption difference with

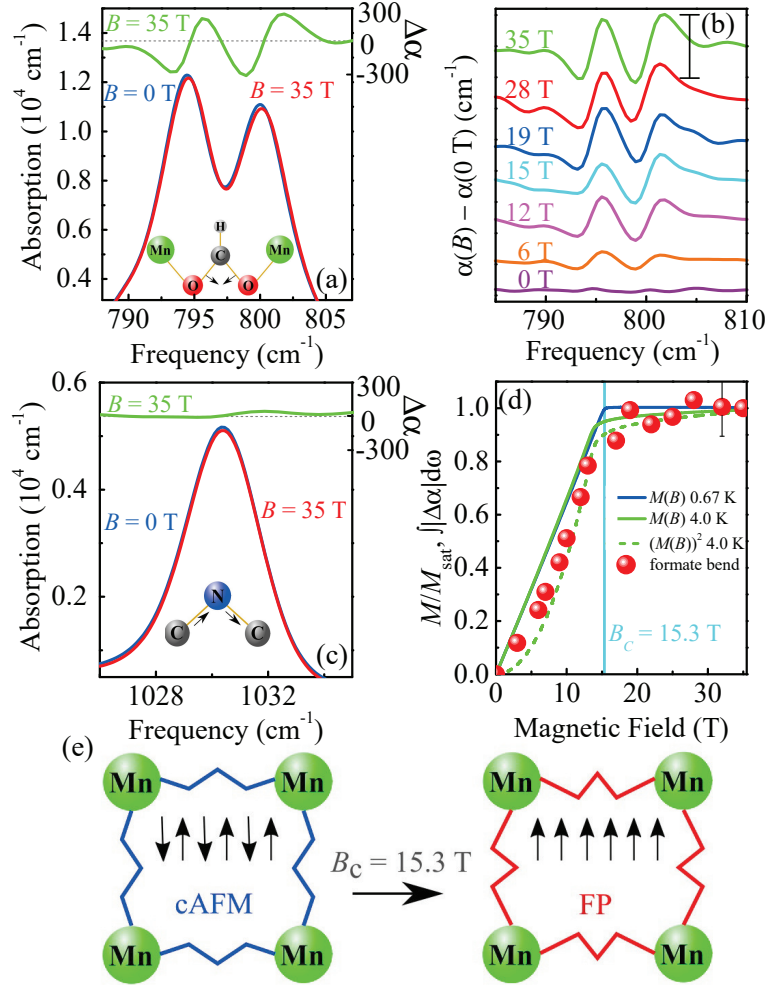


Figure 4.2: (a) Close-up view of the absolute absorption spectrum focusing on the formate bending mode (displacement shown in schematic) at 0 and 35 T at 4.2 K along with the full field absorption difference spectrum. (b) Absorption difference spectra, $\Delta\alpha = \alpha(\omega, B) - \alpha(\omega, B = 0)$, showing field-induced changes in the formate bending mode for fields up to 35 T. The scale bar is 500 cm^{-1} . (c) Absorption spectrum of the 1030 cm^{-1} amine stretching mode at 0 T and 35 T along with the full field absorption difference spectrum, revealing the lack of field dependence in the couterion mode. (d) Normalized magnetization [30], square of the magnetization, and integrated absorption difference as functions of applied field. (e) Schematic of the field-induced local lattice distortion of the formate ligand.

increasing magnetic field. Clear features are apparent even when the field is small. They grow with increasing field and saturate near $B_C = 15.3$ T. The derivative-like shape of $\Delta\alpha$ is consistent with a field-induced hardening of the underlying doublet. Importantly, only one phonon - the relatively soft formate (O-C-O) bending mode - changes in field. Recent calculations reveal that there is significant spin density on the oxygen centers of the formate ligands (and on Mn) [30], making this portion of the framework a logical candidate for spin-lattice coupling. There are no other field-induced local lattice distortions within our sensitivity. This includes the amine-related displacements as evidenced by the spectra in Fig. 4.2 (c) where the C-N-C asymmetric stretch is rigid. We therefore conclude that dimethylammonium plays no role in the magnetically-driven transition at B_C . This is consistent with the lack of spin density on the counterion [30].

To quantify these effects, we integrate the absolute value of the field-induced absorption difference over a small energy window ($\int |\alpha(B) - \alpha(0)| d\omega$) and plot these values - along with magnetization [30] and the square of the magnetization - as a function of applied field. By so doing, we generate a function that is proportional to the frequency shift but with significantly smaller error bars. We tested this method in prior work on $[\text{Ru}_2(\text{O}_2\text{CMe})_4]_3[\text{Cr}(\text{CN})_6]$. As shown in Fig. 4.2 (d), changes in the formate bending mode track $[M(B)]^2$ [112]. This is because molecular vibrations follow an even function whereas magnetism is an odd function. The feature grows with increasing field and plateaus above 15.3 T, an indication that the lattice is sensitive to the microscopic nature of the spin state. Similar trends are seen in other molecule-based magnets like $\text{Mn}[\text{N}(\text{CN})_2]_2$ [29]. It is well known that phonons respond to spin correlations as $\Delta\omega = \lambda\langle S_i \cdot S_j \rangle$ where λ is the spin-phonon coupling constant and $\langle S_i \cdot S_j \rangle$ is the nearest-neighbor spin-spin correlation function [181]. Based on the field-induced frequency shift (on the order of 0.1 cm^{-1}) and the limiting low

temperature value of $\langle S_i \cdot S_j \rangle \approx S^2 = (5/2)^2$, we estimate $\lambda \leq 0.1 \text{ cm}^{-1}$ - a natural consequence of the low energy scales in this system.

The involvement of the formate bending mode in the magnetically-driven transition to the fully saturated state is striking because the same mode is sensitive to the development of the ferroelectric polarization. This observation suggests that the lattice may be connected with high temperature magnetoelectric coupling [37,38]. The key to unraveling this puzzle is to recall that formate is the superexchange ligand. Interactions between Mn^{2+} centers thus take place via $\text{Mn} \cdots \text{formate} \cdots \text{Mn}$ exchange pathways (Fig. 2.13). Distortions of the superexchange pathway modify orbital overlap and therefore reduce J_{AFM} . This is because $J_{\text{AFM}} \sim -4t^2/U$, where t is the overlap integral ($\int \phi_1 H \phi_j d\tau$). Reduction of J_{AFM} allows the fully polarized magnetic state to emerge at $B_C = 15.3 \text{ T}$, somewhat lower than that expected from the zero field exchange energy.

Based on field-induced hardening of the formate bending mode and the Goodenough-Kanamori-Anderson rules stating a tendency toward a 90° superexchange angle in the ferromagnetic state [85], our data suggest that the O-C-O angle of the formate ligand decreases with increasing field, saturating only upon entry into the fully polarized state. We tested this supposition with density functional calculations, optimizing the structure in the antiferromagnetic and ferromagnetic states. Our calculations confirm that the O-C-O bond angles in the ferromagnetic state are smaller than those in the antiferromagnetic state. Moreover, our calculations show that O displacement dominates this angular distortion - not C displacement. The greatest change in bond angle is 0.026° (from 123.635° in the antiferromagnetic state to 123.609° in the ferromagnetic state). Note that there are several different O-C-O angles in the system due to the low symmetry. This is shown schematically in Fig. 4.2(e). By way of comparison, a 1° out-of-plane bend in $[\text{Cu}(\text{HF}_2)(\text{pyz})_2]\text{BF}_4$ is

predicted to modify J_{AFM} by $\simeq 3\%$ [114].

$[(\text{CH}_3)_2\text{NH}_2]\text{Mn}(\text{HCOO})_3$ is well-suited to an analysis of structure-property relations. The molecular aspects of the metal-organic framework allows for synthetic variation, and the perovskite-like crystal structure makes this material topologically similar to the rare earth manganites. The latter have attracted sustained attention for their incredibly complex P - T - B phase diagrams that sport multiple competing phases. In HoMnO_3 , an applied magnetic field drives through five unique magnetic phases at 3 K before saturation [65]. By comparison, $[(\text{CH}_3)_2\text{NH}_2]\text{Mn}(\text{HCOO})_3$ displays a strikingly simple B - T phase diagram [Fig. 2.15] in which magnetic field induces only a spin flop before magnetization saturates at 15.3 T [30]. This simplicity allows each transition to be isolated and explored in a straightforward manner. $[(\text{CH}_3)_2\text{NH}_2]\text{Mn}(\text{HCOO})_3$ also behaves like a molecular material in that only one vibrational mode is sensitive to the change in the microscopic spin pattern [29, 114]. This is quite different than what is observed in the multiferroic manganites, for instance DyMn_2O_5 , where the majority of phonon modes reveal a strong field dependence predominately associated with local distortions of the distorted octahedra and square pyramids [156]. The same is true in $\text{Sr}_{1-x}\text{Ba}_x\text{MnO}_3$ where the large phonon changes at the ferroelectric and magnetic ordering transitions are characteristic of a displacive (rather than order-disorder) ferroelectric [182]. The behavior of the formate bending mode in $[(\text{CH}_3)_2\text{NH}_2]\text{Mn}(\text{HCOO})_3$ is also quite different from an electromagnon which, although sensitive to the development of both electric and magnetic order in rare earth manganites [183, 184], is a collective (rather than elementary) excitation that naturally involves both spin and charge.

Chapter 5

Structure-property relations in multiferroic

$[(\text{CH}_3)_2\text{NH}_2]M(\text{HCOO})_3$ ($M = \text{Mn},$ **Co, Ni**)

In this chapter, we bring together magnetization, infrared spectroscopy, and lattice dynamics calculations to uncover the magnetic field - temperature ($B - T$) phase diagrams and vibrational properties of the $[(\text{CH}_3)_2\text{NH}_2]M(\text{HCOO})_3$ ($M = \text{Mn}^{2+}, \text{Co}^{2+}, \text{Ni}^{2+}$) family of multiferroics. While the magnetically-driven transition to the fully saturated state in $[(\text{CH}_3)_2\text{NH}_2]\text{Mn}(\text{HCOO})_3$ takes place at 15.3 T, substitution with Ni or Co drives the critical fields up toward 100 T - an unexpectedly high energy scale for these compounds. Analysis of the infrared spectrum of the Mn and Ni compounds across T_C reveals doublet splitting of the formate bending mode which functions as an order parameter of the ferroelectric transition. By contrast, $[(\text{CH}_3)_2\text{NH}_2]\text{Co}(\text{HCOO})_3$ reveals a surprising framework rigidity across the

order/disorder transition due to modest distortions around the Co^{2+} centers. The transition to the ferroelectric state is thus driven solely by counterion freezing and the resulting hydrogen bonding. Under applied field, the Mn (and most likely, the Ni) compounds engage the formate bending mode to facilitate the transition to their fully saturated magnetic states, whereas the Co complex adopts a different mechanism involving formate stretching distortions to lower the overall magnetic energy. Similar structure-property relations involving substitution of transition metal centers and control of the flexible molecular architecture are likely to exist in other molecule-based multiferroics. [120]

5.1 Developing magnetic field-temperature phase diagrams

Figure 5.1 (a-c) displays the pulsed field magnetization for the $[(\text{CH}_3)_2\text{NH}_2]M(\text{HCOO})_3$ ($M = \text{Mn}^{2+}, \text{Co}^{2+}, \text{Ni}^{2+}$) family of materials. This data was benchmarked with a vibrating sample magnetometer. The Mn system sports a 0.31 T spin flop transition, and the magnetization rises linearly until it saturates at 15.3 T. [30] This value of B_C is consistent with $J = 0.64$ K [30, 56, 126]; materials with such low magnetic energy scales can be fully polarized by moderate laboratory fields. The critical field for saturation is a sharply defined feature in the magnetization at 0.4 K that broadens as the temperature approaches T_N . Above $T_N = 8.5$ K, there is no evidence for the spin flop, and the approach to saturation is much more gradual, both consequences of fluctuating regions of short-range order as opposed to the long-range order that occurs at low temperatures. [82]

The distinctive high-field behavior of multiferroic $[(\text{CH}_3)_2\text{NH}_2]\text{Mn}(\text{HCOO})_3$ – discussed in detail in Section 2.5.1 – motivated our extension to the Co and Ni

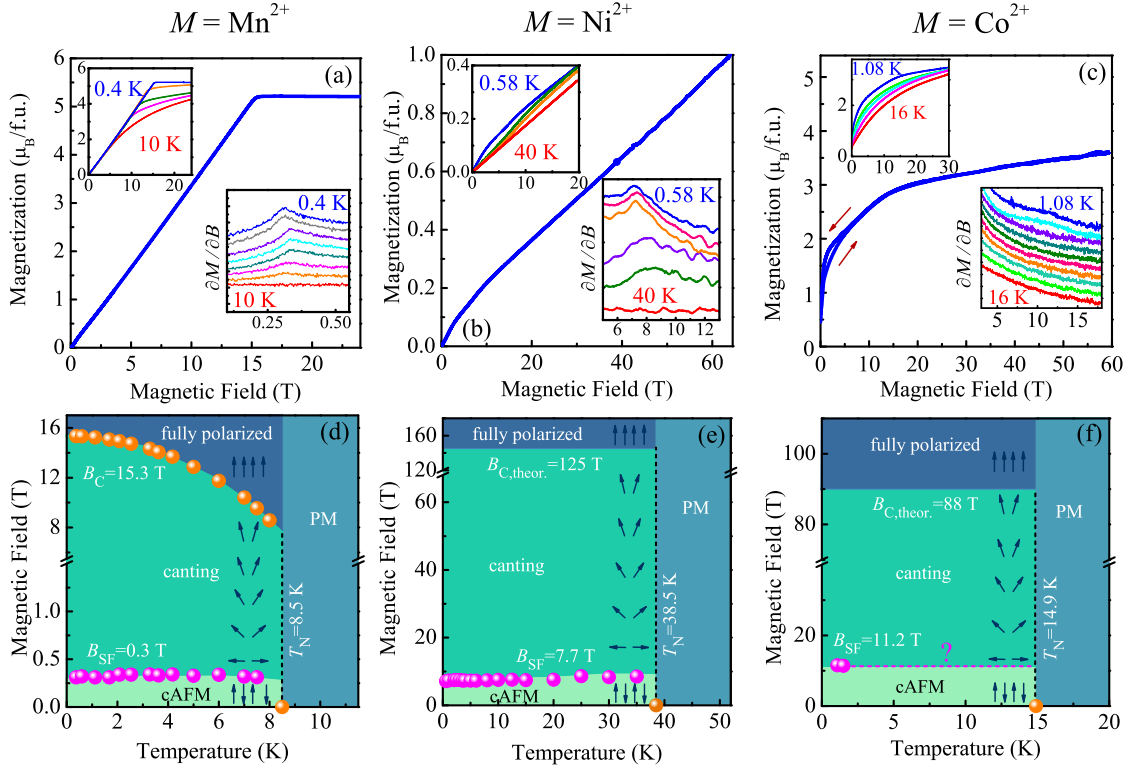


Figure 5.1: (a-c) Pulsed field magnetization of $[(\text{CH}_3)_2\text{NH}_2]M(\text{HCOO})_3$ ($M = \text{Mn}^{2+}$, Co^{2+} , Ni^{2+}) up to 65 T at different temperatures. Derivatives of this data reveal B_{SF} as shown in the lower insets. Only the Mn compound has a clear saturation field under these conditions. [30] The Ni and Co systems are not saturated even at 65 T. (d-f) Magnetic field-temperature phase diagrams developed from the pulsed field magnetization data. Orange points follow the transition to the fully saturated magnetic state, and pink points track the spin flop. The high field phase boundaries for the Ni and Co compounds are estimated as described in the text. Error bars are on the order of the symbol size. cAFM = canted antiferromagnet and PM = high temperature paramagnetic state. [120]

analogs. [30, 41, 90] Just as in $[(\text{CH}_3)_2\text{NH}_2]\text{Mn}(\text{HCOO})_3$, the Ni and Co systems display spin-flop transitions, but at higher fields of 7.7 and 11.2 T, respectively [insets, Fig. 5.1 (b-c)]. The signature of the spin flop in the Co system is subtle and is only seen in the magnetization at the lowest temperatures. We also searched for the saturation field B_C in the Ni and Co compounds; however, even 65 T fails to saturate the magnetization of these materials [Fig. 5.1 (b,c)]. Simple metal site substitution therefore alters the overall energy scales significantly.

In order to generate magnetic field-temperature phase diagrams for these materials, we tracked B_{SF} and, where feasible, B_C as a function of temperature. First derivatives, $\partial M/\partial B$, were used to better highlight the positions of the features in $M(B)$. [30] Figure 5.1 (d-f) summarizes our results. The behavior of the Mn analog is representative of a classic antiferromagnet, where magnetic field drives the system across a low-field spin-flop transition and into the fully saturated magnetic state at 15.3 T. [29, 30] The magnetic field-temperature phase diagrams for the Ni and Co complexes reveal a similar story albeit with higher energy scales. The latter is evident in both the size of B_{SF} and the fact that 65 T does not saturate the magnetization. At higher temperatures, the broadened Co feature is too subtle to track within the noise level. We can estimate the saturation fields for the Co and Ni compounds by equating the total exchange energies from Table 2.3 to the total Zeeman energy via the Hamiltonian $H = -zJ \sum S_i \cdot S_j - g\mu_B B_C \sum S_i^z$ ($z=6$, $g=2.0$, $S = 1$ for Ni and $S = \frac{3}{2}$ for Co). [124] We find $B_{C,\text{Ni}}=125$ T and $B_{C,\text{Co}}=88$ T for the Ni and Co analogs, respectively. Alternatively, we can estimate B_C by extrapolating the linear character of $M(B)$ until it reaches magnetic saturation (defined by $g\mu_B S$) or by extrapolating the derivative of the magnetization curve down to the magnetic field axis. The critical fields obtained from this approach are in reasonable agreement with those estimated above ($B_{C,\text{Ni}}=135$ T, $B_{C,\text{Co}}=90$ T), validating the J values displayed in Table 2.3

and revealing that a spin-only approximation is reliable in these materials - at least within our error bars. These fields are significantly higher than the 15.3 T required to saturate the Mn complex. The energy scales generally follow trends in T_N as well. We therefore see that while metal substitution does not alter the overall space group of the material, there are significant local lattice distortions around the metal centers that modify superexchange interactions and magnetic energy scales. [85] These site-symmetry differences are discussed below. Similar energy scale effects can be seen in other materials like $M[\text{N}(\text{CN})_2]_2$ ($M=\text{Mn}, \text{Co}$). [29, 113]

5.2 Vibrational properties of this family of hybrid organic-inorganic perovskites across the ferroelectric transition

The vibrational properties of $[(\text{CH}_3)_2\text{NH}_2]\text{Mn}(\text{HCOO})_3$ are complex - just like many other molecule-based multiferroics - and have been the subject of numerous investigations. [122, 129, 179, 185–189] Group theory predicts 32 infrared-active modes with both A_{2u} and E_u symmetries. Despite the large number of modes, only a few are useful for revealing changes at the ferroelectric transition or across the critical fields.

Figure 5.2 (a-c) summarizes the behavior of two important vibrational modes of the $[(\text{CH}_3)_2\text{NH}_2]M(\text{HCOO})_3$ ($M = \text{Mn}^{2+}, \text{Co}^{2+}, \text{Ni}^{2+}$) family of materials. Here, we focus on the symmetric formate bending mode near 800 cm^{-1} and the asymmetric C-N-C counterion stretch near 1030 cm^{-1} . The former links the electronic and magnetic ferroicities in the Mn complex [83] whereas the latter is quite sensitive to amine hydrogen bonding and hysteresis effects. Peak position vs. temperature plots [Fig. 5.2 (d-f)] demonstrate strong similarities between the Mn and Ni complexes and, at the same time, uncover distinct behavior in the Co compound.

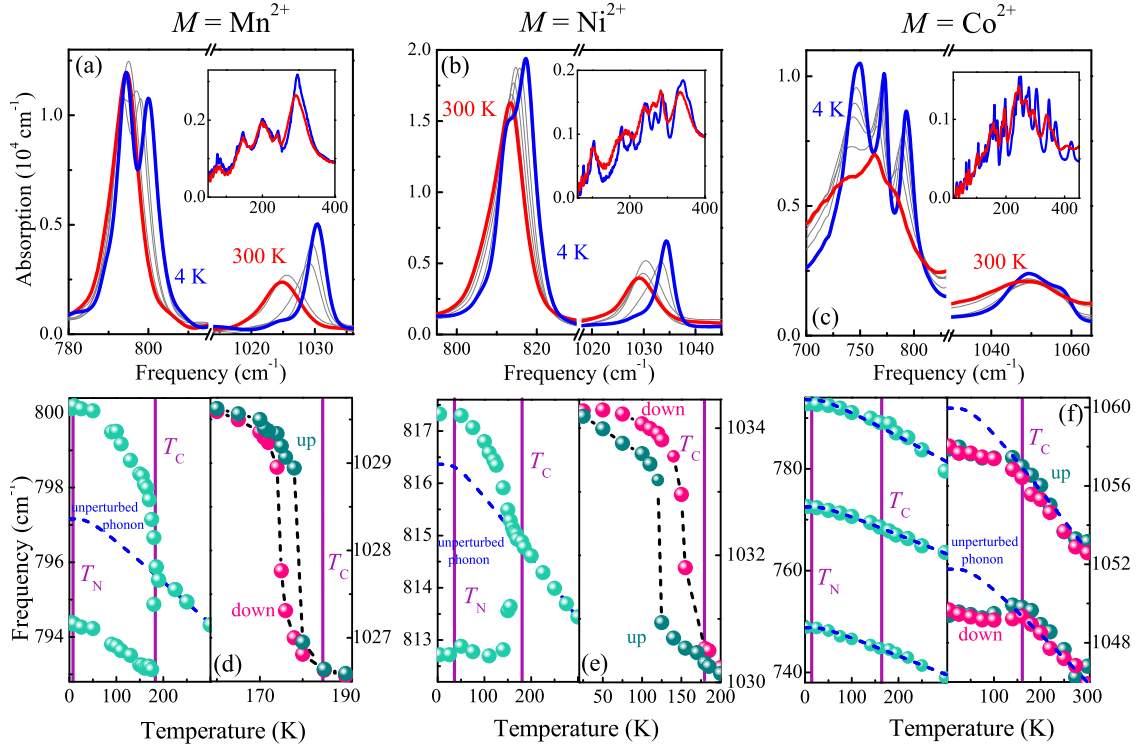


Figure 5.2: (a-c) Close-up views of the formate bending mode (left) and C-N-C stretch (right) for the Mn, Ni, and Co analogs as a function of temperature. Insets show low frequency modes. (d-f) Frequency vs. temperature plots for these features, highlighting the difference in behavior of the Mn and Ni complexes versus the Co system. T_C and T_N are indicated by purple vertical lines. The fit to the high temperature phase data described in the text represents the behavior of the hypothetical unperturbed phonons below T_C . [120]

Doublet splitting of the formate bending modes across T_C is one of the most interesting signatures of the ferroelectric transition in the Mn [30] and Ni analogs. This distortion is due to the development of two unique N-H \cdots O hydrogen-bonded pathways between the counterion and the framework. [83] At base temperature, splitting in the Mn (5.7 cm^{-1}) and Ni (3.9 cm^{-1}) complexes are similar. We fit temperature trends in the paraelectric state as $\omega = \omega_0 + \Delta(T)$, where $\Delta(T) = C[1 + \frac{2}{e^x - 1}]$ with $x = \hbar\omega_0/2k_B T$. Here, ω_0 is the unperturbed phonon frequency at base temperature, \hbar is the reduced Plank's constant, and k_B is Boltzmann's constant. This fit quantifies anharmonicity in the high temperature state, and by extending it into the ferroelectric phase, we reveal how the formate bending mode would have behaved in the absence of the transition. As discussed below, doublet splitting of this mode acts as an order parameter for the ferroelectric transition in the Mn and Ni materials. [120]

Figure 5.3 (a) shows a comparison of the difference in splitting between the high frequency branch of the formate mode in the Mn complex and the anharmonic fit,

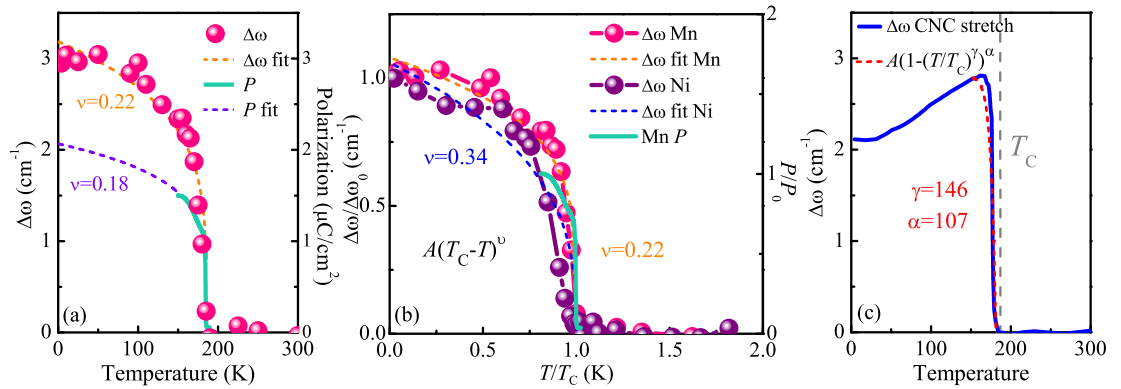


Figure 5.3: (a) Splitting of the formate bending mode vs. temperature in the Mn complex, a power law fit to this data, and polarization from Ref. 37, along with a corresponding power law fit. (b) Overlay of the formate bending mode splittings in the Mn and Ni complexes, along with their power law fits and extracted critical exponents. (c) Calculated cooling rate of the C-N-C stretch along with an extended power law fit. [120]

overlain with polarization measurements. [37, 83] The critical exponent extracted from a power-law fit of $A(T_C - T)^\nu$ to the phonon splittings are in reasonable agreement with a fit to the polarization ($\nu = 0.22$ versus 0.18, respectively). For the power law fit to the spectroscopic data, the entire temperature range below T_C was included; no significant change in the critical exponent was found by varying the temperature window. We also fit the available temperature range of the polarization data. [37] Here, T_C was not used as a fit parameter; this value was taken directly from Ref. 56. These values are suggestive of a quasi-two-dimensional system, since the total critical exponent (ν) for a true Ising system is 0.125. [64] A summary of these values is given in Table 5.1. Figure 5.3 (b) displays the frequency difference between the formate bending modes and anharmonic fits for the Mn and Ni compounds. Both axes are normalized for the purpose of comparison since T_C and splitting values vary with transition metal identity. A power law analysis reveals that while the extracted critical exponent in the Mn complex is $\nu = 0.22 \pm 0.01$, the model fit for the Ni compound produces a value of $\nu = 0.34 \pm 0.03$, which is larger and much closer to mean field behavior, where ν is 0.5. [64, 180] The larger exponent is also indicative of a more gradual transition into the polarized state, clear from visual examination of the data, supported too by the less complete splitting pattern in Fig. 5.2 (b). *B*-site substitution thus reveals that although the structural and vibrational properties of the Mn and Ni complexes are nearly identical, the dimensionality of the ferroelectric phase transition develops differently and is somewhat more three dimensional in the Ni compound. [120]

In order to compare the behavior of the framework across T_C against that of the counterion, we analyze the C-N-C stretch [Fig. 5.3 (c)]. It is well known that the ferroelectric transition in $[(\text{CH}_3)_2\text{NH}_2]\text{Mn}(\text{HCOO})_3$ can have a strong hysteresis. The size of the hysteresis loop is reduced with decreasing cooling rate; it collapses

Table 5.1: Comparison of theoretical [64] critical exponents ν for the power law fit $A(T_C - T)^\nu$ along with exponents extracted from the Mn and Ni data above. The values suggest that the Mn system is more two-dimensional (being closer to the predicted Heisenberg and Ising exponents), while the Ni material is closer to the mean-field, three-dimensional predictions. [120]

| Theoretical ν | | Experimental ν | |
|-------------------|------------|--|------------------|
| Mean Field | 0.5 [64] | $[(\text{CH}_3)_2\text{NH}_2]\text{Mn}(\text{HCOO})_3$ vib. properties | 0.22 ± 0.01 |
| Heisenberg | 0.367 [64] | $[(\text{CH}_3)_2\text{NH}_2]\text{Mn}(\text{HCOO})_3$ polarization | 0.18 ± 0.001 |
| Ising | 0.125 [64] | $[(\text{CH}_3)_2\text{NH}_2]\text{Ni}(\text{HCOO})_3$ vib. properties | 0.34 ± 0.03 |

upon extrapolation to extremely low cooling rates. [83] An extended power law fit of $A(1 - (T/T_C)^\gamma)^\alpha$ reveals unrealistically high values of γ and α , signifying that the counterion transition is rigid and abrupt. This is evidenced by the extremely sharp step in the data [Fig. 5.3 (c)]. Although this fit is the same form as the regular power law, the additional exponent provides extra fitting flexibility. It turns out that this makes no difference anyway because the fit did not converge. This behavior is consistent with $(\text{CH}_3)_2\text{NH}_2$ catching slightly (due to hydrogen bonding) at T_C , distorting the structure, but then continuing to tumble within the formate framework until about 10 K below the transition temperature. [122, 123] At this point, the counterion finally locks into position and the material becomes completely ordered. [122, 123] Thus, the kinetics of the counterion rotation in $[(\text{CH}_3)_2\text{NH}_2]\text{Mn}(\text{HCOO})_3$ cause the transition to be slow to relax. The delayed reaction of the amine also explains why the hysteresis curves are not centered around T_C .

The vibrational response of $[(\text{CH}_3)_2\text{NH}_2]\text{Co}(\text{HCOO})_3$ is remarkably distinct. At room temperature, three peaks are apparent in the vicinity of the formate bend. They become increasingly resolved with decreasing temperature. A plot of peak position vs. temperature reveals that these features behave anharmonically and are completely insensitive to the development of ferroelectric polarization at $T_C=165$ K [Fig. 5.2 (f)]. This is surprising because splitting of the formate bending mode is an

essential aspect of the ferroelectric transition mechanism in the Mn and Ni complexes. Where two peaks in the Mn and Ni compounds develop due to differences in hydrogen bonds from the counterion to the framework, the drive towards counterion-locking is less obvious in the Co complex. We propose that this difference has its origins in slight distortions of the CoO_6 octahedra. This supposition is supported by our lattice dynamics calculations which predict six branches to the mode pattern. As with most materials, decreasing temperature sharpens modes by reducing linewidth [Fig. 5.2 (c)]. In $[(\text{CH}_3)_2\text{NH}_2]\text{Co}(\text{HCOO})_3$, three peaks become more resolved from the broad band with decreasing temperature. Six individual peaks are, however, not resolved due to energetic degeneracies. Although we did not notice any critical slowing down behavior, the inactivity of the framework through T_C in the Co complex is consistent with glassy character and may correlate with glassy magnetism below T_N . [125] Finally, we point out that despite the change in spin state across T_C , [40] neither the formate bending nor stretching modes engage in magneto-elastic coupling.

Figure 5.2 (d-f) summarizes the behavior of the C-N-C counterion stretching mode, which has clear features at the ferroelectric transition in all materials. In the Mn and Ni complexes, the distortion appears as a broadened step, with the mode shifting suddenly to higher frequencies with decreasing temperature. For the same temperature-time gradient, the hysteresis loop in the Ni analog is much larger (30 K) than that in the Mn case (3 K), revealing differences in ordering speeds of the amine. By contrast, the C-N-C stretching mode in $[(\text{CH}_3)_2\text{NH}_2]\text{Co}(\text{HCOO})_3$ displays a small cusp at T_C and softens upon entry into the ferroelectric state [Fig. 5.2 (f)]. The transition does not have a strong hysteresis. This mechanistic difference derives from slightly distorted CoO_6 octahedra in the room temperature structure. In $[(\text{CH}_3)_2\text{NH}_2]\text{Co}(\text{HCOO})_3$, the amine locks into place quickly because the framework is already distorted, and therefore no additional distortion through T_C is required.

Only the rotating counterion is important. In the Mn and Ni materials, the ferroelectric transition mechanism is a cooperative effort between the counterion and the framework, where the amine waits for the framework to become completely distorted before fully ordering.

5.3 Magnetoelastic coupling and the metal center

Figure 5.4 summarizes the magneto-infrared response of our three materials of interest. As previously demonstrated, magnetoelastic coupling in $[(\text{CH}_3)_2\text{NH}_2]\text{Mn}(\text{HCOO})_3$ involves the Mn-O-C-O-Mn superexchange pathway. [83] Evidence for this conclusion is recapped in Fig. 5.4 (a,d), where the -O-C-O formate bending mode displays a derivative-like shape in $\Delta\alpha$. This is the only phonon that is sensitive to applied field. In order to demonstrate how the magneto-infrared response correlates with the spin pattern, we plot the square of the magnetization, [30] $[M(B)]^2$, and the integral of the absolute value of the absorption difference over an appropriate energy window ($\int |\Delta\alpha| d\omega$) vs. magnetic field. Distortions of the formate bending mode develop with increasing field and saturate at 15.3 T - tracking $[M(B)]^2$ very well. We had anticipated that similar local lattice distortions would accompany the approach to the fully polarized magnetic transitions in the Ni and Co analogs since the mechanism for a cAFM $\rightarrow B_{\text{SF}} \rightarrow$ fully polarized state within this family of materials seems to be characteristic. We instead find substantial variations in this picture.

Figure 5.4 (b) displays a close-up view of the magneto-infrared response of $[(\text{CH}_3)_2\text{NH}_2]\text{Ni}(\text{HCOO})_3$ at 0 and 35 T in the vicinity of the formate bending and stretching modes. The full field absorption difference spectra $[\Delta\alpha = \alpha(\omega, B) - \alpha(\omega, B = 0)]$ is shown in green. The absorption difference spectra is nearly flat; in other words, there is an immeasurable difference caused by 35 T.

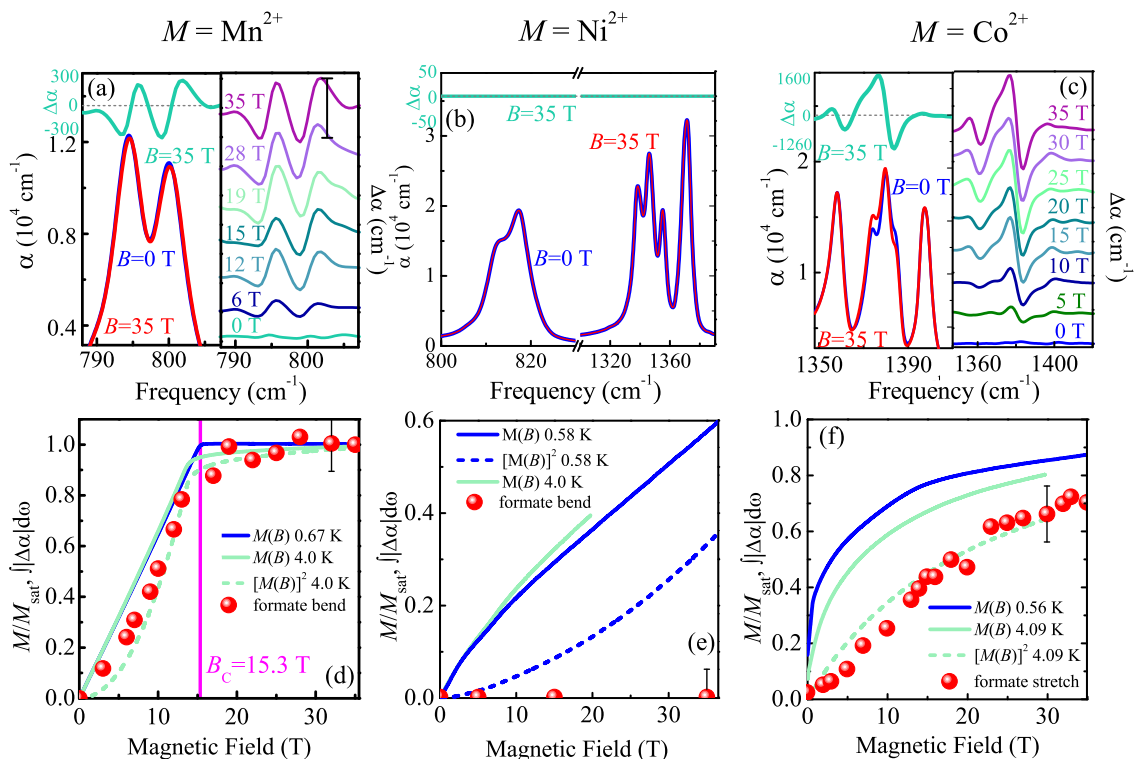


Figure 5.4: (a-c) Absolute absorption spectra at 0 and 35 T for the $[(\text{CH}_3)_2\text{NH}_2]M(\text{HCOO})_3$ materials along with waterfall plots of the absorption difference at 4.2 K highlighting spectral changes in applied magnetic field. The Mn system sports field-induced changes in the formate bending mode, whereas the symmetric O-C-O stretch is important for the Co compound. The Ni analog displays no field-dependent vibrational modes up to 35 T. (d-f) Absolute value of the absorption difference integrated over a small energy window vs. magnetic field along with the 4 K magnetization and the square of the magnetization. Error bars are indicated. [120]

Moreover, the full infrared spectrum was measured, and no other modes were active in field. This finding can be understood from how the $B - T$ phase diagrams change with B -site substitution. Specifically, the Ni centers introduce a much higher energy scale than in the Mn complex ($B_C=125$ T vs. 15.3 T). Since the Mn and Ni behave so similarly through T_C , it is likely that the formate bending mode plays a role in the approach to magnetic saturation. This trend is not observed because an 8% increase in magnetic energy (compared to the Mn analog) is outside of our sensitivity. The overall larger energy scale in $[(\text{CH}_3)_2\text{NH}_2]\text{Ni}(\text{HCOO})_3$ is also apparent in the spin flop fields ($B_{\text{SF}}=7.7$ T vs. 0.31 T).

The magneto-infrared response of $[(\text{CH}_3)_2\text{NH}_2]\text{Co}(\text{HCOO})_3$ is shown in Fig. 5.4 (c). Rather than field-induced changes in the formate bending mode, the absorption difference spectrum ($\Delta\alpha$) highlights an entirely different set of features. $\Delta\alpha$ reveals that the 1358, 1374, and 1379 cm^{-1} cluster is sensitive to magnetic field, whereas the peak at 1398 cm^{-1} is rigid. Our lattice dynamics calculations predict that the field-responsive features at 1358, 1374, and 1379 cm^{-1} are branches of the HCOO^- stretch. We therefore assign these structures as formate stretching modes. Our calculations reveal that the 1397 cm^{-1} feature is different. Instead of being a formate stretch, this peak is due to a counterion vibration - in agreement with the work in Ref. 122. Counterion modes in other materials are also well localized and insensitive to magnetic field. [84] Although full magnetic saturation is not attained (because $B_{C,\text{theor.}}=88$ T and magneto-infrared spectroscopy at the National High Magnetic Field Laboratory is carried out with 35 T resistive magnets at this time), we find that $\int|\Delta\alpha|d\omega$ over the combined energy window tracks $[M(B)]^2$ very well [Fig. 5.4 (f)]. Since these are the only modes sensitive to applied field, it is reasonable to anticipate that the distortions will stop changing at B_C and that the formate stretching modes are involved in the mechanisms resulting in eventual magnetic saturation. Even

though the saturation field is high, field-induced spectral differences are apparent in this case because stretching modes have larger oscillator strength than bending modes, giving enhanced sensitivity compared to the Ni analog. In any case, the magnetically-driven transition in $[(\text{CH}_3)_2\text{NH}_2]\text{Co}(\text{HCOO})_3$ still relies upon formate distortions, a natural consequence of the superexchange ligand linking the metal centers.

Chapter 6

Spin-lattice coupling across the magnetic quantum phase transition in Cu-containing coordination polymers

In this chapter, we measured the infrared vibrational properties of two Cu-containing coordination polymers, $[\text{Cu}(\text{pyz})_2(2\text{-HOpy})_2](\text{PF}_6)_2$ and $[\text{Cu}(\text{pyz})_{1.5}(4\text{-HOpy})_2](\text{ClO}_4)_2$, under different external stimuli in order to explore the microscopic aspects of spin-lattice coupling. While temperature and pressure control hydrogen bonding, applied field drives these materials from the antiferromagnetic \rightarrow fully saturated state. Analysis of the pyrazine-related vibrational modes across the magnetic quantum phase transition provides a superb local probe of magnetoelastic coupling because the pyrazine ligand functions as the primary exchange pathway and is present in both systems. Strikingly, the PF_6^- compound employs several pyrazine-related distortions in support of the magnetically-driven transition whereas the ClO_4^-

system requires only a single out-of-plane pyrazine bending mode. Bringing these findings together with magneto-infrared spectra from other copper complexes reveals spin-lattice coupling across the magnetic quantum phase transition as a function of structural and magnetic dimensionality. Coupling is maximized in $[\text{Cu}(\text{pyz})_{1.5}(4\text{-HOpy})_2](\text{ClO}_4)_2$ on account of its ladder-like character. Although spin-lattice interactions can also be explored under compression, differences in local structure and dimensionality drive these materials to unique high pressure phases. A symmetry analysis suggests that the high pressure phase of the ClO_4^- compound may be ferroelectric.

6.1 Development of low temperature hydrogen bonding

Figure 6.1 summarizes the infrared response of $[\text{Cu}(\text{pyz})_2(2\text{-HOpy})_2](\text{PF}_6)_2$ and $[\text{Cu}(\text{pyz})_{1.5}(4\text{-HOpy})_2](\text{ClO}_4)_2$ at 300 and 4.2 K. Although the molecular aspects of this class of material yield a number of vibrational modes below 2000 cm^{-1} , we find that in general, they can be divided into two major groups: (i) those that behave anharmonically as a function of temperature and (ii) those that reveal characteristics of hydrogen bonding. [190] Through dynamics calculations and comparisons with chemically analogous materials (Fig. S1 in Supporting Information), [114, 191–193] we assign the important modes. Given the fact that these materials are quite different in dimensionality and exchange strength – the PF_6^- complex has largely separated two-dimensional planes whereas the ClO_4^- material is a nearly isotropic spin-ladder system – it is surprising to find that the temperature dependence is rather similar.

In both materials, a vast majority of vibrations are pyrazine-related. These ligands link the Cu^{2+} centers, forming the interplane exchanges in the two-dimensional

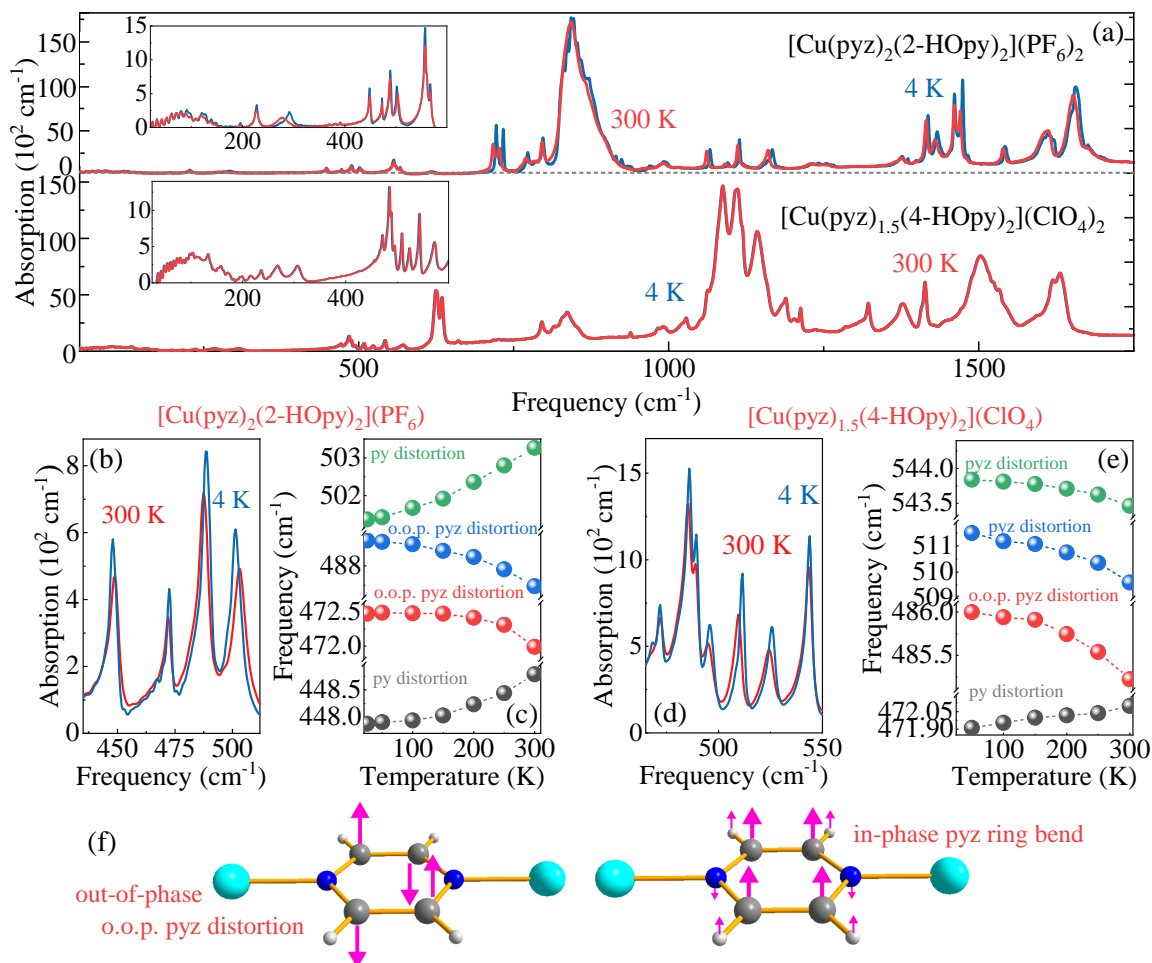


Figure 6.1: (a) Infrared absorption of $[\text{Cu}(\text{pyz})_2(2\text{-HOpy})_2](\text{PF}_6)_2$ and $[\text{Cu}(\text{pyz})_{1.5}(4\text{-HOpy})_2](\text{ClO}_4)_2$ at 300 and 4 K. Insets show the low frequency regions. (b,c) Close-up view of the pyridone (py) and pyrazine-containing (pyz) quartet in $[\text{Cu}(\text{pyz})_2(2\text{-HOpy})_2](\text{PF}_6)_2$ along with the corresponding peak position vs temperature trends. Specifically, we highlight the differences between hydrogen-bonded modes and anharmonic modes. (d,e) Close-up view of the same region in $[\text{Cu}(\text{pyz})_{1.5}(4\text{-HOpy})_2](\text{ClO}_4)_2$. (f) Calculated displacement patterns of the out-of-plane pyrazine distortion and in-phase pyrazine ring bend.

plane as well as the rungs and rails of the ladder. These modes behave anharmonically with temperature - that is, they follow $\omega = \omega_0 + \Delta(T)$, where $\Delta(T) = C[1 + \frac{2}{e^x - 1}]$ with $x = \hbar\omega_0/2k_B T$ and increase in frequency with decreasing temperature. Here, ω_0 is the unperturbed phonon frequency at base temperature, \hbar is the reduced Planck's constant, and k_B is Boltzmann's constant. As examples, we highlight the modes at 472 and 488 cm^{-1} in $[\text{Cu}(\text{pyz})_2(2\text{-HOpy})_2](\text{PF}_6)_2$, which are assigned as out-of-phase, out-of-plane pyrazine distortions [Fig. 6.1 (c)] as well as the pyrazine-related modes above 472 cm^{-1} in $[\text{Cu}(\text{pyz})_{1.5}(4\text{-HOpy})_2](\text{ClO}_4)_2$ [Fig. 6.1 (e)].

What sets $[\text{Cu}(\text{pyz})_2(2\text{-HOpy})_2](\text{PF}_6)_2$ apart is that, in addition to these vibrations, we also find evidence for improved hydrogen bonding at low temperatures. This is a direct result of the separation between the layers, which are linked via relatively long hydrogen bonds from the pyridone ligands to the PF_6^- anion via C-H \cdots F interactions. With decreasing temperature, the layered material naturally contracts, allowing hydrogen-bonding interactions to strengthen. This effect is exemplified by the 450 and 503 cm^{-1} vibrations in Fig. 6.1 (c), which characteristically redshift with decreasing temperature. [190] Signatures of hydrogen bonding exist in the ClO_4^- complex as well, but the number of demonstrative vibrations are far fewer and the effects are much smaller. For instance, the out-of-plane pyridone distortion in the ClO_4^- complex changes very slightly with temperature ($< 0.3 \text{ cm}^{-1}$) whereas in the PF_6^- complex, changes of the same mode are on the order of 1 cm^{-1} . It is therefore clear that in the spin ladder, although hydrogen-bonding interactions connect the ladders to one another via pyrazine $\cdots\text{ClO}_4^- \cdots$ pyrazine pathways, the majority of the distortions occur within the rungs and rails of individual ladders. Figure 6.1 (f) displays displacement patterns of the out-of-phase, out-of plane pyrazine bend along with the in-phase, out-of-plane C-H bend of the pyrazine. We show the latter because of the commonality of this vibration with many prominent Cu-containing

complexes. [114, 192] Below, we focus a majority of our discussion on the out-of-plane pyrazine distortions as they appear in both $[\text{Cu}(\text{pyz})_2(2\text{-HOpy})_2](\text{PF}_6)_2$ and $[\text{Cu}(\text{pyz})_{1.5}(4\text{-HOpy})_2](\text{ClO}_4)_2$ and, as it turns out, reveal important connections to the high magnetic field and pressure-induced states.

6.2 Spin-lattice coupling across the magnetic quantum phase transition

Magneto-infrared spectroscopy provides a unique opportunity to reveal spin-lattice coupling across magnetic quantum phase transitions in Cu-containing coordination polymers and to explore how this interaction varies with dimensionality. This is because we can compare the spectral response below and above these field-induced transitions in a variety of materials. Figure 6.2 (a,d) displays the infrared absorption of $[\text{Cu}(\text{pyz})_2(2\text{-HOpy})_2](\text{PF}_6)_2$ and $[\text{Cu}(\text{pyz})_{1.5}(4\text{-HOpy})_2](\text{ClO}_4)_2$ at 0 and 35 T along with the corresponding full field absorption difference spectra $\Delta\alpha(\omega) = \alpha(35 \text{ T}) - \alpha(0 \text{ T})$. The development of these features across B_C is shown with increasing magnetic field in Fig. 6.2 (b,e). Although these complexes have similar chemical building blocks, the magnetoelastic interactions that facilitate the development of the fully saturated magnetic states are quite different.

In $[\text{Cu}(\text{pyz})_2(2\text{-HOpy})_2](\text{PF}_6)_2$, we find several field-dependent vibrational modes. These include three out-of-plane pyrazine distortions at 472 cm^{-1} , 488 cm^{-1} , and a shoulder off the latter. The peak at 795 cm^{-1} , which we assign as a C-H out-of-plane pyrazine bend, is also active - just to a lesser extent. By contrast, $[\text{Cu}(\text{pyz})_{1.5}(4\text{-HOpy})_2](\text{ClO}_4)_2$ displays only one field-induced feature - an out-of-plane pyrazine distortion, which is now a well-defined doublet at 487 and 489 cm^{-1} . These pyrazine-related distortions are the only field-dependent modes; all others are rigid. This is

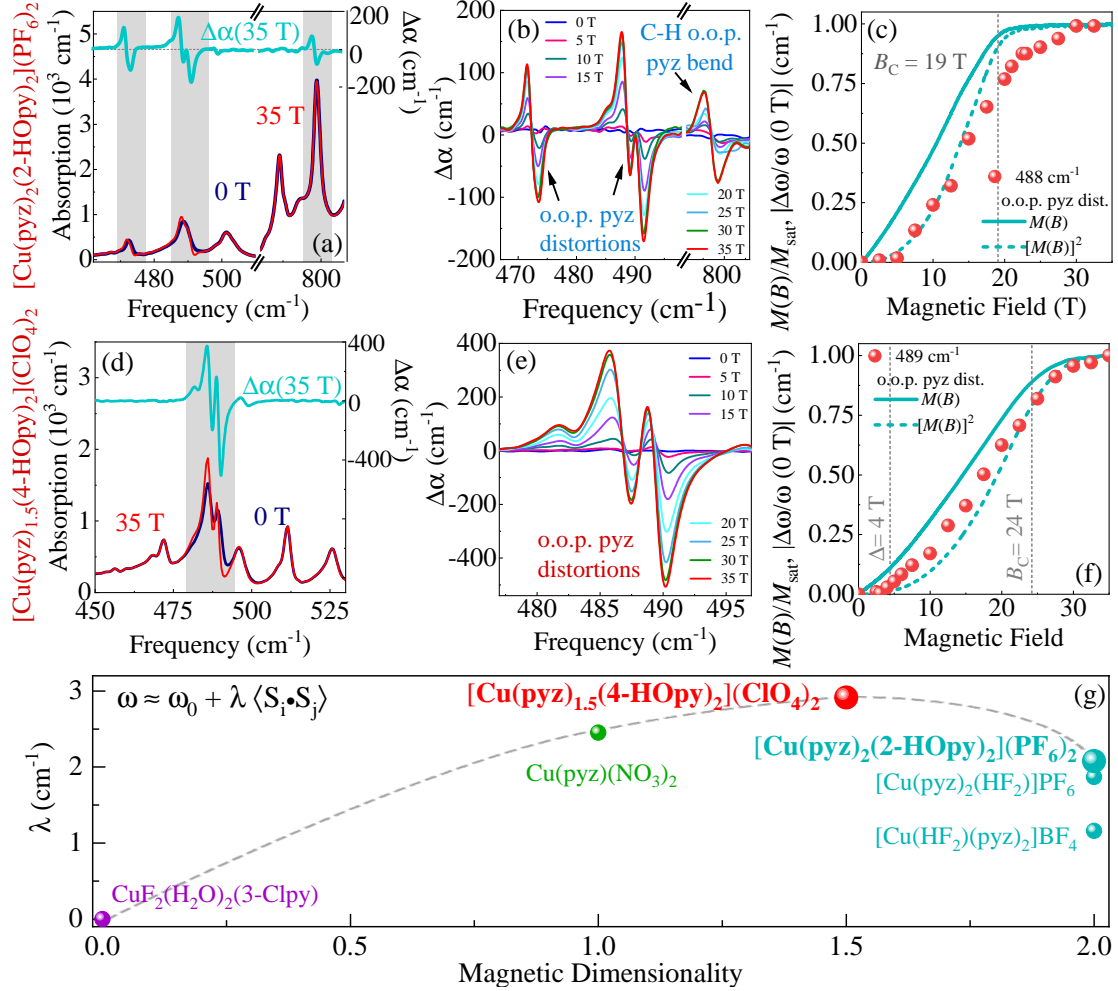


Figure 6.2: (a,d) Absorption (at 4.2 K) of $[\text{Cu}(\text{pyz})_2(2\text{-HOpy})_2](\text{PF}_6)_2$ and $[\text{Cu}(\text{pyz})_{1.5}(4\text{-HOpy})_2](\text{ClO}_4)_2$ at 0 and 35 T along with the 35 T absorption difference spectra. Vertical gray boxes highlight field-induced changes. (b,e) Absorption differences of the magneto-active modes with increasing magnetic field. (c,f) Overlay of magnetic-field-induced frequency shifts of the out-of-plane pyrazine distortions plotted with the 1.5 K magnetization [148] and the square of magnetization. The data sets are normalized above the critical field, B_C . (g) Comparison of spin-phonon coupling constant of the out-of-plane pyrazine distortion as a function of magnetic dimensionality in several well known Cu-containing coordination complexes.

because pyrazine ligands connect the Cu centers in these materials. [16, 150] As a result, the out-of-plane bending mode distorts the superexchange linkage and modulates the exchange between magnetic centers. The motion of the other modes, for instance the pyrazine stretch or the strongly temperature dependent Cu-N stretch near 290 cm^{-1} , do not have the same effect on the antiferromagnetic part of J . [114]

Table 6.1 summarizes the size of the absorption difference across the magnetically driven transition to the fully saturated state. Changes are largest in the low frequency region in both systems. The ClO_4^- also shows stronger distortions compared to the PF_6^- material. We find that $[\text{Cu}(\text{pyz})_2(2\text{-HOpy})_2](\text{PF}_6)_2$ and $[\text{Cu}(\text{pyz})_{1.5}(4\text{-HOpy})_2](\text{ClO}_4)_2$ undergo somewhat different magnetically-driven local lattice distortions due to their respective dimensionalities. At low temperature, the Cu^{2+} centers of the ladder have a tendency to form dimers, [106, 194] causing isolation of important exchange interactions. With applied magnetic field, the mechanism required to fully saturate a pair of spins therefore depends to a lesser extent on distortions along the rails, and the effects are localized within the rungs. [195] In contrast, the distortion in the PF_6^- complex is more complex, requiring a combination of out-of-plane pyrazine motions along multiple directions.

Table 6.1: Summary of magneto-active vibrations in $[\text{Cu}(\text{pyz})_2(2\text{-HOpy})_2](\text{PF}_6)_2$ and $[\text{Cu}(\text{pyz})_{1.5}(4\text{-HOpy})_2](\text{ClO}_4)_2$. We show the percent changes of absorption across the quantum critical transition of these modes, along with field-induced frequency shifts and corresponding spin-phonon coupling constants. These are related as $\omega \approx \omega_0 + \lambda \langle S_i \cdot S_j \rangle$. Here, λ is the spin-phonon coupling constant.

| Anion | Frequency (cm^{-1}) | Assignment | $\Delta\alpha/\alpha$ (%) | $\Delta\omega$ (cm^{-1}) | λ (cm^{-1}) |
|------------------|--------------------------------|----------------------|---------------------------|-------------------------------------|--------------------------------|
| PF_6^- | 472 | o.o.p. pyz dist. | 25 | 0.48 | 1.9 |
| | 488 | o.o.p. pyz dist. | 18 | 0.52 | 2.1 |
| | 797 | C-H o.o.p. pyz dist. | 2 | 0.05 | 0.2 |
| ClO_4^- | 487 | o.o.p. pyz dist. | 25 | 0.66 | 2.7 |
| | 489 | o.o.p. pyz dist. | 33 | 0.73 | 2.9 |

We can also extract frequency shifts $\Delta\omega$ across the magnetic quantum phase transitions. Figure 6.2 (c,f) displays the absolute value of the frequency shift $|\Delta\omega|$ along with the 1.5 K magnetization [148] and the square of magnetization. The data sets are normalized above the critical field, B_C . We find that the field-induced frequency shifts follow $[M(B)]^2$, rising with increasing field and leveling off above the critical field, B_C . This demonstrates that applied field drives both systems into the fully saturated magnetic state [112, 150] and that certain ligand-related phonons are sensitive to the change in spin state. A sharp knee - like that in the magnetization - is not observed at B_C because our magneto-infrared measurements were taken slightly above the ordering temperatures. Nevertheless, short-range interactions are sufficiently strong in both complexes to preserve the essential physics across the quantum phase transition. [114, 196]

Well-defined frequency shifts allow determination of spin-phonon coupling constants across the magnetic quantum phase transition. [197, 198] Generally, these values are defined as $\omega = \omega_0 + \lambda\langle S_i \cdot S_j \rangle$, where ω_0 and ω are the unperturbed and perturbed phonon frequencies, $\langle S_i \cdot S_j \rangle$ is the nearest-neighbor spin-spin correlation function, and λ is the mode-dependent spin-phonon coupling constant. [80, 81] At sufficiently low temperatures, the spin-spin correlation $\langle S_i \cdot S_j \rangle$ goes as $S^2 = (1/2)^2 = 1/4$ for Cu^{2+} spins. The magnitude of λ provides information about how the magnetic exchange interaction J is modulated by certain phonon displacements u , since $\lambda = \partial^2 J / \partial u^2$. [181] Therefore, by tracking the frequency shifts of the out-of-plane pyrazine vibrational modes in $[\text{Cu}(\text{pyz})_2(2\text{-HOpy})_2](\text{PF}_6)_2$ and $[\text{Cu}(\text{pyz})_{1.5}(4\text{-HOpy})_2](\text{ClO}_4)_2$ across the magnetically-driven transition to the fully saturated state, we can extract the spin-lattice coupling constants. Table 6.1 summarizes field-induced frequency shifts and corresponding λ 's for each field-dependent mode. In the following discussion, we focus on the out-of-plane pyrazine distortion near 490

cm^{-1} because, in both cases, λ is large.

With the addition of $[\text{Cu}(\text{pyz})_2(2\text{-HOpy})_2](\text{PF}_6)_2$ and $[\text{Cu}(\text{pyz})_{1.5}(4\text{-HOpy})_2](\text{ClO}_4)_2$, the collection of Cu-containing coordination polymers for which λ 's have been evaluated across the magnetic quantum phase transition is now broad enough to allow several interesting structure-property effects to emerge. Figure 6.2 (g) summarizes spin-phonon coupling constants for the pyrazine bend in this class of materials. [114,157,191] The overall trend is interesting. The pyrazine distortion in the spin ladder $[\text{Cu}(\text{pyz})_{1.5}(4\text{-HOpy})_2](\text{ClO}_4)_2$ sports the strongest spin-phonon coupling ($\lambda=2.9 \text{ cm}^{-1}$), whereas the one- and two-dimensional materials have slightly lower values ranging from 2.5 cm^{-1} in the chain compound to between 1.2 and 2 cm^{-1} in the various layered systems. This difference arises due to the unique structure of the spin ladder. In the quasi-two-dimensional materials, connectivity extends in the *ab*-plane. In the quasi-one-dimensional systems, distortions occur primarily in the rail direction. Both systems require several local lattice distortions to facilitate the transition to the fully saturated spin state. What makes the ladder unique is the tendency toward low temperature dimerization [194] which, in $[\text{Cu}(\text{pyz})_{1.5}(4\text{-HOpy})_2](\text{ClO}_4)_2$, makes the pyrazine ligand the primary magnetic interaction pathway between Cu^{2+} centers in the rung. By undergoing an out-of-plane bend, a single local lattice distortion can reduce the antiferromagnetic part of J and stabilize the fully saturated spin state. [114,157]

6.3 Pressure-induced structural phase transitions in Cu-containing coordination polymers

Spin-lattice interactions can also be explored under compression. [199–201] This is because pressure distorts the soft ligands that act as super-exchange pathways

in molecule-based magnetic materials and, by so doing, triggers changes in magnetic states. [5] Both processes can be probed spectroscopically. Figure 6.3 (a,c) displays close-up views of the infrared response of $[\text{Cu}(\text{pyz})_2(2\text{-HOpy})_2](\text{PF}_6)_2$ and $[\text{Cu}(\text{pyz})_{1.5}(4\text{-HOpy})_2](\text{ClO}_4)_2$ as a function of pressure at 300 K. We only display results up to 10 GPa because, although not necessarily apparent in this energy window, both complexes become amorphous above 8 GPa (dashed gray lines). A detailed discussion is available in the Supporting Information. We focus on the behavior of the pyrazine- and pyridone-related modes in order to link our findings with temperature and field effects. We track frequency vs pressure trends [Fig. 6.3 (b,d)] to quantify the pressure-driven spectral changes. Although inherently similar in composition, differences in local structure and dimensionality drive these materials to unique high pressure phases.

Figure 6.3 (a,b) summarizes the vibrational properties of $[\text{Cu}(\text{pyz})_2(2\text{-HOpy})_2](\text{PF}_6)_2$

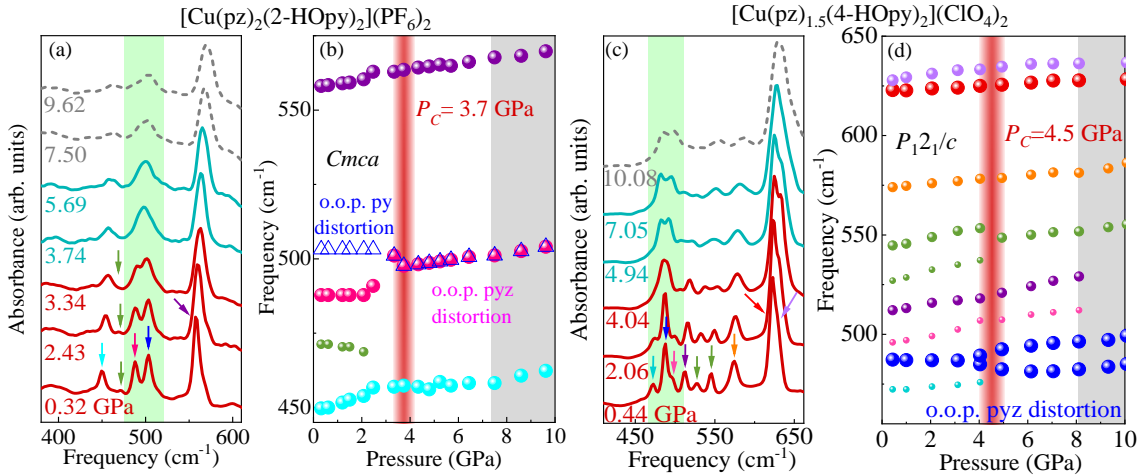


Figure 6.3: (a,c) Close-up views of the 300 K infrared spectra as a function of pressure for $[\text{Cu}(\text{pyz})_2(2\text{-HOpy})_2](\text{PF}_6)_2$ and $[\text{Cu}(\text{pyz})_{1.5}(4\text{-HOpy})_2](\text{ClO}_4)_2$, respectively. The spectra are offset for clarity. The vertical green regions highlight pressure-driven distortions. (b,d) Frequency vs. pressure trends for the modes displayed in (a,c). Critical pressures P_C are indicated by vertical red lines. The gray areas indicate the point at which each system becomes amorphous (Supporting Information).

HOpy)₂](PF₆)₂ as a function of pressure. The 487 cm⁻¹ out-of-plane pyrazine bend (which links the metal centers) hardens under compression whereas the 503 cm⁻¹ pyridone distortion (which stabilizes the layered structure) softens. The two branches come together across the 3.7 GPa structural phase transition [Fig. 6.3 (b)], consistent with the development of a higher symmetry phase. The 450 and 470 cm⁻¹ modes (a pyridone- and pyrazine-containing distortion, respectively) converge across the critical pressure P_C as well. Naturally, the easy axis of compression in the PF₆⁻ compound is along c . Pressure therefore enhances the interlayer hydrogen bonding and stabilizes the structure. The pyridone bending mode softens as a result - analogous to the aforementioned temperature trends [Fig. 6.3 (b)]. The primary contraction along c that strengthens interlayer interactions is accompanied by a relatively simple ab -plane shrinkage that brings the Cu²⁺ centers closer together while distorting the pyrazine ligands.

The [Cu(pyz)_{1.5}(4-HOpy)₂](ClO₄)₂ spin ladder displays local lattice distortions that are consistent with a change in symmetry under compression. Although many of the modes harden systematically under pressure, the out-of-plane pyrazine distortion at 487 cm⁻¹ splits across the 4.5 GPa transition [Fig. 6.3 (d)]. Thus, while the pyrazine ligands in the rung and rail directions are nearly indistinguishable in the low pressure phase, the system becomes anisotropic above $P_C = 4.5$ GPa. We anticipate strengthened Cu···Cu exchange pathways in the rung direction due to the natural tendency for spin ladders to dimerize. [202] Although pressure may improve inter-ladder hydrogen bonding, these interactions, as in the temperature and magneto-infrared measurements, are relatively weak. In any case, splitting of the out-of-plane pyrazine distortion across the pressure-driven transition in the ClO₄⁻ complex is consistent with the development of a lower symmetry space group. A subgroup analysis of the $P2_1/c$ space group [121] reveals several candidate high pressure phases includ-

ing $P1$, $P2_1$, and P_C . In the $P2_1/c$ space group, an inversion center is present due to the intersection of a c -glide plane and a two-fold screw axis (2_1). The lower symmetry space groups do not have this intersection. All of the potential low symmetry structures including $P1$, $P2_1$, and P_C are therefore ferroelectric [121], suggesting that low-dimensional magnetic materials like $[\text{Cu}(\text{pyz})_{1.5}(\text{4-HOpy})_2](\text{ClO}_4)_2$ have potential applications as a multiferroic. The transition to a lower symmetry space group along with pressure-induced modifications to the superexchange pathways may also shift the magnetic quantum phase transition to lower fields. [31]

Given the variety of copper-containing coordination polymers and the fact that spin-phonon coupling constants are sizable and show clear structure-property relations across the magnetic quantum phase transition [Fig. 6.2 (g)], we sought to correlate the behavior across P_C with magnetic dimensionality. There is, however, no apparent trend - probably due to the complexity of the pressure-induced transitions in these materials. In fact, many Cu and Ni coordination complexes have multiple structural transitions under compression with signatures of disorder above 8 or 10 GPa. [203, 204] While applied field drives these materials into the fully saturated state in such a way that the field-dependent local lattice distortions modulate the superexchange pathway, pressure induces a more generalized lattice response with contributions from all of the soft linkages. Only a few of these trigger magnetic crossovers.

6.4 Supporting information

Assigning pyrazine- and pyridone-related vibrational modes

We assign vibrational modes in $[\text{Cu}(\text{pyz})_2(\text{2-HOpy})_2](\text{PF}_6)_2$ and $[\text{Cu}(\text{pz})_{1.5}(\text{4-HOpy})_2](\text{ClO}_4)_2$ using three different strategies: lattice dynamics calculations,

measurements of chemically similar materials, and comparisons with literature data. For the work with chemically related materials, we measured the vibrational properties of several different copper-containing coordination polymers including $\text{Cu}(\text{HF}_2)(\text{pyz})_2\text{BF}_4$ [205], $\text{Cu}(\text{HF}_2)(\text{pyz})_2\text{ClO}_4$ [205], $[\text{Cu}(\text{pyz})_2(2\text{-HOpy})_2](\text{BF}_4)_2$, and $[\text{Cu}(\text{pyz})_2(2\text{-HOpy})_2](\text{ClO}_4)_2$. The latter two are very similar in structure to the PF_6 complex of interest here. The infrared response of these systems is summarized in Fig. 6.4. Our specific goal was to compare and distinguish the cluster of modes between 475 and 525 cm^{-1} . This is challenging because pyrazine- and pyridone-related vibrations resonate in close proximity to each other. Even so, the distinction becomes especially important for interpreting high pressure effects in $[\text{Cu}(\text{pyz})_2(2\text{-HOpy})_2](\text{PF}_6)_2$ and $[\text{Cu}(\text{pyz})_{1.5}(4\text{-HOpy})_2](\text{ClO}_4)_2$.

The blue band in Fig. 6.4 highlights pyrazine-related distortions. This vibration is present in all six compounds and is well-understood in literature as an out-of-plane pyrazine bend [191, 192]. A single feature is present for $[\text{Cu}(\text{pyz})_2(2\text{-HOpy})_2](\text{PF}_6)_2$ and the two HF_2 -containing complexes because these three compounds are planar and essentially square. They contain only one pyrazine environment. On the other hand, both $[\text{Cu}(\text{pyz})_{1.5}(4\text{-HOpy})_2](\text{ClO}_4)_2$ and the two other $[\text{Cu}(\text{pyz})_2(2\text{-HOpy})_2]$ layered complexes have a doublet in this region, indicative of unique pyrazine environments. The mode near 503 cm^{-1} (highlighted in pink) is absent in both $\text{Cu}(\text{HF}_2)(\text{pyz})_2\text{BF}_4$ and $\text{Cu}(\text{HF}_2)(\text{pyz})_2\text{ClO}_4$ where pyridine is not part of the chemical structure. We therefore assign this feature as an out-of-plane pyridone bend. The lower vibration of this pyridone doublet is seen near 450 cm^{-1} . A side-by-side comparison also reveals the BF_4^- and ClO_4^- counterion modes. We note that the spin ladder $[\text{Cu}(\text{pyz})_2(2\text{-HOpy})_2](\text{ClO}_4)_2$ has several additional features, probably due to the fact that there are two sets of interactions – those along the rung and those along the rail – which act to split the modes.

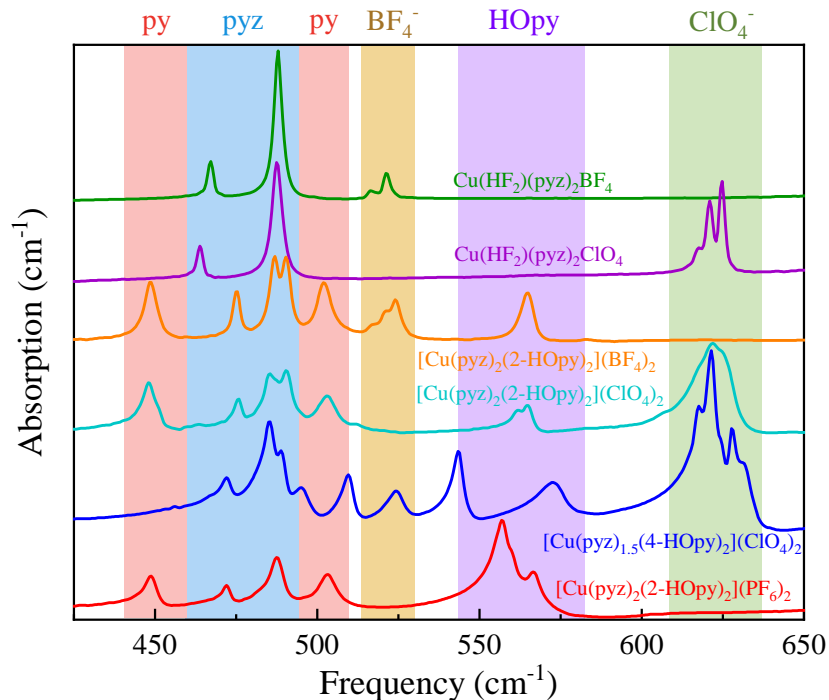


Figure 6.4: Comparison of several copper-containing coordination polymers in the relevant frequency range. We highlight a number of similarities between these complexes including pyrazine-, pyridone-, HOpy, and BF_4^- - and ClO_4^- -related modes. Our goal is to assign vibrations in $[\text{Cu}(\text{pyz})_{1.5}(4\text{-HOpy})_2](\text{ClO}_4)_2$ and $[\text{Cu}(\text{pyz})_2(2\text{-HOpy})_2](\text{PF}_6)_2$ (dark blue and red spectra on the bottom.)

Disordered high pressure phase in copper-containing coordination polymers

Figure 6.5 summarizes the infrared and Raman response of $[\text{Cu}(\text{pyz})_2(2\text{-HOpy})_2](\text{PF}_6)_2$ and $[\text{Cu}(\text{pyz})_{1.5}(4\text{-HOpy})_2](\text{ClO}_4)_2$ under compression. To highlight differences, we show spectra taken below the critical pressure (P_C), above P_C , and in the amorphous region. Although we focus on the infrared response in the main text, evidence for disorder is also present in the Raman spectra. Both materials display compression-induced structural phase transitions. The infrared-active modes reveal new splitting patterns across P_C whereas most of the Raman modes harden (and decrease in intensity) under pressure. At higher levels of compression, the phonons in these materials start to lose their coherency and definition due to disorder. As a

result, many features can not be easily tracked because the signatures of individual peaks are smeared in this range. In $[\text{Cu}(\text{pyz})_2(2\text{-HOpy})_2](\text{PF}_6)_2$, the lattice loses coherence above 7.42 GPa. Similar signatures of disorder appear near 8.08 GPa in $[\text{Cu}(\text{pyz})_{1.5}(4\text{-HOpy})_2](\text{ClO}_4)_2$. These onset pressures along with evidence for amorphous states in related materials [203] suggests that we can anticipate signatures of disorder between 6 and 8 GPa in this family of compounds. Whether there is a commonality in the mechanism is a topic for future work.

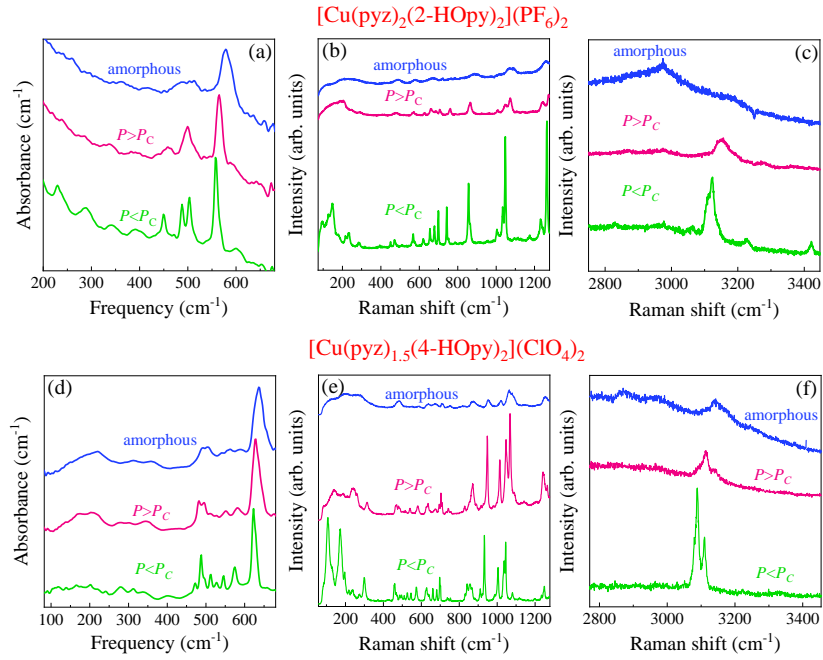


Figure 6.5: (a) Infrared absorption and (b, c) Raman scattering spectra of two-dimensional $[\text{Cu}(\text{pz})_2(2\text{-OHpy})_2](\text{PF}_6)_2$ below P_C , above P_C , and in the disordered phase. (d-f) Corresponding spectra for ladder-like $[\text{Cu}(\text{pz})_{1.5}(4\text{-OHpy})_2](\text{ClO}_4)_2$. All data are taken at room temperature, and the spectra are offset for clarity.

Chapter 7

Observation of magnetoelectric, spin-lattice, and electron-phonon coupling in multiferroic



In this chapter, I bring together pulsed-field polarization techniques, magneto-infrared spectroscopy, and lattice dynamics calculations to uncover the high magnetic field coupling mechanism of P and B in $(\text{NH}_4)_2[\text{FeCl}_5 \cdot (\text{H}_2\text{O})]$ and to explore the structural distortions that this system undergoes through various magnetic phases and across the magnetic quantum phase transition. High-field polarization is quenched by the quasicollinear \rightarrow collinear sinusoidal magnetic transition. Strikingly, spin-lattice coupling across the magnetic quantum phase transition reveals that nearly all low-frequency vibrations modulate magnetic exchange via hydrogen- and halogen-bonding interactions. An analysis of combined techniques demonstrates that magneto-infrared is sensitive to both spin-phonon and electron-phonon coupling.

7.1 Electric polarization across the magnetic quantum phase transition

Figure 7.1 displays the polarization of $(\text{NH}_4)_2[\text{FeCl}_5 \cdot (\text{H}_2\text{O})]$ as a function of magnetic field. Specifically, we highlight the $P||a, B||c$ configuration. Figure 7.1 (a) shows the electric polarization ΔP as a function of magnetic field at various temperatures both above and below $T_{\text{FE}}=6.9$ K. We find that polarization values are small at low magnetic fields, falling to zero near 5 T. This is in excellent agreement with previous reports that polarization lies primarily within the ab plane (9° off of the a -axis) in zero field and flops to the c -axis at 5 T, concurrent with the magnetic spin-flop transition. [61,90] In any case, this transition is not strongly temperature dependent, and signatures of the phase diminish above 6 K. Given the size of the magnetic moments ($\approx 4.6 \mu_{\text{B}}/\text{f.u.}$ at B_{C}) and the electric polarization ($\Delta P = 1.8 \text{ nC/cm}^2$ at P_{max}), magnetism likely drives the changes in polarization. Therefore, the 5 T polarization flop in $(\text{NH}_4)_2[\text{FeCl}_5 \cdot (\text{H}_2\text{O})]$ is triggered by the magnetic spin-flop transition. This is consistent with a type-II multiferroic mechanism in which electric polarization is lost above the magnetic ordering temperature or whenever spin order vanishes.

Unexpectedly, polarization begins to rise again in this configuration with increasing magnetic field. Previous work suggests that ΔP disappears above the spin-flop transition when $P||a$ and that polarization subsequently rises after 5 T in the $P||c$ configurations. [61] We find that values increase systematically above 5 T, reaching a maximum at 26 T. At low temperatures, ΔP displays a dome-like trend with field that rises gradually and drops off sharply at higher magnetic fields. At 1.5 K, polarization goes to zero near 26 T; the magnitude of the 4 K curve is overall smaller, falling to zero at 21 T. The 6 K curve shows small signatures of this transition,

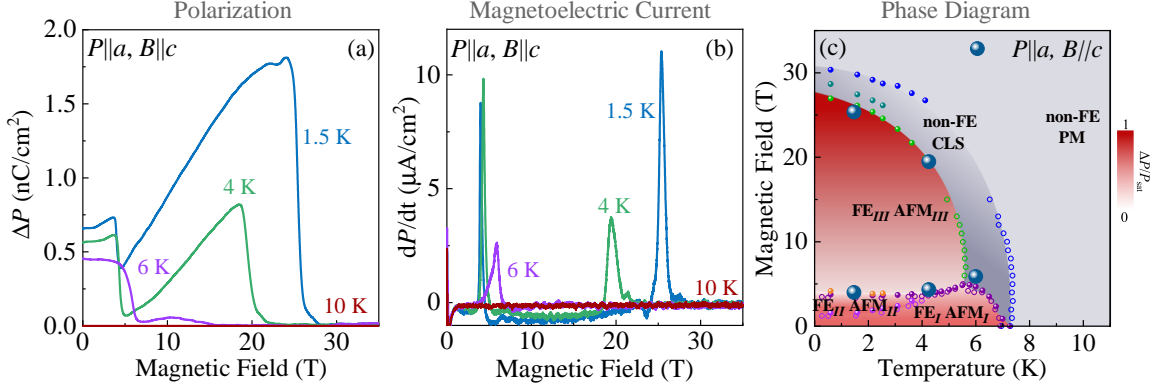


Figure 7.1: (a) Change in electric polarization (ΔP) of $(NH_4)_2[FeCl_5 \cdot (H_2O)]$ as a function of magnetic field at various temperatures. This is the $P||a, B||c$ configuration. Others are given in Supplemental Information. (b) Magnetolectric current I vs B , highlighting changes in $\Delta P(B)$. (c) B - T phase diagram of $(NH_4)_2[FeCl_5 \cdot (H_2O)]$; points taken from the magnetolectric current measurement are indicated in light blue. [90] A color bar is included to illustrate the strength of ΔP with field – red signifies a strong response and white represents zero polarization.

but the effects are smeared – probably due to the fact that these data are in close proximity to the triple point of the phase diagram and that some short-range interactions survive above the ordering temperature. [30] The dome-like shape of our data is reminiscent of the magnetic saturation, which is characteristic of a typical antiferromagnet in that saturation values are high at lowest temperatures and fall off towards $T_N=7.25$ K. [90] In order to investigate this correlation, we show the derivative of ΔP – the magnetolectric current I vs. B – in Fig. 7.1 (b). The use of derivative techniques provides a precise determination of changes in polarization; we uncover the low- and high-field transition fields in polarization with relatively small error bars and definitively reveal high-field multiferroic behavior.

Bringing the high-field polarization behavior together with previous magnetization work, we reveal the complete B - T phase diagram of $(NH_4)_2[FeCl_5 \cdot (H_2O)]$ summarizing the behavior of both electric polarization and spin [Fig. 7.1 (c)]. [61,90,153] Small open circles denote the different ferroelectric phases, [61] small spheres show the spin-flop transition, spin reorientations, and magnetic saturation, [90] and the

large blue spheres are data points taken directly from the magnetoelectric current reported in this work. The changes in low-field polarization at low magnetic field are consistent with the cycloidal \rightarrow quasicollinear magnetic transition. Our measurements serve as further proof that this transition is of magnetoelectric origin, since previous reports only measured either the magnetic or electric aspects, and here we measure how they interact. The overall strength of ΔP is depicted with the red scale bar, where dark red represents larger changes in polarization and white signifies zero change. Surprisingly, we find that polarization does not correlate with the magnetic saturation field ($B_C=30$ T at the lowest temperatures) as one might naively expect for a magnetoelectric complex, but rather with the first small magnetic reorientation leading up to saturation. Once the magnetic spin arrangements begin to change, ΔP reaches a maximum and drops suddenly to zero, despite the fact that the overall magnetic moment continues to grow. Polarization is lost at the quasicollinear magnetic orientation to collinear sinusoidal configuration transition – as expected for a type-II multiferroic. It collapses entirely before the magnetic quantum phase transition. We note that all measurement configurations show an overall loss of polarization at the same magnetic field, proving that polarization does not merely flop to another axis at this transition.

7.2 Lattice distortions through the order-disorder phase and the magnetic quantum phase transition

$(\text{NH}_4)_2[\text{FeCl}_5 \cdot (\text{H}_2\text{O})]$ is well-studied in the infrared, although the majority focused on vibrational motions of water-coordinated aquo-complexes as a whole and how vibrations varied with counterion substitution (K, Rb, NH_4). [206–208] Our interests

are different and instead lie in the microscopic lattice changes across the 79 K order-disorder transition and the development of the low temperature, magnetoelectric state. We assign modes based off of lattice dynamics calculations and calculated displacement patterns. What is unique about this work is the heavy focus on the low-frequency modes, since previous work primarily investigates lattice activity above 350 cm^{-1} .

We track the vibrational modes as a function of temperature – by doing so, we unveil several different trends including mode splitting, characteristics of anharmonicity, and signatures of hydrogen bonding [Fig. 7.2]. Importantly, nearly every mode is responsive to the order-disorder transition at 79 K. This is surprising since this transition is reported as a subtle distortion to a monoclinic phase. [209] That nearly every mode responds to this transition signifies that, although $T_{o/d}$ does not drastically alter the overall crystal structure, the induced hydrogen bonding does lower the local symmetry of several centers – namely those that split below the order-disorder transition like the H_2O wag and the NH bend [Fig. 7.2 (a,e)]. Frequency vs temperature plots reveal that hydrogen bonding interactions – though typically weak compared to traditional covalent bonds – play an important role in molecular materials with low energy scales and flexible architectures.

To examine spin-lattice coupling in this hydrogen- and halogen-bonded multiferroic and to determine which of the competing magnetic exchange pathways aid in the development of the fully saturated magnetic state, we measure the magneto-infrared response of $(\text{NH}_4)_2[\text{FeCl}_5 \cdot (\text{H}_2\text{O})]$ at 4.2 K across the magnetic quantum phase transition. Figure 7.3 (a) displays the low-frequency regime of $(\text{NH}_4)_2[\text{FeCl}_5 \cdot (\text{H}_2\text{O})]$ at 0 and 35 T, along with the 35 T absorption difference curve $\Delta\alpha = \alpha(35 \text{ T}) - \alpha(0 \text{ T})$, which serves to emphasize small changes with magnetic field. Some of the most important modes include the Fe-Cl stretch at 276 cm^{-1} , the Fe-O stretch at 365 cm^{-1} ,

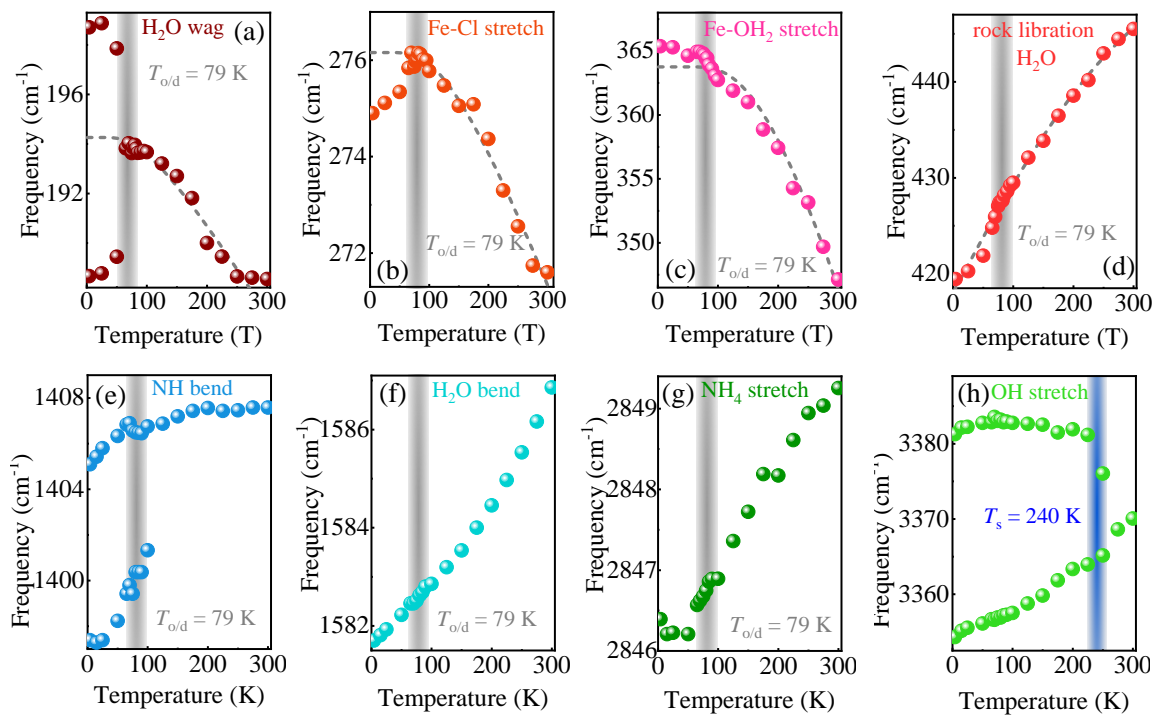


Figure 7.2: Frequency vs temperature plots of several important modes, emphasizing the differences in behavior as a function of temperature.

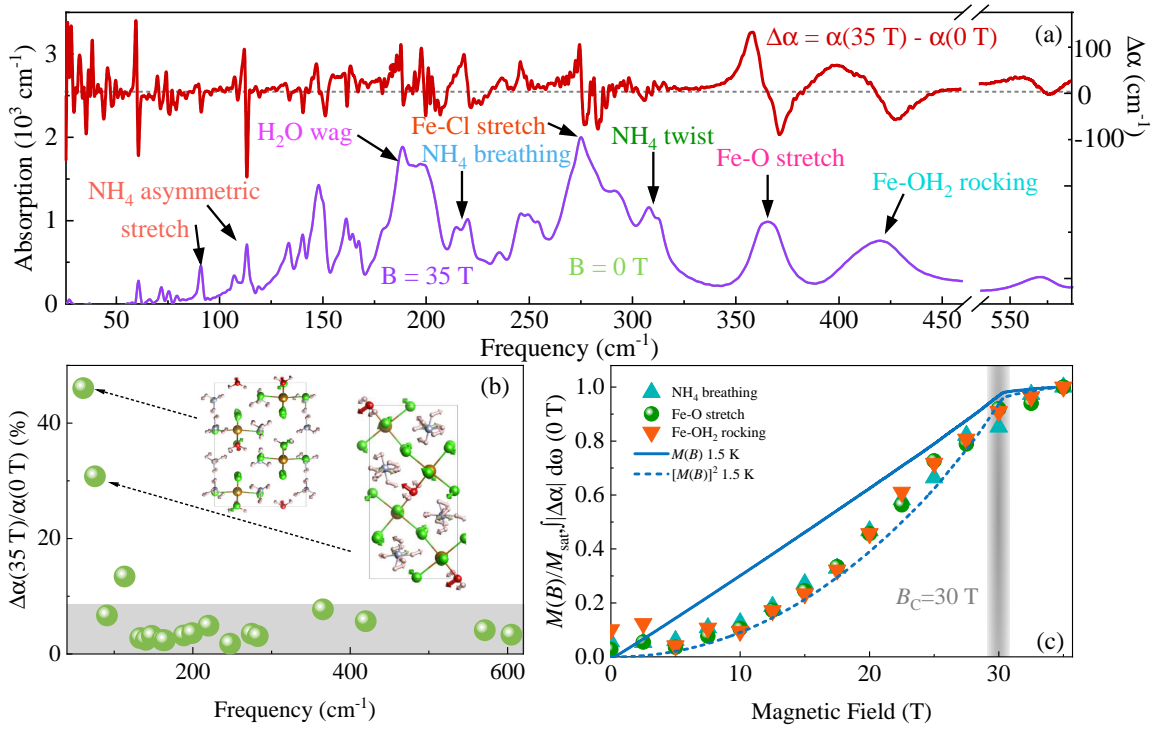


Figure 7.3: (a) Absorption of $(\text{NH}_4)_2[\text{FeCl}_5(\text{H}_2\text{O})]$ at 0 at 35 T in the low-frequency regime along with the 35 T absorption difference spectrum, $\Delta\alpha = \alpha(35\text{ T}) - \alpha(0\text{ T})$. All vibrations in this region are magneto-active. (b) Analysis of percent changes of absorption across the magnetic quantum phase transition. (c) Overlay of the integrated area of several magneto-active vibrations along with the low-temperature magnetization [90] and the square of magnetization. The magnetic saturation region is shown by the vertical gray box.

and the Fe-OH₂ stretch at 420 cm⁻¹. Remarkably, we uncover that every lattice distortion below 600 cm⁻¹ is sensitive to applied magnetic field. This is entirely different than other molecule-based magnets like Cu(py_z)(NO₃)₂ and [Cu(py_z)₂(HF₂)]PF₆, where only one or two distortions aid in the development of the magnetic quantum phase. [84, 120, 157] The higher frequency modes are completely rigid because they are localized vibrations and counterion distortions rather than metal-containing or superexchange-related vibrations such as those that resonate lower frequencies. Figure 7.3 (b) reveals the relative size of the field-induced changes $\Delta\alpha(35\text{ T})/\alpha(0\text{ T})$ of these low-frequency modes. The majority of the distortions change up to 10% with magnetic field. However, several of the lower frequency distortions reveal much greater modifications with field – up to 46% in the largest case.

In order to quantify these field-induced effects, we integrate the absolute value of the absorption differences $\int |\Delta\alpha|d\omega$ and plot them as a function of magnetic field. In this way, we can discern how specific lattice distortions are involved in the development of the 30 T magnetic quantum phase. Figure 7.3 (c) displays the integrated absorption differences of several important modes, the magnetization [90], and the square of magnetization at low temperature. By analyzing the various superexchange pathways, we find that applied field affects vibrations corresponding to changes in all of the J exchange pathways, namely the H₂O wag and the NH₄-related motions. This is evidenced by the fact that a majority of these lattice distortions follow $[M(B)]^2$; $\int |\Delta\alpha|d\omega$ reaches a plateau as magnetization saturates, indicative that these distortions are sensitive to the microscopic nature of the spin state. Although there are competing low-field magnetic phases in addition to a series of spin transitions leading up to the full field saturation in (NH₄)₂[FeCl₅·(H₂O)], [90, 153] we do not see evidence for this frustration in the integrated absorption differences – probably due to the sensitivity of the experiment.

Spin-lattice coupling is often observed in materials in which ligands directly link magnetic centers including many rare-earth manganites [200, 210] and more recently, molecule-based magnetic systems of varying connectivities [3, 120, 211]. $(\text{NH}_4)_2[\text{FeCl}_5 \cdot (\text{H}_2\text{O})]$ – with a plethora of low-frequency magneto-active vibrations that arise solely due to changes in hydrogen and halogen bond interactions – is extremely rare, and the implications for these interactions are wholly unexplored. Other molecular magnets with hydrogen-bonded superexchange pathways reveal a distinct lack of spin-lattice coupling. [84] $(\text{NH}_4)_2[\text{FeCl}_5 \cdot (\text{H}_2\text{O})]$, being completely molecular in nature, provides one of the first examples of magnetic field-driven spin-lattice coupling mediated by hydrogen bonding and opens the door to a new area of molecular multiferroics in which generally weakly-coupled interactions can toggle new magnetic phases. That the strengths of these exchanges are comparable to traditional metal-ligand-metal values is important towards the development of entirely new classes of materials in which spin-lattice coupling is variable and direct metal exchange is no longer a requirement to access quantum phases.

7.3 Microscopic signatures of charge-spin-lattice coupling

In order to unravel the distinct modifications that $(\text{NH}_4)_2[\text{FeCl}_5 \cdot (\text{H}_2\text{O})]$ undergoes with applied electric and magnetic field, we sought to directly correlate two bulk techniques – polarization and magnetization – along with a microscopic technique, magneto-infrared spectroscopy. Figure 7.4 displays the normalized magnetization [90], square of the magnetization, polarization, and $\int |\Delta\alpha| d\omega$ of the Fe-O stretch and the Fe-OH₂ rocking mode. We highlight these particular modes because they display large changes with magnetic field and play important roles in the magnetic

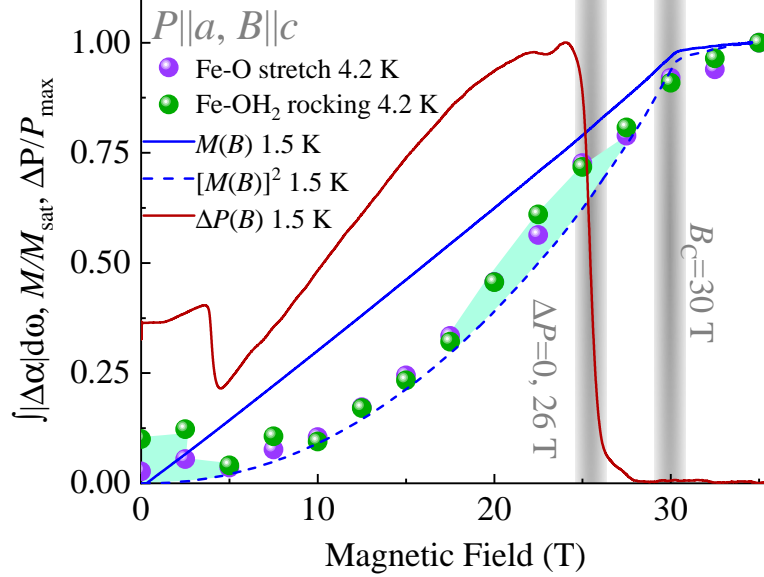


Figure 7.4: Comparison of the absolute value of the absorption differences of two important magneto-infrared distortions, magnetization [90], the square of magnetization, and ΔP of $(\text{NH}_4)_2[\text{FeCl}_5 \cdot (\text{H}_2\text{O})]$. [90] All data were acquired at low temperature (below T_N and T_{FE}) and are normalized to the P or M saturation fields. $\Delta P(B)$ goes to zero at 26 T, and magnetization saturates at 30 T. The magneto-infrared data tracks $[M(B)]^2$, but small signatures of the ΔP transitions are also apparent in the infrared data as deviations from this trend.

exchange. The combination of these techniques provides a rare opportunity to investigate the interplay between spin and charge of a particular lattice distortion – whereas polarization and magnetization measure the long-range response of the entire material, magneto-infrared spectroscopy probes a specific chemical bond.

Spin-phonon coupling is the dominant field-driven interaction in $(\text{NH}_4)_2[\text{FeCl}_5 \cdot (\text{H}_2\text{O})]$, evidenced by the strong similarities between $[M(B)]^2$ and $\int |\Delta\alpha| d\omega$. Strikingly, we also observe modest signatures of ΔP near the low-field polarization rotation along with the high-field change in which ΔP drops to zero – they appear as deviations from $[M(B)]^2$ and are highlighted in light blue in Fig. 7.4. The response of magneto-elastic distortions to the electronic properties is altogether unexplored, as previous work focuses solely on spin-phonon interactions related to changes in the overlap integral within superexchange pathways. However,

when magnetic field perturbs the spin state and the overall electric polarization (which are both sensed by the lattice), electron-phonon coupling emerges. Although electron-phonon coupling is typically demonstrated through optical measurements, we observe electronic signatures because infrared spectroscopy is considered to measure a change in dipole moment and is sensitive to both the charge and volume of a material. We therefore reveal that – in a magnetoelectric multiferroic – signatures of both spin-phonon and electron-phonon coupling are observable, albeit with different magnitudes.

Chapter 8

Summary and outlook

In this dissertation, I present the spectroscopic study of several important molecule-based multiferroics and quantum magnets in order to explore the exotic properties that emerge from flexible lattices, low energy scales, and strong spin-lattice-charge mixing. By probing the vibrations in these systems as a function of temperature, magnetic field, high pressure, and chemical substitution, I reveal the microscopic mechanisms required to reach non-equilibrium phases such as those that develop ferroelectricity, magnetism, and their mutual coupling.

The first problem focuses on the interplay between electric and magnetic polarizations in the molecule-based multiferroic $[(\text{CH}_3)_2\text{NH}_2]\text{Mn}(\text{HCOO})_3$. These ferroicites are linked by a single phonon - an infrared-active formate bending mode. Analysis of this structure across T_C shows that doublet splitting can be described in terms of a power law fit to the order parameter - just like polarization. The ligand bending mode also couples to the development of magnetization across B_C , a finding that we analyze in terms of how reduction of J_{AFM} facilitates the development of the fully saturated state. That a specific phonon mode underpins both ferroicities and magnetoelectric coupling is remarkable because T_C and T_N are quite different. This discovery opens the door to a significant new research area in tunable low energy-scale

multiferroics.

We build upon these ideas by exploring the structure-property relations that arise in this family of molecule-based multiferroics. We combined magnetization, magneto-infrared spectroscopy, and lattice dynamics calculations to unveil the magnetic field - temperature phase diagrams in multiferroic $[(\text{CH}_3)_2\text{NH}_2]M(\text{HCOO})_3$ ($M=\text{Mn}^{2+}$, Co^{2+} , Ni^{2+}). Although the magnetic saturation field of the Mn analog is experimentally realizable at 15.3 T, much higher fields are required to saturate the Ni and Co complexes. Both the magnetization data to 65 T and knowledge of the exchange energies suggest that these values are around 125 T and 88 T, respectively. Analysis of the infrared spectrum of the Mn and Ni compounds across T_C reveals doublet splitting of the formate bending mode. This local lattice distortion is an order parameter of the ferroelectric transition. Interestingly, a power law fit shows that the dimensionality of these analogs develops differently through T_C , with $[(\text{CH}_3)_2\text{NH}_2]\text{Ni}(\text{HCOO})_3$ being much more mean field like than $[(\text{CH}_3)_2\text{NH}_2]\text{Mn}(\text{HCOO})_3$ as evidenced by the value of the critical exponent. By contrast, $[(\text{CH}_3)_2\text{NH}_2]\text{Co}(\text{HCOO})_3$ reveals a surprising framework rigidity across the order/disorder transition due to modest distortions around the Co^{2+} centers. We therefore conclude that the transition to the ferroelectric state is driven solely by counterion freezing and the consequent hydrogen bonding. Under applied field in the Mn (and most likely, the Ni) compounds, the formate bending mode is involved in the transition to the fully saturated magnetic states, whereas the Co complex adopts a different mechanism involving formate stretching distortions. B-site substitution is thus a powerful tool for the development of structure-property relations within chemically analogous materials, providing control of electronic and magnetic properties, as well as energy scales, without altering the overall architecture.

Another complementary area of work was a comprehensive study of copper-

containing coordination polymers and how spin-phonon coupling strengths vary with structural and magnetic dimensionality. Here, we combined vibrational spectroscopy with a number of different external stimuli to explore spin-lattice coupling in $[\text{Cu}(\text{pyz})_2(2\text{-HOpy})_2](\text{PF}_6)_2$ and $[\text{Cu}(\text{pyz})_{1.5}(4\text{-HOpy})_2](\text{ClO}_4)_2$. The Cu centers in both systems are linked by pyrazine ligands, and by following local lattice distortions under temperature, magnetic field, and pressure, we can analyze magnetoelastic coupling. One of the most fascinating trends emerges across the magnetic quantum phase transition. While zero-dimensional (or “dot-like”) systems connected only by intermolecular hydrogen bonds display no spin-lattice coupling across this type of field-driven transition, coupling increases in the one-dimensional case, reaches a maximum in the ladder, and falls again in layered analogs. The availability of a chemically-related family of copper-containing quantum magnets including the ladder system, $[\text{Cu}(\text{pyz})_{1.5}(4\text{-HOpy})_2](\text{ClO}_4)_2$, is key to unveiling this trend. These findings are applicable to other classes of materials with field-induced transitions from the antiferromagnetic \rightarrow fully saturated state including molecule-based multiferroic and single sheet analogs. [56, 61, 212] $[(\text{CH}_3)_2\text{NH}_2]\text{Mn}(\text{HCOO})_3$, for instance, relies upon asymmetric hydrogen bonding that emanates from an order-disorder transition to produce ferroelectricity, [56] whereas $(\text{NH}_4)_2[\text{FeCl}_5 \cdot (\text{H}_2\text{O})]$ utilizes a number of different hydrogen bond pathways to create magnetic exchange as well as frustration. [61] Analysis of spin-lattice coupling across the magnetic quantum phase transitions in these systems may reveal extended structure-property relationships. These materials may also have applications in single sheet form where ferromagnetic ferroelectricity is rarely explored [212] and as molecular spin-crossover systems for actuators. [213]

To gain further understanding of high-field multiferroic behavior and spin-lattice coupling in molecule-based magnets, we explored $(\text{NH}_4)_2[\text{FeCl}_5 \cdot (\text{H}_2\text{O})]$ via a com-

bination of pulsed-field polarization techniques, magneto-infrared spectroscopy, and lattice dynamics calculations. Polarization effects fall to zero at the same time that the quasicollinear \rightarrow collinear sinusoidal magnetic state occurs, as expected for a type-II multiferroic. Strikingly, spin-lattice coupling across the 30 T magnetic quantum phase transition reveals that nearly all features below 600 cm^{-1} are magneto-active. This is in stark contrast to most molecule-based magnets in which only a few distortions aid in the development of the fully saturated magnetic state. Moreover, these distortions modulate hydrogen-bonding pathways rather than typical metal-ligand-metal exchanges. Composed of entirely hydrogen- and halogen-bonded interactions, $(\text{NH}_4)_2[\text{FeCl}_5\cdot(\text{H}_2\text{O})]$ is unique in that it demonstrates intrinsic coupling of the lattice, electronic properties, and magnetism. Strikingly, a comparison of polarization, magnetization, and magneto-infrared techniques reveals that in addition to these spin-phonon effects, we also observe signatures of electron-phonon coupling, evidenced by modest changes in the magneto-infrared distortions at the polarization transitions. This rare effect motivates further exploration of other families of molecule-based multiferroics in which coupling between spin, charge, and lattice degrees of freedom may exist. Additionally, because $(\text{NH}_4)_2[\text{FeCl}_5\cdot(\text{H}_2\text{O})]$ breaks time reversal, rotational, mirror plane, and inversion symmetry, nonreciprocal effects are likely.

Taken together, these comprehensive findings elucidate the mechanisms and cross-coupling of ferroelectricity and magnetism in several important families of molecule-based multiferroics and quantum magnets. With the application of magnetic field, we can identify the specific lattice distortions that change across magnetic quantum phase transitions in order to understand how different materials reach non-equilibrium phases. Molecule-based materials – with bridged metal ions, well-established superexchange behavior, overall low energy scales, and a wide variety of

structural and magnetic dimensionalities – are ideal candidates with which to explore these ideas. This research motivates further exploration of other complex molecular magnets under extreme conditions, the development of their rich phase diagrams, and the discovery of different properties that arise across magnetic, electronic, and structural phase boundaries.

Bibliography

- [1] E. Pardo, C. Train, H. Liu, L. M. Chamoreau, B. Dkhil, K. Boubekeur, F. Lloret, K. Nakatani, H. Tokoro, S. I. Ohkoshi, and M. Verdaguer. *Angew. Chemie - Int. Ed.*, **51**, 8356 (2012).
- [2] R. Shang, G.-C. Xu, Z.-M. Wang, and S. Gao. **3**, 1146 (2014).
- [3] T. V. Brinzari, P. Chen, L. C. Tung, Y. Kim, D. Smirnov, J. Singleton, J. S. Miller, and J. L. Musfeldt. *Phys. Rev. B*, **86**, 214411 (2012).
- [4] Y. Tian, W. Wang, Y. Chai, J. Cong, S. Shen, L. Yan, S. Wang, X. Han, and Y. Sun. *Phys. Rev. Lett.*, **112**, 10 (2014).
- [5] B. Wehinger, C. Fiolka, A. Lanza, R. Scatena, M. Kubus, A. Grockowiak, W. A. Coniglio, D. Graf, M. Skoulatos, J. H. Chen, J. Gukelberger, N. Casati, O. Zaharko, P. Macchi, K. W. Krämer, S. Tozer, C. Mudry, B. Normand, and C. Rüegg. *Phys. Rev. Lett.*, **121**, 117201 (2018).
- [6] A. J. Steele, T. Lancaster, S. J. Blundell, P. J. Baker, F. L. Pratt, C. Baines, M. M. Conner, H. I. Southerland, J. L. Manson, and J. A. Schlueter. *Phys. Rev. B*, **84**, 064412 (2011).
- [7] P. A. Goddard, J. L. Manson, J. Singleton, I. Franke, T. Lancaster, A. J. Steele, S. J. Blundell, C. Baines, F. L. Pratt, R. D. McDonald, O. E. Ayala-Valenzuela, J. F. Corbey, H. I. Southerland, P. Sengupta, and J. A. Schlueter. *Phys. Rev. Lett.*, **108**, 077208 (2012).

- [8] S. N. Herringer, C. P. Landee, M. M. Turnbull, J. Ribas-Ariño, J. J. Novoa, M. Polson, and J. L. Wikaira. *Inorg. Chem.*, **56**, 5441 (2017).
- [9] D. Papoutsakis, J. P. Kirby, J. E. Jackson, and D. G. Nocera. *Chem. - A Eur. J.*, **5**, 1474 (1999).
- [10] P. A. Goodson, J. Glerup, D. J. Hodgson, K. Michelsen, and U. Rychlewska. *Inorg. Chem.*, **33**, 359 (1994).
- [11] A. Orendáčová, M. Kajaková, J. Černák, J. H. Park, E. Čižmár, M. Orendáč, A. Vlček, O. V. Kravchyna, A. G. Anders, A. Feher, and M. W. Meisel. *Chem. Phys.*, **309**, 115 (2005).
- [12] A. O. Polyakov, A. H. Arkenbout, J. Baas, G. R. Blake, A. Meetsma, A. Caretta, P. H. M. Van Loosdrecht, and T. T. M. Palstra. *Chem. Mater.*, **24**, 133 (2012).
- [13] S. H. Lapidus, J. L. Manson, J. Liu, M. J. Smith, P. Goddard, J. Bendix, C. V. Topping, J. Singleton, C. Dunmars, J. F. Mitchell, and J. A. Schlueter. *Chem. Commun.*, **49**, 3558 (2013).
- [14] J. Schnack, H. Nojiri, P. Kögerler, G. J. T. Cooper, and L. Cronin. *Phys. Rev. B*, **70**, 174420 (2004).
- [15] B. Kundys, A. Lappas, M. Viret, V. Kapustianyk, V. Rudyk, S. Semak, C. Simon, and I. Bakaimi. *Phys. Rev. B*, **81**, 224434 (2010).
- [16] J. L. Manson, J. A. Schlueter, K. A. Funk, H. I. Southerland, B. Twamley, T. Lancaster, S. J. Blundell, P. J. Baker, F. L. Pratt, J. Singleton, R. D. McDonald, P. A. Goddard, P. Sengupta, C. D. Batista, L. Ding, C. Lee, M. H. Whangbo, I. Franke, S. Cox, C. Baines, and D. Trial. *J. Am. Chem. Soc.*, **131**, 6733 (2009).

- [17] B. C. Watson, V. N. Kotov, M. W. Meisel, D. W. Hall, G. E. Granroth, W. T. Montfrooij, S. E. Nagler, D. A. Jensen, R. Backov, M. A. Petruska, G. E. Fanucci, and D. R. Talham. *Phys. Rev. Lett.*, **86**, 5168 (2001).
- [18] J. Schnack. *Contemp. Phys.*, 1–18 (2019).
- [19] K. R. O’Neal, Z. Liu, J. S. Miller, R. S. Fishman, and J. L. Musfeldt. *Phys. Rev. B*, **90**, 104301 (2014).
- [20] K. D. Hughey, N. C. Harms, K. R. O’Neal, A. J. Clune, J. C. Monroe, A. L. Blockmon, C. P. Landee, Z. Liu, M. Ozerov, and J. L. Musfeldt, submitted.
- [21] P. Coleman and A. Schofield. *Nature*, **433**, 226 (2005).
- [22] T. Lancaster, P. A. Goddard, S. J. Blundell, F. R. Foronda, S. Ghannadzadeh, J. S. Möller, P. J. Baker, F. L. Pratt, C. Baines, L. Huang, J. Wosnitza, R. D. McDonald, K. A. Modic, J. Singleton, C. V. Topping, T. A. W. Beale, F. Xiao, J. A. Schlueter, A. M. Barton, R. D. Cabrera, K. E. Carreiro, H. E. Tran, and J. L. Manson. *Phys. Rev. Lett.*, **112**, 207201 (2014).
- [23] Y. Kono, T. Sakakibara, C. P. Aoyama, C. Hotta, M. M. Turnbull, C. P. Landee, and Y. Takano. *Phys. Rev. Lett.*, **114**, 037202 (2015).
- [24] S. Sachdev and B. Keimer. *Phys. Today*, **64**, 29 (2011).
- [25] M. T. Batchelor, X. W. Guan, N. Oelkers, K. Sakai, Z. Tsuboi, and A. Foerster. *Phys. Rev. Lett.*, **91**, 217202 (2003).
- [26] E. V. Gorbar, V. P. Gusynin, V. A. Miransky, and I. A. Shovkovy. *Phys. Rev. B*, **66**, 045108 (2002).
- [27] J. L. Manson, C. R. Kmetz, F. Palacio, A. J. Epstein, and J. S. Miller. *Chem. Mater.*, **13**, 1068 (2001).

- [28] J. A. Rodríguez-Velamazán, O. Fabelo, J. Campo, Á. Millán, J. Rodríguez-Carvajal, and L. C. Chapon. *Phys. Rev. B*, **95**, 174439 (2017).
- [29] T. V. Brinzari, P. Chen, Q. C. Sun, J. Liu, L. C. Tung, Y. Wang, J. A. Schlueter, J. Singleton, J. L. Manson, M. H. Whangbo, A. P. Litvinchuk, and J. L. Musfeldt. *Phys. Rev. Lett.*, **110**, 237202 (2013).
- [30] A. Clune, K. Hughey, C. Lee, N. Abhyankar, X. Ding, N. Dalal, M.-H. Whangbo, J. Singleton, and J. Musfeldt. *Phys. Rev. B*, **96**, 104424 (2017).
- [31] S. Ghannadzadeh, J. S. Möller, P. A. Goddard, T. Lancaster, F. Xiao, S. J. Blundell, A. Maisuradze, R. Khasanov, J. L. Manson, S. W. Tozer, D. Graf, and J. A. Schlueter. *Phys. Rev. B*, **87**, 241102(R) (2013).
- [32] K. R. O’Neal, B. S. Holinsworth, Z. Chen, P. K. Peterson, K. E. Carreiro, C. Lee, J. L. Manson, M.-H. Whangbo, Z. Li, Z. Liu, and J. L. Musfeldt. *Inorg. Chem.*, **55**, 12172 (2016).
- [33] A. Prescimone, C. Morien, D. Allan, J. A. Schlueter, S. W. Tozer, J. L. Manson, S. Parsons, E. K. Brechin, and S. Hill. *Angew. Commun.*, **51**, 7490 (2012).
- [34] R. I. Thomson, P. Jain, A. K. Cheetham, and M. A. Carpenter. *Phys. Rev. B*, **86**, 214304 (2012).
- [35] J. Adamson, N. P. Funnell, A. L. Thompson, and A. L. Goodwin. *Phys. Chem. Chem. Phys.*, **16**, 2654 (2014).
- [36] K. R. O’Neal, T. V. Brinzari, J. B. Wright, C. Ma, S. Giri, J. A. Schlueter, Q. Wang, P. Jena, Z. Liu, and J. L. Musfeldt. *Sci. Rep.*, **4**, 6054 (2014).
- [37] W. Wang, L. Q. Yan, J. Z. Cong, Y. L. Zhao, F. Wang, S. P. Shen, T. Zou, D. Zhang, S. G. Wang, X. F. Han, and Y. Sun. *Sci. Rep.*, **3**, 2024 (2013).

- [38] P. Jain, A. Stroppa, D. Nabok, A. Marino, A. Rubano, D. Paparo, M. Matsubara, H. Nakotte, M. Fiebig, S. Picozzi, E. S. Choi, A. K. Cheetham, C. Draxl, N. S. Dalal, and V. S. Zapf. *npj Quantum Mater.*, **1**, 16012 (2016).
- [39] P. J. Baker, T. Lancaster, I. Franke, W. Hayes, S. J. Blundell, F. L. Pratt, P. Jain, Z.-M. Wang, and M. Kurmoo. *Phys. Rev. B*, **82**, 012407 (2010).
- [40] K. Vinod, C. S. Deepak, S. Sharma, D. Sornadurai, A. T. Satya, T. R. Ravindran, C. S. Sundar, and A. Bharathi. *RSC Adv.*, **5**, 37818 (2015).
- [41] L. C. Gómez-Aguirre, B. Pato-Doldón, J. Mira, S. Castro-García, M. A. Senarís-Rodríguez, M. Sanchez-Andújar, J. Singleton, and V. S. Zapf. *J. Am. Chem. Soc.*, **138**, 1122 (2015).
- [42] F.-R. Fan, H. Wu, D. Nabok, S. Hu, W. Ren, C. Draxl, and A. Stroppa. *J. Am. Chem. Soc.*, **139**, 12883 (2017).
- [43] J. Kreisel and M. Kenzelmann. *Europhys. News*, **40**, 17 (2009).
- [44] J. P. Thomas and M. A. Qidwai. *Acta Mater.*, **52**, 2155 (2004).
- [45] M. Behl, M. Y. Razzaq, and A. Lendlein. *Adv. Mater.*, **22**, 3388 (2010).
- [46] S. Nemat-Nasser, S. Nemat-Nasser, T. Plaisted, A. Starr, and A. V. Amirkhizi. *Biomimetics Biol. Inspired Technol.*, **12**, 309 (2005).
- [47] Z. Surowiak and D. Bochenek. *Arch. Acoust.*, **33**, 243 (2008).
- [48] C. Bellitto, E. M. Bauer, and G. Righini. *Coord. Chem. Rev.*, **289-290**, 123 (2015).
- [49] J. Dho, W. Kim, E. Chi, N. Hur, S. Park, and H.-C. Ri. *Solid State Commun.*, **125**, 143 (2003).

- [50] Y. Tian, A. Stroppa, Y. Chai, L. Yan, S. Wang, P. Barone, S. Picozzi, and Y. Sun. *Sci. Rep.*, **4**, 6062 (2014).
- [51] J. Alberto Rodríguez-Velamazán, Ó. Fabelo, Á. Millán, J. Campo, R. D. Johnson, and L. Chapon. *Sci. Rep.*, **5**, 14475 (2015).
- [52] S. Gnewuch and E. E. Rodriguez. *J. Solid State Chem.*, **271**, 175 (2019).
- [53] D. Khomskii. *Physics*, **2**, 20 (2009).
- [54] W. Eerenstein, N. D. Mathur, and J. F. Scott. *Nature*, **442**, 759 (2006).
- [55] N. A. Spaldin and M. Fiebig. *Science*, **309**, 391 (2005).
- [56] P. Jain, V. Ramachandran, R. J. Clark, H. D. Zhou, B. H. Toby, N. S. Dalal, H. W. Kroto, and A. K. Cheetham. *J. Am. Chem. Soc.*, **131**, 13625 (2009).
- [57] R. Ramesh and N. A. Spaldin. *Nat. Mater.*, **6**, 21 (2007).
- [58] T. Kimura, G. Lawes, T. Goto, Y. Tokura, and A. P. Ramirez. *Phys. Rev. B*, **71**, 224425 (2005).
- [59] A. Singh, V. Pandey, R. K. Kotnala, and D. Pandey. *Phys. Rev. Lett.*, **101**, 247602 (2008).
- [60] S. Dong, J.-M. Liu, S.-W. Cheong, and Z. Ren. *Adv. Phys.*, **64**, 1 (2015).
- [61] M. Ackermann, D. Brüning, T. Lorenz, P. Becker, and L. Bohatý. *New J. Phys.*, **15**, 123001 (2013).
- [62] I. B. Bersuker. *J. Phys. Conf. Ser.*, **428**, 012028 (2013).
- [63] N. A. Hill. *J. Phys. Chem. B*, **104**, 6694 (2000).

- [64] S. Blundell, *Magnetism in Condensed Matter*, Oxford University Press Inc., New York (2001).
- [65] B. Lorenz. ISRN Condens. Matter Phys., **2013**, 497073 (2013).
- [66] N. A. Hill. AIP Conf. Proc., **535**, 372 (2000).
- [67] F. Zavaliche, S. Y. Yang, T. Zhao, Y. H. Chu, M. P. Cruz, C. B. Eom, and R. Ramesh. Phase Transitions, **79**, 991 (2006).
- [68] A. Midya, S. N. Das, P. Mandal, S. Pandya, and V. Ganesan. Phys. Rev. B, **84**, 235127 (2011).
- [69] Y. Tokura. J. Magn. Magn. Mater., **310**, 1145 (2007).
- [70] Y. Tian, A. Stroppa, Y. S. Chai, P. Barone, M. Perez-Mato, S. Picozzi, and Y. Sun. Phys. Status Solidi - Rapid Res. Lett., **9**, 62 (2015).
- [71] W. Li, Z. Wang, F. Deschler, S. Gao, R. H. Friend, and A. K. Cheetham. Nat. Rev. Mater., **2**, 16099 (2017).
- [72] A. Stroppa, P. Jain, P. Barone, M. Marsman, J. M. Perez-Mato, A. K. Cheetham, H. W. Kroto, and S. Picozzi. Angew. Chemie - Int. Ed., **50**, 5847 (2011).
- [73] J. S. Miller. Mater. Today, **17**, 224 (2017).
- [74] H. B. Cui, Z. Wang, K. Takahashi, Y. Okano, H. Kobayashi, and A. Kobayashi. J. Am. Chem. Soc., **128**, 15074 (2006).
- [75] H. B. Cui, B. Zhou, L. S. Long, Y. Okano, H. Kobayashi, and A. Kobayashi. Angew. Chemie - Int. Ed., **47**, 3376 (2008).

- [76] M. Šiménas, A. Ciupa, M. Ma, A. Póppl, and J. Banys. *J. Phys. Chem. C*, **119**, 24522 (2015).
- [77] H. L. Cai, Y. Zhang, D. W. Fu, W. Zhang, T. Liu, H. Yoshikawa, K. Awaga, and R. G. Xiong. *J. Am. Chem. Soc.*, **134**, 18487 (2012).
- [78] M. Wu, J. D. Burton, E. Y. Tsympal, X. C. Zeng, and P. Jena. *J. Am. Chem. Soc.*, **134**, 14423 (2012).
- [79] C. Bosch-Serrano, J. M. Clemente-Juan, E. Coronado, A. Gaita-Ariño, A. Pali, and B. Tsukerblat. *Phys. Rev. B*, **86**, 024432 (2012).
- [80] J. H. Lee, L. Fang, E. Vlahos, X. Ke, Y. W. Jung, L. F. Kourkoutis, J. W. Kim, P. J. Ryan, T. Heeg, M. Roeckerath, V. Goian, M. Bernhagen, R. Uecker, P. C. Hammel, K. M. Rabe, S. Kamba, J. Schubert, J. W. Freeland, D. A. Muller, C. J. Fennie, P. Schiffer, V. Gopalan, E. Johnston-Halperin, and D. G. Schlom. *Nature*, **466**, 954 (2010).
- [81] A. B. Sushkov, O. Tchernyshyov, W. Ratcliff, S. W. Cheong, and H. D. Drew. *Phys. Rev. Lett.*, **94**, 137202 (2005).
- [82] L. D. Casto, A. J. Clune, M. O. Yokosuk, J. L. Musfeldt, T. J. Williams, H. L. Zhuang, M. W. Lin, K. Xiao, R. G. Hennig, B. C. Sales, J. Q. Yan, and D. Mandrus. *APL Mater.*, **3**, 041515 (2015).
- [83] K. D. Hughey, A. J. Clune, M. O. Yokosuk, A. Al-Wahish, K. R. O’Neal, S. Fan, N. Abhyankar, H. Xiang, Z. Li, J. Singleton, N. S. Dalal, and J. L. Musfeldt. *Phys. Rev. B*, **96**, 180305(R) (2017).
- [84] A. Al-Wahish, K. R. O’Neal, C. Lee, S. Fan, K. Hughey, M. O. Yokosuk, A. J. Clune, Z. Li, J. A. Schlueter, J. L. Manson, M.-H. Whangbo, and J. L. Musfeldt. *Phys. Rev. B*, **95**, 104437 (2017).

- [85] J. B. Goodenough, *Magnetism and the Chemical Bond*, Wiley, New York, (1963).
- [86] J. B. Goodenough. Phys. Rev., **100**, 564 (1955).
- [87] J. Kanamori. J. Phys. Chem. Solids, **10**, 87 (1959).
- [88] P. W. Anderson. Phys. Rev., **115**, 2 (1959).
- [89] D. I. Khomskii, *Basic aspects of the quantum theory of solids: order and elementary excitations*, Cambridge University Press, (2010).
- [90] A. J. Clune, J. Nam, M. Lee, K. D. Hughey, W. Tian, J. Fernandez-Baca, R. S. Fishman, J. Singleton, J. H. Lee, and J. L. Musfeldt, npj Quantum Mater., **4**, 44 (2019).
- [91] I. Nemeč, R. Herchel, T. Šilha, and Z. Trávníček. Dalt. Trans., **43**, 15602 (2014).
- [92] S. Seth. Crystals, **8**, 455 (2018).
- [93] J. Cao, J. T. Haraldsen, S. Brown, J. L. Musfeldt, J. R. Thompson, S. Zvyagin, J. Krzystek, M. H. Whangbo, S. E. Nagler, and C. C. Torardi. Phys. Rev. B, **72**, 214421 (2005).
- [94] A. Barbour, R. D. Luttrell, J. Choi, J. L. Musfeldt, D. Zipse, N. S. Dalal, D. W. Boukhvalov, V. V. Dobrovitski, M. I. Katsnelson, A. I. Lichtenstein, B. N. Harmon, and P. Kögerler. Phys. Rev. B, **74**, 014411 (2006).
- [95] J. A. Schlueter, H. Park, G. J. Halder, W. R. Armand, C. Dunmars, K. W. Chapman, J. L. Manson, J. Singleton, R. McDonald, A. Plonczak, J. Kang, C. Lee, M.-H. Whangbo, T. Lancaster, A. J. Steele, I. Franke, J. D. Wright,

- S. J. Blundell, F. L. Pratt, J. DeGeorge, M. M. Turnbull, and C. P. Landee. *Inorg. Chem.*, **51**, 2121 (2012).
- [96] M. Fourmigué and P. Batail. *Chem. Rev.*, **104**, 5379 (2004).
- [97] M. Owczarek, K. A. Hujsak, D. P. Ferris, A. Prokofjevs, I. Majerz, P. A. Szklarz, H. Zhang, A. A. Sarjeant, C. L. Stern, R. Jakubas, S. Hong, V. P. Dravid, and J. F. Stoddart. *Nat. Commun.*, **7** (2016).
- [98] M. A. Abdalrahman, F. F. Awwadi, G. B. Jameson, C. P. Landee, C. G. Saunders, M. M. Turnbull, and J. L. Wikaira. *CrystEngComm*, **15**, 4309 (2013).
- [99] S. Sachdev. **288**, 475 (2000).
- [100] V. Franco, J. S. Blázquez, and A. Conde. *Appl. Phys. Lett.*, **89**, 222512 (2006).
- [101] M. Maczka, A. Gagor, M. Ptak, W. Paraguassu, T. A. Da Silva, A. Sieradzki, and A. Pikul. *Chem. Mater.*, **29**, 2264 (2017).
- [102] A. Köhler, S. T. Hoffmann, and H. Bässler. *J. Am. Chem. Soc.*, **134**, 11594 (2012).
- [103] T. Furukawa, K. Miyagawa, H. Taniguchi, R. Kato, and K. Kanoda. *Nat. Phys.*, **11**, 221 (2015).
- [104] J. Biscaras, N. Bergeal, S. Hurand, C. Feuillet-Palma, A. Rastogi, R. C. Budhani, M. Grilli, S. Caprara, and J. Lesueur. *Nat. Mater.*, **12**, 542 (2013).
- [105] J. Wang, *Doctoral Dissertation*, California Institute of Technology, 2009.
- [106] G. Chaboussant, M. H. Julien, Y. Fagot-Revurat, M. Hanson, L. P. Lévy, C. Berthier, M. Horvatić, and O. Piovesana. *Eur. Phys. J. B*, **6**, 167 (1998).

- [107] Z. Honda, H. A. Katori, M. Ikeda, M. Hagiwara, K. Okunishi, M. Sakai, T. Fukuda, and N. Kamata. *J. Phys. Soc. Japan*, **81**, 113710 (2012).
- [108] Y. Dagan, M. M. Qazilbash, C. P. Hill, V. N. Kulkarni, and R. L. Greene. *Phys. Rev. Lett.*, **92**, 167001 (2004).
- [109] S. Sachdev. *Philos. Trans. A*, **374** (2015).
- [110] J. L. White, C. Lee, O. Günaydin-Şen, L. C. Tung, H. M. Christen, Y. J. Wang, M. M. Turnbull, C. P. Landee, R. D. McDonald, S. A. Crooker, J. Singleton, M. H. Whangbo, and J. L. Musfeldt. *Phys. Rev. B*, **81**, 052407 (2010).
- [111] A. Sozinov, A. A. Likhachev, N. Lanska, and K. Ullakko. *Appl. Phys. Lett.*, **80**, 1746 (2002).
- [112] E. Granado, A. García, J. A. Sanjurjo, C. Rettori, I. Torriani, F. Prado, R. D. Sánchez, A. Caneiro, and S. B. Oseroff. *Phys. Rev. B*, **60**, 11879 (1999).
- [113] T. V. Brinzari, J. T. Haraldsen, P. Chen, Q. C. Sun, Y. Kim, L. C. Tung, A. P. Litvinchuk, J. A. Schlueter, D. Smirnov, J. L. Manson, J. Singleton, and J. L. Musfeldt. *Phys. Rev. Lett.*, **111**, 047202 (2013).
- [114] J. L. Musfeldt, L. I. Vergara, T. V. Brinzari, C. Lee, L. C. Tung, J. Kang, Y. J. Wang, J. A. Schlueter, J. L. Manson, and M. H. Whangbo. *Phys. Rev. Lett.*, **103**, 147401 (2009).
- [115] A. K. Cheetham and C. N. R. Rao. **318**, 141 (2008).
- [116] J. L. Rowsell and O. M. Yaghi. *Microporous Mesoporous Mater.*, **73**, 3 (2004).
- [117] C. N. R. Rao, A. Müller, and A. K. Cheetham, *The Chemistry of Nanomaterials: Synthesis, Properties and Applications*, Wiley-VCH Verlag & Co. (2004).

- [118] C. N. R. Rao, A. K. Cheetham, and A. Thirumurugan. *J. Phys. Condens. Matter*, **20**, 083202 (2008).
- [119] J.-C. Tan and B. Civalleri. *CrystEngComm*, **17**, 197 (2015).
- [120] K. D. Hughey, A. J. Clune, M. O. Yokosuk, J. Li, N. Abhyankar, X. Ding, N. D. Dalal, H. Xiang, D. Smirnov, J. Singleton, and J. L. Musfeldt. *Inorg. Chem.*, **57**, 11569 (2018).
- [121] D. B. Litvin. *Acta Crystallogr.*, **A42**, 44 (1986).
- [122] M. Mączka, M. Ptak, and L. Macalik. *Vib. Spectrosc.*, **71**, 98 (2014).
- [123] H. D. Duncan, M. T. Dove, D. A. Keen, and A. E. Phillips. *Dalt. Trans.*, **45**, 4380 (2016).
- [124] N. Abhyankar, S. Bertaina, and N. S. Dalal. *J. Phys. Chem. C*, **119**, 28143 (2015).
- [125] R. Yadav, D. Swain, H. L. Bhat, and S. Elizabeth. *J. Appl. Phys.*, **119**, 064103 (2016).
- [126] X. Y. Wang, L. Gan, S. W. Zhang, and S. Gao. *Inorg. Chem.*, **43**, 4615 (2004).
- [127] Y. P. Wang, X. G. Li, X. G. Zhang, G. Christou, and H. P. Cheng. *J. Phys. Chem. C*, **121**, 10893 (2017).
- [128] J. López-Beceiro, C. Gracia-Fernández, S. Gómez-Barreiro, S. Castro-García, M. Sánchez-Andújar, and R. Artiaga. *J. Phys. Chem. C*, **116**, 1219 (2011).
- [129] M. Mączka, A. Pietraszko, L. Macalik, A. Sieradzki, J. Trzmiel, and A. Pikul. *Dalt. Trans.*, **43**, 17075 (2014).

- [130] A. Vasiliev, O. Volkova, E. Zvereva, and M. Markina. *npj Quantum Mater.*, **3**, 18 (2018).
- [131] V. S. Zapf, V. F. Correa, P. Sengupta, C. D. Batista, M. Tsukamoto, N. Kawashima, P. Egan, C. Pantea, A. Migliori, J. B. Betts, M. Jaime, and A. Paduan-Filho. *Phys. Rev. B*, **77**, 020404(R) (2008).
- [132] W. Qin, B. Xu, and S. Ren. *Nanoscale*, **7**, 9122 (2015).
- [133] J. L. Manson, Q. Z. Huang, C. M. Brown, J. W. Lynn, M. B. Stone, J. Singleton, and F. Xiao. *Inorg. Chem.*, **54**, 11897 (2015).
- [134] T. Hong, K. P. Schmidt, K. Coester, F. F. Awwadi, M. M. Turnbull, M. Zhu, X. Ke, C. P. Aoyama, Y. Takano, H. Cao, W. Tian, J. Ma, R. Custelcean, H. D. Zhou, and M. Matsuda. *Phys. Rev. B*, **89**, 174432 (2014).
- [135] D. Blosser, N. Kestin, K. Y. Povarov, R. Bewley, E. Coira, T. Giamarchi, and A. Zheludev. *Phys. Rev. B*, **96**, 134406 (2017).
- [136] J. Liu, S. Kittaka, R. D. Johnson, T. Lancaster, J. Singleton, T. Sakakibara, Y. Kohama, J. Van Tol, A. Ardavan, B. H. Williams, S. J. Blundell, Z. E. Manson, J. L. Manson, and P. A. Goddard. *Phys. Rev. Lett.*, **122**, 057207 (2019).
- [137] S. Horiuchi, Y. Okimoto, R. Kumai, and Y. Tokura. *Science*, **299**, 229 (2003).
- [138] A. Gaita-Ariño, F. Luis, S. Hill, and E. Coronado. *Nat. Chem.*, **11**, 301 (2019).
- [139] D. Blosser, V. K. Bhartiya, D. J. Voneshen, and A. Zheludev. *Phys. Rev. Lett.*, **121**, 247201 (2018).

- [140] E. Čižmár, M. Ozerov, J. Wosnitza, B. Thielemann, K. W. Krämer, C. Rüegg, O. Piovesana, M. Klanjšek, M. Horvatić, C. Berthier, and S. A. Zvyagin. *Phys. Rev. B*, **82**, 054431 (2010).
- [141] M. B. Stone, D. H. Reich, C. Broholm, K. Lefmann, C. Rischel, C. P. Landee, and M. M. Turnbull. *Phys. Rev. Lett.*, **91**, 037205 (2003).
- [142] A. A. Validov, E. M. Lavrentyeva, M. Ozerov, S. A. Zvyagin, M. M. Turnbull, C. P. Landee, and G. B. Teitel'baum. *J. Phys. Conf. Ser.*, **200**, 022070 (2010).
- [143] C. P. Landee and M. M. Turnbull. *Eur. J. Inorg. Chem.*, 2266 (2013).
- [144] Y. Narumi, N. Terada, Y. Tanaka, M. Iwaki, K. Katsumata, K. Kindo, H. Kageyama, Y. Ueda, H. Toyokawa, T. Ishikawa, and H. Kitamura. *J. Phys. Soc. Japan*, **78**, 043702 (2009).
- [145] L. Zhao, M. T. Fernández-Díaz, L. H. Tjeng, and A. C. Komarek. *Sci. Adv.*, **2**, 1 (2016).
- [146] B. M. Huddart, J. Brambleby, T. Lancaster, P. A. Goddard, F. Xiao, S. J. Blundell, F. L. Pratt, J. Singleton, P. Macchi, R. Scatena, A. M. Barton, and J. L. Manson. *Phys. Chem. Chem. Phys.*, **21**, 1014 (2019).
- [147] J. H. Yu, J. Q. Xu, L. Ye, H. Ding, W. J. Jing, T. G. Wang, J. N. Xu, H. B. Jia, Z. C. Mu, and G. D. Yang. *Inorg. Chem. Commun.*, **5**, 572 (2002).
- [148] C. P. Landee, N. Nizar, K. Richardson, J. C. Monroe, M. M. Turnbull, M. Polson, S. Vela, W. Blackmore, P. A. Goddard, F. Xiao, T. Lancaster, R. C. Williams, P. M. D. Gape, F. L. Pratt, and S. J. Blundell, in preparation.
- [149] E. Čižmár, S. A. Zvyagin, R. Beyer, M. Uhlarz, M. Ozerov, Y. Skourski, J. L. Manson, J. A. Schlueter, and J. Wosnitza. *Phys. Rev. B*, **81**, 064422 (2010).

- [150] P. A. Goddard, J. Singleton, P. Sengupta, R. D. McDonald, T. Lancaster, S. J. Blundell, F. L. Pratt, S. Cox, N. Harrison, J. L. Manson, H. I. Southerland, and J. A. Schlueter. *New J. Phys.*, **10**, 083025 (2008).
- [151] J. A. Rodríguez-Velamazán, Ó. Fabelo, Á. Millán, R. D. Johnson, and L. Chapon. *Sci. Rep.*, **5**, 14475 (2015).
- [152] J. N. McElearney and S. Merchant. *Inorg. Chem.*, **17**, 1207 (1978).
- [153] W. Tian, H. B. Cao, A. J. Clune, K. D. Hughey, T. Hong, J.-Q. Yan, H. K. Agrawal, J. Singleton, B. C. Sales, R. S. Fishman, J. L. Musfeldt, and J. A. Fernandez-Baca. *Phys. Rev. B*, **98**, 054407 (2018).
- [154] R. Samantaray, R. J. Clark, E. S. Choi, H. Zhou, and N. S. Dalal. *J. Am. Chem. Soc.*, **133**, 3792 (2011).
- [155] W. Tian, H. Cao, J. Wang, F. Ye, M. Matsuda, J.-Q. Yan, Y. Liu, V. O. Garlea, H. K. Agrawal, B. C. Chakoumakos, B. C. Sales, R. S. Fishman, and J. A. Fernandez-Baca. *Phys. Rev. B*, **94**, 214405 (2016).
- [156] J. Cao, L. I. Vergara, J. L. Musfeldt, A. P. Litvinchuk, Y. J. Wang, S. Park, and S. W. Cheong. *Phys. Rev. Lett.*, **100**, 177205 (2008).
- [157] O. Günaydin-Şen, C. Lee, L. C. Tung, P. Chen, M. M. Turnbull, C. P. Landee, Y. J. Wang, M.-H. Whangbo, and J. L. Musfeldt. *Phys. Rev. B*, **81**, 104307 (2010).
- [158] A. B. Sushkov, J. L. Musfeldt, Y. J. Wang, R. M. Achey, and N. S. Dalal. *Phys. Rev. B*, **66**, 144430 (2002).
- [159] F. Wooten. *Optical Properties Of Solids*. Academic Press (1972).
- [160] D. A. McQuarrie, *Quantum Chemistry*, University Science Books, (2008).

- [161] R. L. Carlin and A. J. van Duyneveldt, *Magnetic properties of transition metal compounds*, Springer-Verlag, (1977).
- [162] S. Kamba, V. Goian, V. Skoromets, J. Hejtmánek, V. Bovtun, M. Kempa, F. Borodavka, P. Vaněk, A. A. Belik, J. H. Lee, O. Pacherová, and K. M. Rabe. Phys. Rev. B, **89**, 064308 (2014).
- [163] C. Kittel, *Introduction to solid state physics*, Wiley (2005).
- [164] P. J. Larkin, *Infrared and Raman Spectroscopy*, Elsevier Science (2011).
- [165] P. F. Bernath, *Spectra of Atoms and Molecules*, Oxford University Press (1995).
- [166] M. A. Sherwood, *Vibrational Spectroscopy of Solids*, Cambridge University Press, (1972).
- [167] J. M. Chalmer and P. R. Griffiths, *Handbook of Vibrational Spectroscopy*, John Wiley and Sons Ltd, Chichester (2002).
- [168] W. Koch and M. C. Holthausen, *A Chemist's Guide to Density Functional Theory*, Wiley-VCH (2001).
- [169] R. A. Shaw and H. H. Mantsch, *Near-IR Spectrometers*, Encyclopedia of Spectroscopy and Spectrometry, Academic Press (1999).
- [170] N. Waeselmann, *Doctoral Dissertation*, Hamburg, 2012.
- [171] H. K. Mao, J. Xu, and P. M. Bell. J. Geophys. Res., **91**, 4673 (1986).
- [172] A. I. Liechtenstein, V. I. Anisimov, and J. Zaanen, Phys. Rev. B **52**, R5467 (1995).
- [173] J. P. Perdew, K. Burke, and M. Ernzerhof, Phys. Rev. Lett. **77**, 3865 (1996).

- [174] G. Kresse and J. Furthmüller, *Comput. Mater. Sci.* **6**, 15 (1996).
- [175] G. Kresse and J. Furthmüller, *Phys. Rev. B* **54**, 11169 (1996).
- [176] P. E. Blöchl, *Phys. Rev. B* **50**, 17953 (1994).
- [177] G. Kresse and D. Joubert, *Phys. Rev. B* **59**, 1758 (1999).
- [178] M. Sánchez-Andújar, S. Presedo, S. Yáñez Vilar, S. Castro-García, J. Shamir, and M. A. Señarís-Rodríguez. *Inorg. Chem.*, **49**, 1510 (2010).
- [179] K. Szymborska-Malek, M. Trzebiatowska-Gusowska, M. Maczka, and A. Gagor. *Spectrochim. Acta - Part A Mol. Biomol. Spectrosc.*, **159**, 35 (2016).
- [180] F. Kagawa, K. Miyagawa, and K. Kanoda. *Nature*, **436**, 534 (2005).
- [181] J. H. Lee and K. M. Rabe. *Phys. Rev. B*, **84**, 104440 (2011).
- [182] V. Goian, F. Kadlec, C. Kadlec, B. Dabrowski, S. Kolesnik, O. Chmaissem, D. Nuzhnyy, M. Kempa, V. Bovtun, M. Savinov, J. Hejtmánek, J. Prokleška, and S. Kamba. *J. Phys. Condens. Matter*, **28**, 175901 (2016).
- [183] A. B. Sushkov, C. Kant, M. Schiebl, A. M. Shuvaev, A. Pimenov, A. Pimenov, B. Lorenz, S. Park, S. W. Cheong, M. Mostovoy, and H. D. Drew. *Phys. Rev. B*, **90**, 054417 (2014).
- [184] M. Schmidt, C. Kant, T. Rudolf, F. Mayr, A. A. Mukhin, A. M. Balbashov, J. Deisenhofer, and A. Loidl. *Eur. Phys. J. B*, **71**, 411 (2009).
- [185] M. Sánchez-Andújar, L. C. Gómez-Aguirre, B. Pato Doldán, S. Yáñez-Vilar, R. Artiaga, A. L. Llamas-Saiz, R. S. Manna, F. Schnelle, M. Lang, F. Ritter, A. A. Haghighirad, and M. A. Señarís-Rodríguez. *CrystEngComm*, **16**, 3558 (2014).

- [186] M. Mączka, W. Zierkiewicz, D. Michalska, and J. Hanuza. *Spectrochim. Acta Part A Mol. Biomol. Spectrosc.*, **128**, 674 (2014).
- [187] M. Mączka, T. A. da Silva, W. Paraguassu, M. Ptak, and K. Hermanowicz. *Inorg. Chem.*, **53**, 12650 (2014).
- [188] A. Ciupa, M. Mączka, A. Gągor, A. Sieradzki, J. Trzmiel, A. Pikul, and M. Ptak. *Dalt. Trans.*, **44**, 8846 (2015).
- [189] L. Xin, Z. Fan, G. Li, M. Zhang, Y. Han, J. Wang, K. P. Ong, L. Qin, Y. Zheng, and X. Lou. *New Journal Chem.*, **41**, 151 (2017).
- [190] B. R. Jones, P. A. Varughese, I. Olejniczak, J. M. Pigos, J. L. Musfeldt, C. P. Landee, M. M. Turnbull, and G. L. Carr. *Chem. Mater.*, **13**, 2127 (2001).
- [191] A. Al-Wahish, K. O’Neal, C. Lee, S. Fan, K. Hughey, M. Yokosuk, A. Clune, Z. Li, J. Schlueter, J. Manson, M.-H. Whangbo, and J. Musfeldt. *Phys. Rev. B*, **95**, 1 (2017).
- [192] J. Choi, J. D. Woodward, J. L. Musfeldt, C. P. Landee, and M. M. Turnbull. *Chem. Mater.*, **15**, 2797 (2003).
- [193] J. L. Manson, S. H. Lapidus, P. W. Stephens, P. K. Peterson, K. E. Carreiro, H. I. Southerland, T. Lancaster, S. J. Blundell, A. J. Steele, P. A. Goddard, F. L. Pratt, J. Singleton, Y. Kohama, R. D. McDonald, R. E. D. Sesto, N. A. Smith, J. Bendix, S. A. Zvyagin, J. Kang, C. Lee, M.-H. Whangbo, V. S. Zapf, and A. Plonczak. *Inorg. Chem.*, **50**, 5990 (2011).
- [194] O. Vaccarelli, G. Rouse, A. Saúl, and G. Radtke. *Phys. Rev. B*, **96**, 180406(R) (2017).
- [195] B. Bleaney and K. D. Bowers. *Proc. R. Soc. London A*, **214**, 451 (1952).

- [196] L. J. De Jongh. *J. Appl. Phys.*, **49**, 1305 (1978).
- [197] C. J. Fennie and K. M. Rabe. *Phys. Rev. Lett.*, **97**, 267602 (2006).
- [198] T. Rudolf, C. Kant, F. Mayr, J. Hemberger, V. Tsurkan, and A. Loidl. *New J. Phys.*, **9**, 76 (2007).
- [199] K. K. Zhuravlev, K. Traikov, Z. Dong, S. Xie, and Y. Song. *Phys. Rev. B*, **82**, 064116 (2010).
- [200] C. dela Cruz, F. Yen, B. Lorenz, Y. Q. Wang, Y. Y. Sun, M. M. Gospodinov, and C. W. Chu. *Phys. Rev. B*, **71**, 060407(R) (2005).
- [201] S. Saha, D. V. Muthu, C. Pascanut, N. Dragoe, R. Suryanarayanan, G. Dhahlenne, A. Revcolevschi, S. Karmakar, S. M. Sharma, and A. K. Sood. *Phys. Rev. B*, **74**, 064109 (2006).
- [202] G. Radtke, A. Saúl, H. A. Dabkowska, M. B. Salamon, and M. Jaime. *Proc. Natl. Acad. Sci.*, **112**, 1971 (2015).
- [203] J. L. Musfeldt, Z. Liu, S. Li, J. Kang, C. Lee, P. Jena, J. L. Manson, J. A. Schlueter, G. L. Carr, and M.-H. Whangbo. *Inorg. Chem.*, **50**, 6347 (2011).
- [204] K. R. O’Neal, B. S. Holinsworth, Z. Chen, P. K. Peterson, K. E. Carreiro, C. Lee, J. L. Manson, M.-H. Whangbo, Z. Li, Z. Liu, and J. L. Musfeldt. *Inorg. Chem.*, **55**, 12172 (2016).
- [205] S. Brown, J. Cao, J. L. Musfeldt, M. M. Conner, A. C. McConnell, H. I. Southerland, J. L. Manson, J. A. Schlueter, M. D. Phillips, M. M. Turnbull, and C. P. Landee. *Inorg. Chem.*, **46**, 8577 (2007).
- [206] M. Adams and P. J. Lock. *J. Chem. Soc. A Inorganic, Phys. Theor.*, 2801–2806 (1971).

- [207] M. Falk and C.-H. Huang. *Can. J. Chem.*, **55**, 1736 (1974).
- [208] S. K. Sharma and D. K. Pandya. *J. inorg. nucl. chem.*, **36**, 1165 (1974).
- [209] J. Alberto Rodríguez-Velamazán, O. Fabelo, A. Millán, J. Campo, R. D. Johnson, and L. Chapon. *Sci. Rep.*, **5**, 14475 (2015).
- [210] S. Jandl, S. Mansouri, J. Vermette, A. A. Mukhin, V. Y. Ivanov, A. Balbashov, and M. Orlita. *J. Phys. Condens. Matter*, **25** (2013).
- [211] K. R. O’Neal, A. Paul, A. al-Wahish, K. D. Hughey, A. L. Blockmon, X. Luo, S.-W. Cheong, V. S. Zapf, C. V. Topping, J. Singleton, M. Ozerov, T. Birol, and J. L. Musfeldt. *npj Quantum Mater.* **4**, 48 (2019).
- [212] C. Huang, Y. Du, H. Wu, H. Xiang, K. Deng, and E. Kan. *Phys. Rev. Lett.*, **120**, 147601 (2018).
- [213] H. J. Shepherd, I. A. Gural’skiy, C. M. Quintero, S. Tricard, L. Salmon, G. Molnár, and A. Bousseksou. *Nat. Commun.*, **4**, 1 (2013).

Vita

Kendall D. Hughey was born in Jackson, Mississippi. She attended the University of South Carolina between 2010 and 2014, where she received a B.S. degree in Chemistry. Kendall joined the research group of Dr. Janice L. Musfeldt in the Spring of 2015 pursuing her Ph.D. degree from the University of Tennessee. Her research focuses on spin-charge-lattice interactions in molecule-based multiferroics and analyses of symmetry breaking in complex materials. Kendall D. Hughey received a Doctor of Philosophy Degree in Chemistry from the University of Tennessee in December of 2019.